UNIVERSITÀ
DEGLI STUDI DI TRIESTE

Procedure setting to determine the Dynamic transfer stiffness of a resilient mounting element in a low frequency range

PhD candidate: Alexandre HECQUET (UniTS)

Thesis supervisor: Marco BIOT (UniTS)

Co-supervisor: Hervé LE SOURNE (Icam Nantes)

DOCTORATE COORDINATOR: Diego Micheli (UniTS)

Summary

List of figures

Introduction

Passengers comfort on board ship, especially cruise ships and mega-yachts, is one of the most emphasized and discussed point in the marine engineering sector [1] [2]. This comfort depends on several environmental factors that could be outside of the ship. That external cause arises from the weather that induces assorted consequences, such as, certain sea states and ship motions or atmospheric phenomena. Although the impact of these phenomena is significant, it is difficult to anticipate the effect on the ship behavior and thus the engendered trouble on the passenger comfort. However, the effect of internal source of discomfort is, on the contrary, actually predictable. The last studies focused on those issues. It was standardized through the last few years by the ship standardization associations [3] [4].

Among the several possible sources of discomfort a particular attention was paid on the perceived vibrations and air born noises [2] [3] [4] and was pointed about one of the main possible comfort disturbance on passengers [5]. Indeed, the natural frequencies and resonance modes of the body human are from 2 to 60 Hz with different trigger levels depending on the excitation frequency and, consequently, cause more or less disturbance to passengers [6] [7] [8].

According to this specific impact on the human body and therefore passengers, the noises and vibrations levels need to be evaluated. The methodologies and procedures are commonly experimental with specific instrumentation in laboratory or with on board measurements when the ship is in navigation in the pre-test phase [9] [10]. Among the on board instruments and machinery such as pumps, ventilations, propellers, the main sources of back ground noises and vibrations are the engines, which are generally 2 or four strokes engines for civil ships [11] [12] [13].

In fact, the engine room is located at the bottom rear of the ship. Thus, the created vibrations and noises propagates along the ship structure and super-structure to the accommodation areas where the comfort of passengers should be at the maximum, especially in the cabins. Although it is impossible to remove completely the disturbances, it is necessary to reduce them significantly along the noises and vibrations path, between the source and passengers. Even though the discomfort is mainly bi-factorial, the only studied factor in this thesis will be the vibration aspect mainly due to the focused frequency range (1-60 Hz) where the human ear could not perceive the emitted noise.

Considering the architecture of ships especially mega-yacht or cruise ship, the vibrations propagate according to a certain course. It spreads from the engines feet, through the ship hull and thereafter the pillars that sustain the different decks to arrive to the accommodation deck wall and floors. Several studies focused on a possible way to damp the vibrations especially by introducing viscoelastic materials in the pillars [14] or in the floors [15]. However the most common and simple way to avoid the propagations is to suspend the engines using passive isolators [16] where their main purpose is to reduce the vibration level using a constitutive damping material in the isolator structure. In this case, the isolators are labeled Resilient Mounting Element (RME).

To be able to understand all the vibration transmission mechanisms between the engines and the ship structure with resilient elements implementation and thereby make a complete analysis, the six degree of freedom (3 translation and 3 rotations) of the system should be considered along with the mobility of the foundations [17] [18]. However, considering the installation the most judicious approach is the one in which the structural noise source and receiver are considered as a multi-point-connected system with one principal direction of excitation: the vertical one [19] [20] [21] [22] [23].

According to the outlined simplified approach, the dynamic coupling between diesel engine and foundation may be characterize once the resilient mounting system mechanical impedance is identified [24] [25] [26]. This mechanical impedance is related by a simple equation to the dynamic transfer stiffness (DTS) of the single resilient mounting element (RME). This DTS depends on several parameters such as the excitation frequency spectrum, the excitation amplitude and the background temperature and several other trivial parameters. Thus, the DTS determination could allow a behaviour prediction of all the structure depending on those external parameters. So, the main purpose of studies for the dynamic characterization of a resilient mounting element is to determine, by direct test [27] [28] carried out according to the ISO 10846 standard, its dynamic transfer stiffness [29]. However, considering the ISO standards recommended experimental means, it requires substantial material and financial resources as well as a long test period for the DTS determination.

Although, numerical tools to resolve mechanical problem have been widely developed over the last decades, the behavior prediction of passive isolators is still performed on prototype using experimental means. In fact, it has to be emphasized that it cannot be determined resorting to traditional FE methods without resorting to a complex tuning of the model by experimental tests [30]. Therefore, the main purpose of the thesis is to develop a scientific approach to remedy the issues using traditional finite element analysis.

To fulfill the objectives of the thesis a scientific approach was developed. This approach is divided in two main parts, which work in parallel, with the support of a third one (see figure 1). The experimental part of the scientific approach consists to determine the dynamic transfer stiffness (DTS) of the resilient mounting element. This DTS is considered as the reference on which the results of the other would be compared. The other is constituted by several numerical inquiries including dynamic quasi-static simulation, normal modes analysis and frequency response simulation to determine the DTS of the resilient mount FE model. If the numerical model are correlated with the first experimental test results, numerical simulations should allow to reduce drastically, the time and cost associated to the determination of the DTS of a similar resilient mount. The developed FE models should then allow to study the dynamic response of RME with other geometries.

But at first, the numerical simulation of the RMS vibration response requires to know the elastomer mechanical characteristics, which can be determined by performing DMA tests on several material samples which constitutes the damping part of the RME.

To model the mount elastomer behavior, it is possible to use, either a linear elastic law whose the Young modulus is set accounting for the pre-loaded RMS working point (if it is known), supposing a linear behavior of the RME at the working point, or an hyper-elastic law which allows for modeling the stiffening of the compressed elastomer.

Anyway, the utilization domain of the chosen behavior law must be defined according to the frequency work range, the static deformation where the RMS should work and the deformation amplitude created by the excitation (from the engine) of the RMS.

Comparing a model based on a linear elastic law for the rubber to another based on a hyper elastic one should allow to know if a linear elastic law is sufficient to model correctly the elastomer behavior under a static pre-load. If the discrepancies are small, it would be possible in the future to use the more simple linear elastic law to model the elastomer behavior.

Unfortunately, the influence of temperature on the dynamic transfer stiffness is not considered due to a lack of time during the thesis. However, it could be an interesting aspect for a deeper investigation.

The start point of the thesis and commonly the provided information about the resilient mount element is the static deflection curve of the element. This curve represents the static displacement of the top of the

tested element under a compression load. Thus, the first step in the quasi-static simulation that model the element under the working load. The working load for the studied element in the thesis is 7.5 tons load, which corresponds to 73 KN. Using reverse engineering and acknowledging the matching displacement the young modulus or the equivalent coefficient in the hyperelastic law. The method and FE model are described in the III.A.1 part.

Then, using the resultant strain deformation field is possible to initiate the dynamic mechanical analysis (DMA) which requires, a static deformation, a dynamic deformation and a frequency range of study as input test parameters. The DMA tests results, such as Young modulus and tangent angle loss (damping) would provide updated data at the working point considering here the effect of pre-compression. A first comparison is effected between the strain fields and decisions could be done concerning the most suited material law.

In addition to the static simulations, normal modes analysis are performed -experimental and numerical- to acknowledge some significant area in the frequency where possible unexpected RME behavior could occur. In consequence, it ensures a better certainty during frequency response post-treatment and thus about the results.

In parallel of the numerical process, a classical experimental campaign to characterize the RME and predict his behavior depending on the input excitation is performed. This campaign is constituted by two stages. At first, a gradually static compression is achieved to verify the provided data from the RME manufacturer. Then the working load is applied on the tested element. After the compression a dynamic analysis, more precisely a frequency response analysis (FRA), is accomplished. The obtained experimental results would be the reference in this work.

This reference would be confronted to the results of the numerical frequency response analysis and of the analytical model to validate the established scientific approach. This confrontation would verify the cogency and coherence of the developed work in this thesis.

The scientific procedure is explicitly displayed in the figure 1 and the steps and components are detailed and endorsed in the parts of this thesis. The PhD work stages are in purple boxes and the related results are in blue boxes in the figure.

Therefore, the presented parts in this work are following the procedure. In the first part on the bibliography, a general presentation of the different industrial domains and their respecting problematics where resilient mounting elements are employed (chapter I.A.1.) is portrayed. The use of passive isolators (RME) in the marine engineering field is displayed in the two following chapter, treating, at first, of the direct environment, indeed engines room (chapter I.A.2.), and about their specific role and surrounding problematic (section I.A.3.).

Then, after a brief introduction on mathematical features (chapter I.B.1) that appear in the thesis, particular reflections about on the theoretical background exploited are enlightened especially about the developed work on passive isolator theory (chapter I.B.2.), vibration and damping considerations (chapter I.B.3.) and material perspectives (chapter I.B.4.).

To complete the work of the two previous chapters, a review on the different potential RME characterization methods with the related studies is delivered, split into three main chapter representing the type of approach, the experimental (chapter I.C.1.), the analytical (chapter I.C.2.), the numerical (chapter I.C.3.).

Additional explanations of the ISO standards regarding the practical aspects essential in this work, are presented in the third part: RME experimental characterization (chapter I.D.1.), viscoelasticity characterization and aspect of polymers (chapter I.D.2.) and special features of the finite elements software's (chapter I.D.3).

Then, a small conclusion recapitulate the important points discussed in the bibliography and the specificities of the thesis are enhanced (part I.E).

To allow the proceedings of the scientific approach, some preliminary studies are completed concerning the experimental means (part II.A.) and numerical pre-investigations about the RME model concerning his static aspect (part II.B.) and natural frequency modes (part II.C.).

Furthermore, the dynamic mechanical analysis settings are outlined (part III.A.) and the resulting outcomes are examined (part III.B.).

The aforementioned experimental campaign is described in two parts, the followed methodology and settings (part IV.A.) and the obtained results (part IV.B.).

Finally, the numerical dynamic simulation results are presented, and the related results compared to the experimental results (part V.A.) and the development of an analytical model disclosed (part V.B.).

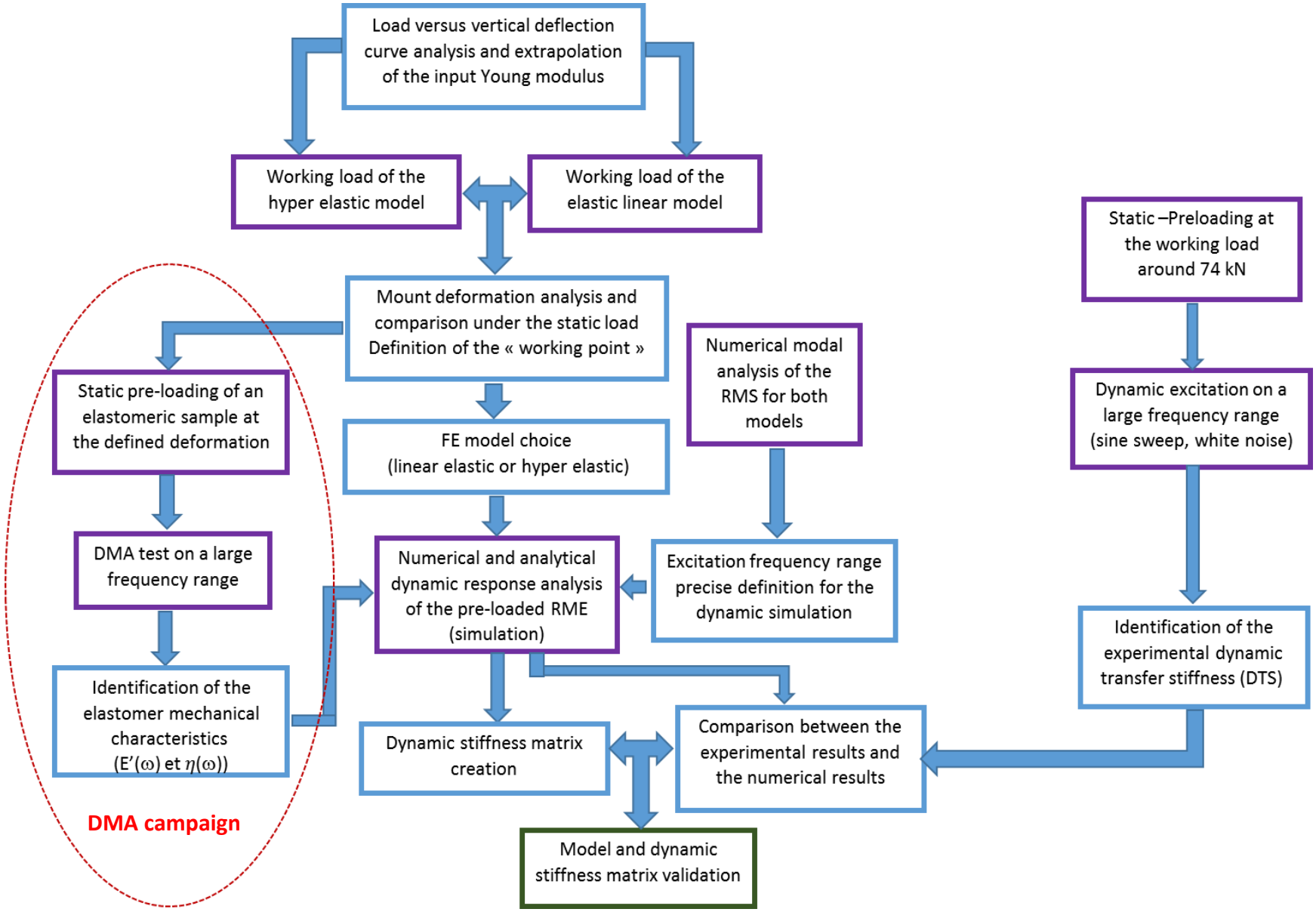

Figure 1: Developed RME dynamic characterization procedure

I. BIBLIOGRAPHY

The bibliography presented in this work contains a state of art on passive isolators, including a wide description of the ones used marine industry. The aim was also to understand the specificities of the linked thesis problematics with a study of the direct background of in marine engineering. It also integrates a theoretical background to understand the hypothesis adopted in the presented work. Then, current methods to determine the RME DTS will be prospected. Thereafter, the ISO standards and theirs specific and crucial points, which determine the validations of experiments performed in the framework of the thesis, are also explicitly described. Finally, the bibliography will be concluded and the specificities of the thesis will be reviewed.

A. PASSIVE ISOLATORS

In this part, the utilization of passive isolators in different industrial fields is reviewed to put in perspective the specific problematics of their use. More specifically, the use of resilient mounting elements in marine engineering sector is described. Indeed, the use of passive isolators to reduce vibrations levels for several purpose, such as the comfort of passengers or avoid irreversible damages on structures, is widely spread in different application with different problematics, ambitions and surrounding environments. The subjects appear frequently in the transport industry such as aeronautic, aerospace and automotive or in specific fields where the devices are sensitive such as precision mechanic or micro mechanic.

At first, most of the applications fields of the passive isolators will be presented with the related problematics. Then, the approach elements will focused more on the application in naval environment especially the marine engineering sector by presenting the background specific to this field. Finally, the diversity of the passive isolators used among the marine field will be quickly evoked before presenting the studied resilient mount studied in this thesis: the T200 produced by Vulcan for Wärtisila. However, the specificities of the thesis will be explicitly approach in the conclusion part of the bibliography.

1. Passive isolator applications fields

In fact, the application field of the passive isolator is quite wide. It is related to all fields, directly or indirectly, that are connected to general problematics about vibrations. From a physical point of view, vibrations are mechanical waves that propagate through solids and liquids. Vibrations are generally generated by physical periodic oscillations. Engines, motors, and all mechanical actuators could be considered as a source of oscillations. When the excitation frequencies are close to natural frequencies of the structure, this latest goes into resonance and vibrations can generate fatigue of the material leading to unwanted stresses and strains. That is why the transport industry give a preponderant place to passive isolators in applied research. The particular use of passive isolators linked to transverse problematics could be common to several fields. However, there are few of those interdisciplinary problematics due to the variability and specificities of the issues of each environments. Even if the oscillations amplitude is very low with a long sine period, it could damage really sensitive devices due to the relative low stiffness of those devices, which decreases the natural frequencies of the elements.

Indeed, in precision mechanics where the instrumentation are susceptible to react to a very low vibrations level, the focusing aspect of passive isolators is the reduction of the isolator stiffness. Actually, in this field, the used devices have a very low mass due to the small dimensions. Thus, to lower the natural frequencies of the component, the lowering of the stiffness is necessary [31]. The objectives is to acquire wider range of frequency isolation, which could lead to the obtaining of relative negative stiffness using a specific mechanism [32].

Another field in which the same problematics appear is the aerospace industry. Indeed, the instrumentation used in for spatial applications is also highly sensitive to vibrations with small dimensions and low mass [33]. Moreover, specific features encountered in space are the micro gravity [33] and the very low temperture environement [34] which can potentially have a significant effect on the properties of elastomeric used material inducing the variation of the intrisic characteristics values (increasing of the stiffness, decreasing of the viscosity) .

Those material are not only used for critical environement but also in more common situations encountered for example in aeronautic sector. In this sector, the influence of the excitation frequency range and temperature is extensively studied [35], especially where passive isolators are used to damp vibration levels induced by rotative element such as helicopter rotor. The objectives is to propose an accurate predictive model integrating hyperelatic and dissipative constitutive equations to be able to obtain the response of the investigated system in function of the working conditions (temperature and cyclic loadings). The variation of those working conditions are the main cause of fatigue phenomena, when the passive isolators endure a great number of cycles. Therefore it is necessary to study the effect of fatigue on the isolators [36] especially if it could lead to the damaging of the isolator.

Elastomeric materials are also extensively used to protect structures against shocks. The principal quality of thoses materials is their high dissipative properties, usefull to absorb shock energy. The response of structures to shock load is characterized by high deformation amplitude and sometimes high strain rates. The absorbtion of shock is particulary treated in the military field, especially in design of equipment embarked in sub-marine [37].

However, the shock issues are not exclusively related to military applications. This problematic is also widely treated in transpsort industry, especially in the automotive sector, where it is linked to the engine/road interactions, more preceisely when the engine suspensions interact with the irregularities of the roads. The resulting multiple shocks may be sources of discomfort for passangers and the studies performed in this sector usualy focus on the reduction of this discomfort [38] [39].

Of course, reducing the vibration levels in order to improve the comfort of passengers is not limited to the automotive sector.

2. Maritime applications features

In this section, the background concerning the use of passive isolator in maritime industry will be presented, and the problematic of passengers comfort and the possible source of discomfort will be discussed.

As it was previously introduced, the comfort on board ships, especially on yachts and cruise ships, is highly requested for both passengers and crews. This comfort is may be affected mainly by the structure-born noise which often originates from all the machinery, generally located in ship bottom. It propagates along the ship structure and reaches the accommodations areas, usually located at mid-height or at the top of the ship where high level of comfort is necessary. Figure 2 shows the localisation of those accommodation areas in cruise ships and mega-yachts.

Figure 2: General view accommodations for a cruise ship (left) and a mega-yacht (right) [59][60]

Among all the on board machinery, it has been evoked that the principal source of vibrations are the engines [11] [12] [13] which are generally two or 4-stroke diesel engines for civil ships.

Figure 3 features a 3D CAD model of a 4-stroke engine supported by passive isolators, displayed in black at the lower part of the engine. The main role of those passive isolators is to reduce the transmission of the vibrations toward the engine foundation

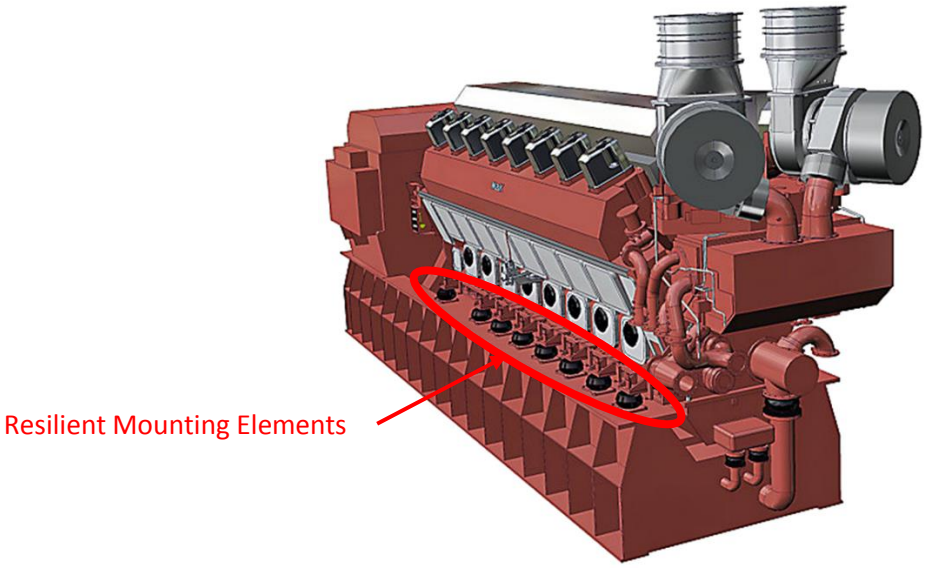

Figure 3: 3D model or the "VM 43 C Generator Set" provided by the Caterpillar Company [61]

The passive isolators on which the engines lies are called in consequence *resilient mounting element,* the term mostly because they often must endure a high gravity load which generally leads to high compression strain inside the elastomeric constitutive material. This high compression is often a determinant characteristics of the passive isolators used in the marine engineering sector.

According to the ISO 10816-6 standard [40], for engines categorized in class 5, the maximum possible dynamic excitations transmitted to the resilient mount from the engine is the following particulars:

- From 1 to 10 Hz: a vertical displacement of around 0.6 mm
- From 10 to 200 Hz: a vertical velocity 40 mm/s

These average values could be used in the experimental campaign as a realistic input signal if the excitation is capable to maintain it. Furthermore, comparing the maximum dynamic amplitude to the static pre-load displacement presented below, this leads to considerations concerning the linearization of the RME behaviour and thus model simplifications (see section I.B.5).

3. Passive isolators for marine applications

In this part, among the entire resilient mounting elements used in the marine engineering sector, a few of them will be displayed. Then the RME chosen in this thesis will be presented and all the data provided by the manufacturer will be exposed.

a) Different types of devices

There exists a great number of resilient mounting element produced by several manufacturers. Each of them have their own characteristics and application. The figure 4 features three RME studied in the Ship Noise Vibration Laboratory (SNVL).

Figure 4: From the left to the right, T75, RK658, and M157

b) Studied RME: T200

The resilient mounting element considered in the framework of this thesis, is called T200, produced by Vulcan for Wärtsila. This RME is composed by three parts. The top casting is tightly connected on the engine foot and constituted by a relatively rigid material (commonly steel). It covers on the intermediate parts which is constituted by a damping material (rubber) with an hardness of 75 shore A. This latter is supported by a metallic base frame, solidly connected to the structure of the ship foundation and also constituted by a relatively rigid material (commonly steel). Figure 5 features the T200 under testing and Figure 6 presents a typical RME with the connections to the engine on its upper part and to the foundations (ship structure) on its lower part.

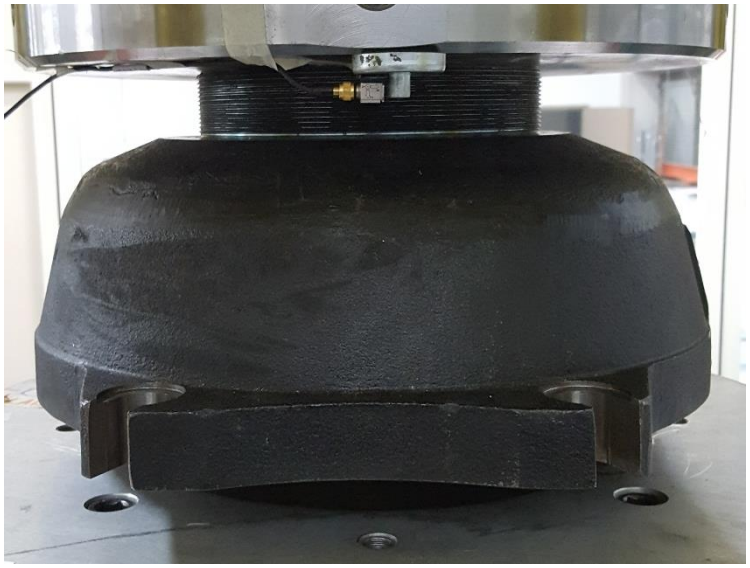

Figure 5: View of the T200 resilient mounting element under testing

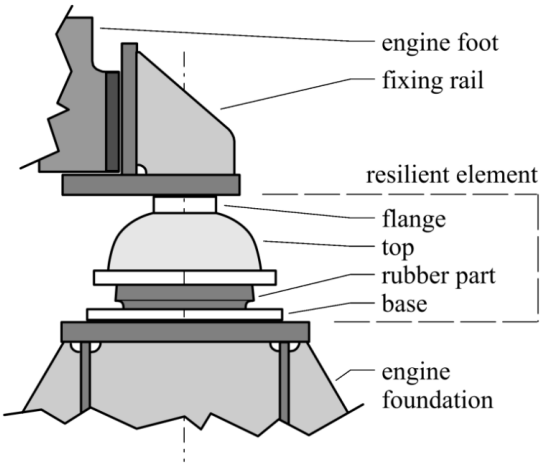

Figure 6: RME with connections [41]

Figure 7 presents the static compression curve of two resilient mounting elements: T200 and T200S. In Figure 7, the **compression load**, expressed in **kN**, is in **ordinate** whereas the corresponding **compression displacement**, expressed in **mm**, is in **abscissa**.

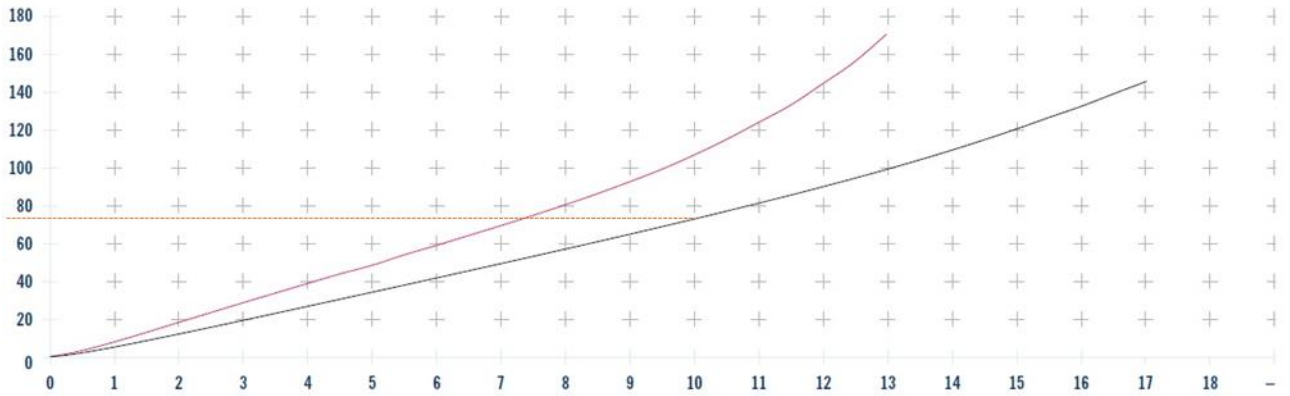

Figure 7: Compression curves of the T200 (black) and T200S (red) with the T200 working point

The intersection of the black curve (T200) and the orange curve, which represents the working load, is a unique point, the working point. This T200 curve shows that a working load of 74 kN applied on the T200 leads to a displacement of about 10 mm.

It is of great interest for the Marin industry, diesel engines manufacturers and shipyards to know precisely the dynamic behaviour of a given resilient mounting element at both low and high frequencies. As an experimental characterization of a full scale RME remains quite long and costly, such companies are particularly concerned with the development of a procedure based on material characterizations coupled with numerical or analytical simulations.

In order to achieve this objective, the PhD work of Lorenzo Moro [41], performed in Trieste University (SNVL laboratory) aimed to develop a procedure allowing, amongst others subjects, the characterization of an RME in the high frequency range (100-1000Hz). Such procedure was based on non-linear dynamic simulations involving some hyper-elastic behaviour law such as the Yeoh hyperelastic law. The RME was the same as in the thesis, the T200.

Nevertheless, this thesis was not the only one approaching the RME problematics. Several studies exists in the literature, investigating RME experimental characterization, numerical tool implementation for the DTS determination, and researching potential analytical model to quickly predict the RME behaviour. The mentioned works will be, deeply reviewed in section I.C.

B. THEORETICAL BACKGROUND

1. Mathematical considerations

a) Tensors

A second-order tensor, so called $\bar{\bar{T}}$ in 3 dimensions contains 9 values and can be formally presented as a matrix.

A tensor is considered symmetric if the following relation exists:

$$T_{ij} = T_{ji} \quad (1)$$

b) Invariants of tensors

Invariants are elements that remain unchanged when an application, here defined by a tensor, is applied to them. Such invariants are involved in the determination of tensor eigenvalues and eigenvectors govern by the following equation

$$\det\left(\bar{\bar{T}} - \lambda\bar{\bar{I}}\right) = 0 \quad (2)$$

Where $\bar{\bar{T}}$ is a symmetric tensor and λ is the eigenvalue vector.

It can be shown that invariant also appear in the resulting characteristic equation:

$$-\lambda^3 + I_1\lambda^2 + I_2\lambda + I_3 = 0 \quad (3)$$

Therefore, invariants of tensor $\bar{\bar{T}}$ are independent from the basis uses to define such tensor and can be calculated as follows:

$$I_1 = tr\left(\bar{\bar{T}}\right) = \sum T_{ii} \quad (4)$$

$$I_2 = \frac{1}{2}\sum\left(T_{ii}T_{jj} - T_{ij}T_{ji}\right) \quad (5)$$

$$I_3 = det\left(\bar{\bar{T}}\right) \quad (6)$$

2. Four pole parameters theory

The ISO 10846 standards are widely accepted as a sound reference for the experimental measurement of the resilient mountings dynamic transfer properties both in low and in high frequency ranges. Those properties are evaluated considering the diesel engine as a suspended vibration source. According to such approach [42] [43] [44], the characterization of a resilient mounting system is achieved by making reference to a three block system (Fig. 8): the vibration source (i.e., the diesel engine), the isolator and the receiving structure (i.e., the ship structure). The application of the procedure supposes that only passive linear-response resilient elements are studied and that the contacts between the three blocks are treated as a series of independent single-point-connected systems.

According to ISO 10846-1, the vibroacoustic characteristics of a resilient mounting are mainly described by its dynamic transfer stiffness $k_{i,j}(f)$.

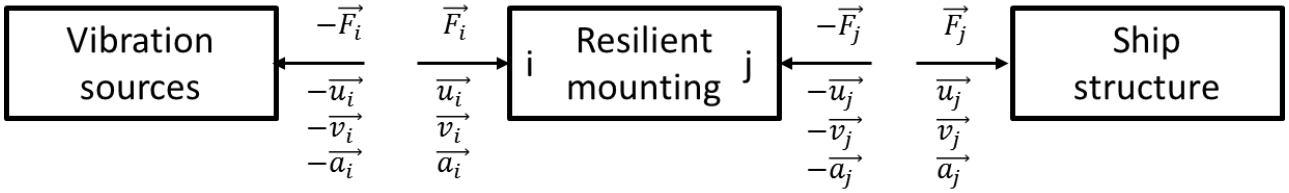

Figure 8: Four pole parameter theory

The dynamic transfer stiffness is defined as the ratio between the dynamic force on the blocked output side of an isolator $F_{jb}(f)$ and the complex displacement on the driven side $u_i(f)$. To illustrate the concept of dynamic transfer stiffness, the simple case of a unidirectional transmission of vibrations through an isolator is considered in the following. If $k_{i,i}(f)$ and $k_{j,j}(f)$ are the driven-point stiffnesses when the resilient element is blocked at the opposite side (u_i and u_i are null, respectively) and $k_{i,j}(f)$ and $k_{j,i}(f)$ denote the ratio between the force at the blocked side and the displacement on the driven side. The equilibrium equations of the isolator can be written for each frequency as:

$$\begin{cases} F_j = k_{i,i}u_i + k_{i,j}u_j \\ F_j = k_{j,i}u_i + k_{j,j}u_j \end{cases} \quad (7)$$

In this system, the isolators (RME) exerts on the receiving structure a force F_j which may be derived from the definition of the driven-point stiffness of the receiving structure, that is:

$$k_{dp} = -\frac{F_j}{u_j} \quad (8)$$

So, F_j may thus be given by:

$$F_j = k_{j,i}\,\frac{k_{dp}}{k_{j,j} + k_{dp}}\,u_i \quad (9)$$

Furthermore, if the DTS of the RME is considered negligible in relation to the driving-point stiffness ($|k_{j,j}| < 0.1\ |k_{dp}|$) the previous equation can be expressed as:

$$F_j \approx F_{jb} = k_{j,i}u_i \quad (10)$$

This formula is the one that is used to calculated the DTS of the RME.

3. Vibration and damping considerations

In this part the vibration considerations taken in the thesis are discussed. At first, two oscillating systems of 1 degree of freedom (1DOF) will be exposed. Both will be constituted by a mass and a stiffness, but one will have a different kind of damping. In this studied systems, the related damping is associated to the potential viscoelasticity of the system. The study frame in this section will be limited to the linear viscoelasticity.

a) Damped oscillating system models

The modelling of a 1D damped oscillating systems was among the earliest discussed topic in mechanic. The modelling consists in the combinations of elementary models such as spring, mass, or dashpot for example. The associated models of these elements describe often related to a rheological approach. Several of them, they relate the external applied stress or similar phenomenon (Force, pressure) and the resulting strain.

- **Viscous damping**

A first model to describe a 1DOF oscillating system with damping property integrates a viscous damping to model the viscosity.

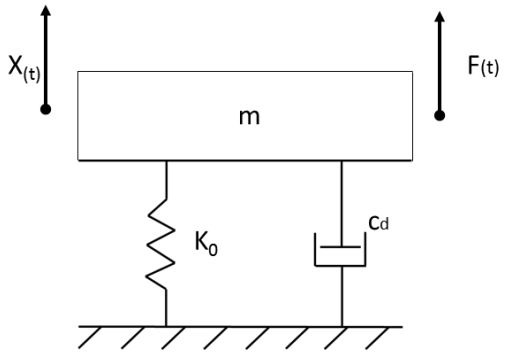

Figure 9: 1 degree of freedom oscillating system with viscous damping

The equation that governs the oscillations of the system may be expressed as:

$$m\ddot{X} + ic\dot{X} + K_0 X = F(t) \quad (11)$$

Let us express the time evolution of in the complex form:

$$F(t) = F_0 e^{i\omega t} \quad (12)$$

The resulting displacement, velocity and acceleration may then be expressed as:

$$X(t) = X_0 e^{i\omega t} \quad (13)$$

$$\dot{X}(t) = i\,\omega X_0 e^{i\omega t} \quad (14)$$

$$\ddot{X}(t) = -\omega^2 X_0 e^{i\omega t} \quad (15)$$

It is therefore possible to obtain the ratio between displacement amplitude X_0 and force amplitude F_0 which can be expressed as following:

$$\frac{1}{(K_0 - m\omega^2) + ic\omega} = \frac{X_0}{F_0} \quad (16)$$

- **Structural damping**

A second model to described the same oscillating system integrates a structural damping.

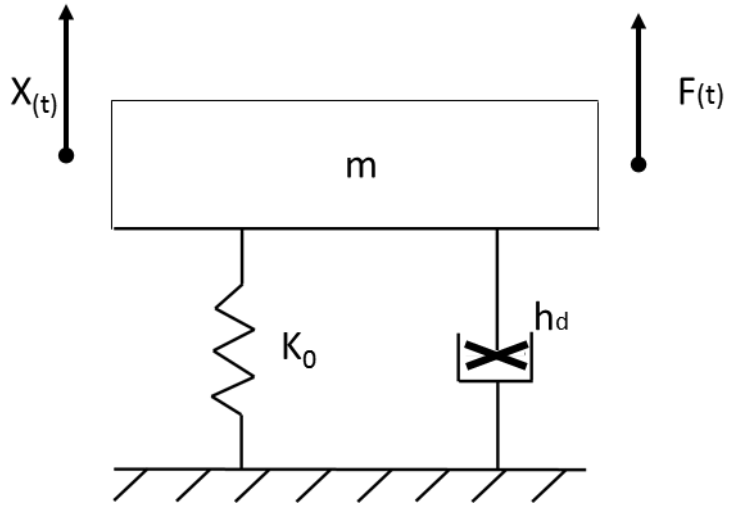

Figure 10: 1 degree of freedom oscillating system with structural damping

Considering a structural damping of the involved material, expression 16 becomes:

$$\frac{1}{(K_0 + i\ h_d) - m\omega^2} = \frac{X_0}{F_0} \qquad 17$$

Expressions 16 and 17 are the so-called transfer functions. The structural damping can also be designated with the Greek letter η and called loss factor.

The structural damping and the viscous damping represent in theory the same physical aspect of a material or system. Therefore, it exist a relation between the two dampings. This relation can be expressed as follows:

$$c = \eta\ \times m \times \frac{{\omega_0}^2}{\omega} \qquad 18$$

where ω_0 refers to the natural frequency of the system.

At the resonance circular frequency ω_0 when ω is equal to ω_0, the previous equation becomes:

$$c = \eta\ \times\ m\ \times \omega_0 \qquad 19$$

b) Transfer function

When the structural damping of the material is considered, the transfer functions are complex numbers. Considering time-invariant systems, if the input physical quantity is related to a motion and the resulting output is a force, the different complex transfer functions of the system are defined as follows:

- The *accelerance* is the ratio between the acceleration and the force:

$$A_{ji}^{*}(f) = \frac{a_i^{*}(f)}{F_j^{*}(f)} \quad (20)$$

- The *mobility* is the ratio between the velocity and the force:

$$V_{ji}^{*}(f) = \frac{v_i^{*}(f)}{F_j^{*}(f)} \quad (21)$$

- The *admittance* is the ratio between the and the force:

$$D_{ji}^{*}(f) = \frac{u_j^{*}(f)}{F_j^{*}(f)} \quad (22)$$

Moreover, the inverse of above functions are defined by the following expressions:

- The *apparent mass* is the ratio between the force and the acceleration:

$$M_{ji}^{*}(f) = \frac{F_j^{*}(f)}{a_i^{*}(f)} \quad (23)$$

- The *impedance* is the ratio between the force and the velocity:

$$Z_{ji}^{*}(f) = \frac{F_j^{*}(f)}{v_i^{*}(f)} \quad (24)$$

- The *dynamic stiffness* is the ratio between the force and the displacement:

$$K_{ji}^{*}(f) = \frac{F_j^{*}(f)}{u_i^{*}(f)} \quad (25)$$

It is worth noting that the input physical quantity can also be the Force and the output one can be a variable describing the movement of the considered structure. Furthermore, if the same physical quantity is measured in both point, the transfer function is called “transmissibility”.

The following figure represents a system where i and j denote the points where the physical quantities are measured:

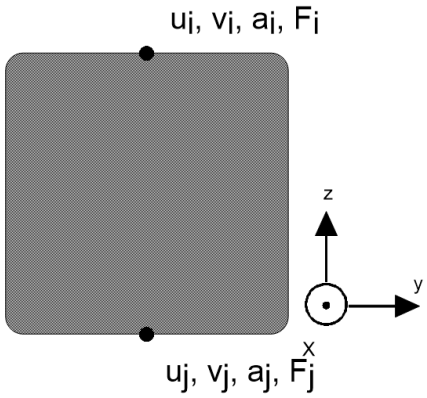

Figure 11: Schematically representation of an element considered in the single point theory

Considering the input and output as 6-degree of freedom points, the following convention is established:

- Translation/force in x direction : 1
- Translation/force in y direction : 2
- Translation/force in z direction : 3
- Rotation/torque in x direction : 4
- Rotation/torque in y direction : 5
- Rotation/torque in z direction : 6

Then, the expression of a transfer function becomes as in equation 23:

$$K_{i3\,j5}{}^{*}(f) = \frac{F_{j5}{}^{*}(f)}{u_{i3}{}^{*}(f)} \qquad 26$$

Considering the equation 14 and 15, the equation can be expressed as:

$$K_{i3\,j5}{}^{*}(f) = \frac{F_{j5}{}^{*}(f)}{u_{i3}{}^{*}(f)} = i \times 2\pi f \times \frac{F_{j5}{}^{*}(f)}{v_{i3}{}^{*}(f)} = -(2\pi f)^2 \frac{F_{j5}{}^{*}(f)}{a_{i3}{}^{*}(f)} \qquad 27$$

Of course, the unit of the transfer function depends on the involved physical quantities. The physical quantity amplitude may be expressed in decibel (dB) as unit. This level should be compared to a reference level to be represented in graphics as Bode diagram. The use if this level is often adopted in large scales where a logarithmic scale is needed for the representation. This level could be expressed by the following equation:

$$L_{TFK}(f) = 20 \times \log\left(\frac{K}{K_{ref}}\right) \qquad 28$$

The reference level is genrally arbitrary fixed to 1 N/m for a stiffness, 1 N/(m.s^{-1}) for an impedance and 1 N/(m.s^{-2}) for an apparent mass.

4. Material perspectives

One of the main element of the procedure developed in this thesis is the integration of the viscosity in a model (numerical or analytical), in order to simulate the damping properties of the RME and the hyperelastic features of the constitutive rubber.

In this part, the specificities of the behaviour of the material considered in this thesis will be discussed. The rubber used to build resilient mounting systems is generally a vulcanized rubber with carbon filler. The rubber behaviour can generally be separated in two main non-coupled components, the viscosity and the hyperelasticity.

This separation is helpful when setting a numerical model. At first, a suitable constitutive law to model the rubber hyperelasticity is chosen among the ones available in the literature. Then, a specific material law or a discrete damper, similar to the ones presented in section I.B.3, can be used to simulate the viscosity of the system. Rubber materials are commonly considered as isotropic and nearly incompressible. For convenience, the rubber studied in the framework of this thesis is considered as incompressible so its Poisson coefficient is supposed to be equal to 0.5.

At first, some general features describing the materials behaviour will be presented in subsection ***a***. Then, the viscosity will be examined in subsection ***b***. The rubber hyperelasticity, as for it, will be discussed in section c. Finally, two different material laws used to model the rubber will be compared in section d and relations between parameters that characterize these constitutive laws will be derived.

a) Material behaviours

To describe and model both hyperelasticity and viscosity, two physical quantities were introduced: the Deborah number and the Weissenberg number [45]. The Deborah number (De), which integrates solid and fluidic behaviours of a material, links its elasticity to its viscosity. For a determined load and resulting deformation, this number is the ratio between the relaxation time, consequence of the deformation, and its observation time. It can be expressed ad follow:

$$De = \frac{t_o}{t_r} \tag{29}$$

where t_o is the time during which the deformation is observed, and t_r is the relaxation time corresponding to the end of the deformation.

Therefore, for a determined material, at low Deborah number (nearly 0), the material has a fluidic behaviour. On contrary, a high Deborah number indicates that the material behaves mostly elastically.

The Weissenberg number, as for it, relies the elasticity and the viscosity of a material. For the same determined solicitation, this number is the ratio between resulting elastic and viscous forces:

$$We = \frac{elastic\ forces}{viscous\ forces} \tag{30}$$

$$We = \frac{t_r \times \mu \times \dot{\gamma}^2}{\mu \times \dot{\gamma}} = t_r \times \dot{\gamma} \tag{31}$$

where t_r is the relaxation time, $\dot{\gamma}$ the strain rate and μ the dynamic viscosity.

By introducing above numbers, it is possible to create the so-called Pipkin diagram depicted in Figure 12.

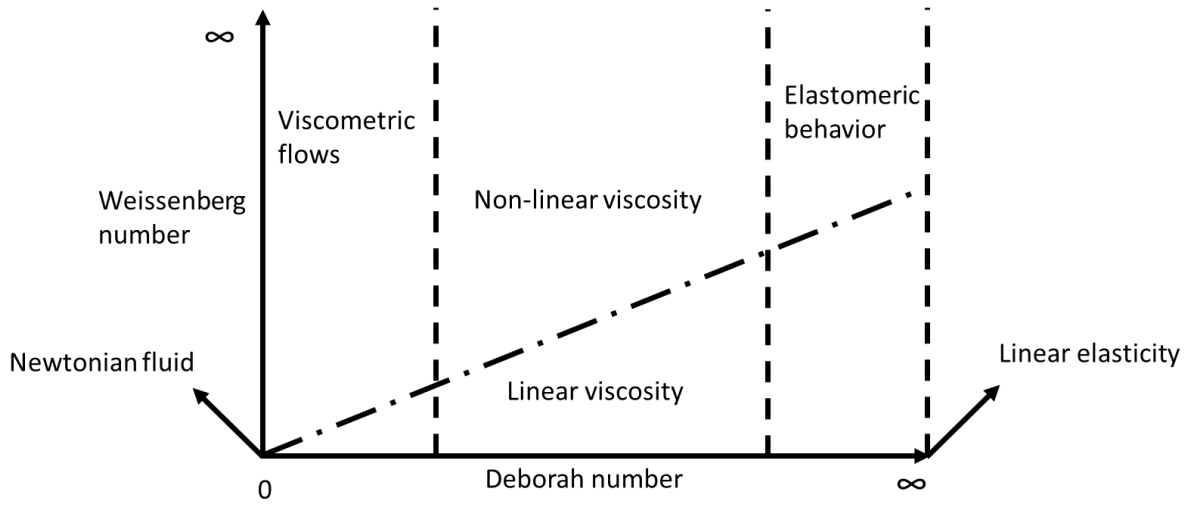

Figure 12: Pipkin diagram

This diagram may be considered as a qualitative representation of several material behaviours integrating their respective viscosity and elasticity. The limit between the viscometric flows and the rest of the diagram is arbitrary fixed. It is the same case for the elastomeric behaviour area. A material in which the Boltzmann principle is not verified, has a non-linear viscosity behaviour. The Boltzmann superposition principle asserts that, when several successive loadings are applied on a viscoelastic material, every loadings contribute independently to the final state of the material. There is no coupling effect.

It is interesting to note that the linear elasticity and Newtonian fluid suggests a perfect behaviour of the material, which is nearly impossible to obtain in reality.

b) Viscosity and DMA

At first, it is necessary to investigate the influence of the viscosity on the material behaviour, especially regarding the stress-strains relations. When a material is subjected to deformation, the viscosity designed all the internal mechanisms of the materials that are opposed to the applied deformation [46]. The viscosity is present in all materials but constitutes a fundamental characteristic of fluidic and elastomeric materials. On the molecular scale, the viscosity represents the frictions between the material molecules or molecular chains when subjected to deformation, which is the case for the filled rubber. In consequence, the viscosity induces an increase of the rubber internal temperature and then depends on the environment temperature, an energy loss due to this friction. When the material is successively loaded and unloaded, friction between molecules engenders hysteresis as illustrated by the stress-strain curve depicted in Figure 13.

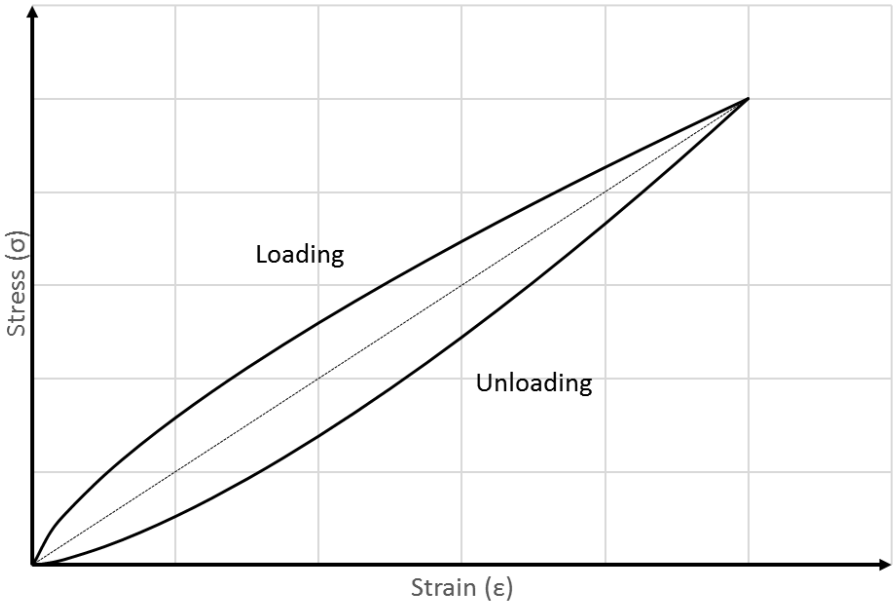

Figure 13: Qualitative representation of the hysteresis engendered by the material viscosity

Combining the viscosity to a Hook law, the resulting stress-strain relation is not anymore proportional. When a deformation (or a load) is applied on the material, the resultant stresses integrating the viscosity are higher than the stresses obtained when considering the Hook law represented by the dotted line in Figure 13. On the contrary, when the material is unloaded, the resultant stresses are lower.

The area between “loading” and “unloading” curves represents the energy loss during one cycle. It is worth noting that the smaller the area, the lower the viscosity. Therefore, “loading” and “unloading” curves converge to a straight line when the viscosity decreases.

It exists several types of viscosity. However, two types are generally used in mechanic: the dynamic and cinematic viscosities, which are related by the following expression:

$$\upsilon = \frac{\eta}{\rho} \qquad 32$$

where, υ is the cinematic viscosity, η the dynamic viscosity of the material and ρ the density.

For an incompressible material, when the test are performed at constant temperature, both viscosities are proportional. In this thesis, only the dynamic viscosity will be studied.

Considering the filled rubber material, it should be expected that the rubber has an elastomeric behaviour with at best a linear viscosity. In the case where such elastomeric material has a linear viscosity, the applied stress on the material should be proportional to the resultant strain rate, respecting the following equation:

$$\sigma = \eta \frac{d\varepsilon}{dt} \quad 33$$

where σ is the applied stress, η is the dynamic viscosity of the material and ε is the strain.

When modelling the behaviour of a viscoelastic material or more generally a system with damping properties, as rubber, it is possible to associate dampers and springs to represent its behaviour [47].

The viscosity of a material may be directly measured but the influence of environmental parameters such as temperature and external stresses has to be investigated.

As previously mentioned in part I.B.3, several types of damping can be used to model the viscous behaviour of a material. It is necessary to connect these damping to measurable material characteristics after the determination of the related parameters using a specific test type.

Among the several tests performed on rubber-like material, the dynamic mechanical analysis (DMA) test provides information about the material mechanic behaviour. The main characteristics measured through the DMA test are the compression and extension Young moduli (E), the shear modulus (*G*), and the tangent angle loss $(\tan\delta \text{ or } \eta)$ [48]. The tangent angle loss, which features a phase difference between the sinusoidal applied load and the strain response of the material, is directly linked to the structural damping property of a material.

Above material characteristics depend on the temperature, the initial static strain and the dynamic strain related to the frequency of the applied dynamic excitation.

The special features related to the practical aspect of the DMA test will be detailed in section II.D.2 with details on the method and the interpretation of the results.

Figure 14 shows typical evolutions of the Young modulus and tangent angle loss with the temperature. Figure 15, as for it, shows typical evolutions of the Young modulus and tangent angle loss with the frequency.

Those essential features are the principal outcome parameters when performing a DMA test on a polymer such as filled rubber .

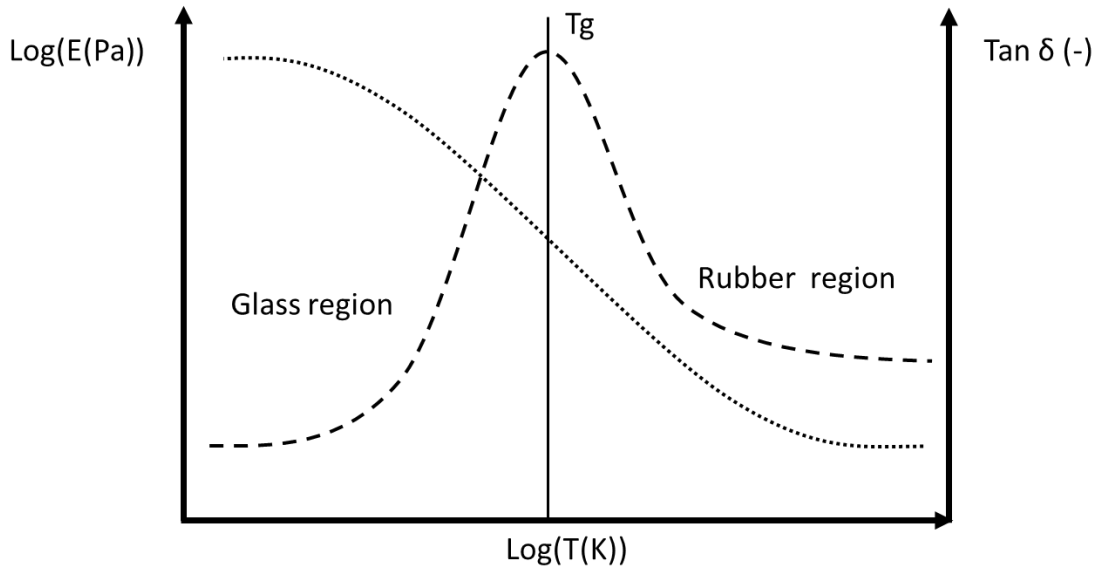

Figure 14: Typical evolutions the tangent angle loss and Young modulus with the temperature

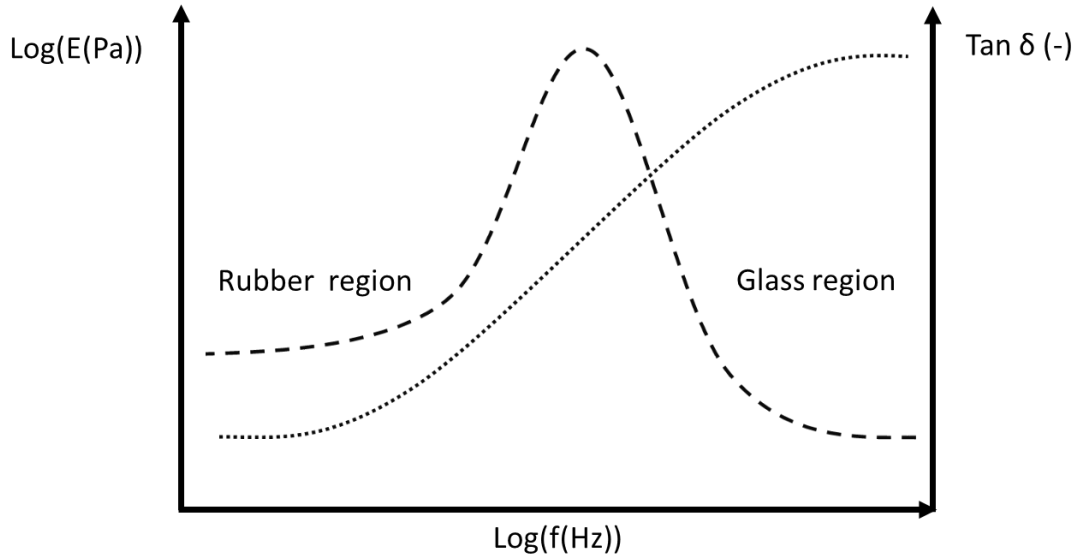

Figure 15: Typical evolutions of angle loss and Young modulus with the frequency

The Young modulus (in Pascal), featured by the small dot lines on graphics above decreases with the temperature (in Kelvin) and increases with the frequency. It is worth noting that all physical quantities are generally plotted in logarithmic scale in order to represent large variations. For, example, large variations of the Young modulus are commonly measured when the excitation frequency varies from 1 to 10^3 Hz.

The tangent angle loss, as for it, featured by large dot lines, increases with the temperature up to a maximum, the so-called glass transition temperature (*Tg*), and then decreases. The transition temperature delimits two regions, the **glass region** and **rubber region**. These regions characterize the molecular arrangements in the polymer, which depend on the temperature, the strain and the strain rate of the material. As shown in Figures 14 and 15, frequency and temperature have symmetrical effects on the young modulus and tangent angle loss.

It is also worth noting that the excitation frequency has an inverse effect on the two main characteristics of the polymer. When performing a DMA test, only one parameter like the frequency or the temperature is varied, the other one remaining constant. For example, the evolution of the Young modulus as function of the frequency is performed at constant temperature.

As a consequence, a frequency-temperature superposition principle is often used. Indeed, the evolutions of the Young modulus and tangent angle loss with the frequency at constant temperature (T_1) are the same that the one obtained at a different temperature (T_2) with the same other experimental conditions. The curves are just shifted on the eft or the right on the frequency axis, depending on the test temperature ($T_1 < T_2$ or $T_1 > T_2$). Using an empirical relation proposed by Williams, Landel and Ferry (**WLF**) [49], it is possible to obtain the related shift factor, or, in other words the ratio between the values of a parameter (viscosity, etc.) at the two temperatures:

$$log_{10}(a_T) = \frac{-C_1(T - T_r)}{C_2 + (T - T_r)} \qquad 34$$

where a_T is the shift factor, C_1 and C_2 are model constants obtained empirically, T the requested temperature and T_r a baseline temperature. This baseline is generally set as the glass transition temperature T_g of the material. It is important to note that using this equation requires the temperature T to be higher than the glass transition temperature T_g. In other words, expression *(32)* allows to estimate the shift factor to be applied on a curve at temperature T, as soon as T is higher than the glass transition temperature.

For polymers such as elastomeric materials, it is suggested to use universal constants for C_1 and C_2, when there is a lack of experimental data. These values are given as follows:

$$C_1 = 17.44 \qquad 35$$

$$C_2 = 51.6 \text{ K} \qquad 36$$

The perspective to use the frequency-temperature superposition principle and the WLF formula is convenient when the frequency study range is out of the acceptable frequency range of the apparatus while performing the test at the ambient temperature. Then, it is possible to obtain the equivalent curve at the ambient temperature within the requested frequency range, cooling or heating the material before the test.

c) Hyperelastic aspects

Once the global elastomeric behaviour and the viscosity have been explained, it is interesting to study the elasticity aspects of the filled rubber. In fact, the rubber does not behave linearly, i.e. the stress-strain curve is not a straight line. The relation between the strains and stresses derives from a strain density function [50]. The material may be considered as elastic due to its ability to return to its original state when the applied load is removed. A hyperelastic material can endure a significant strain level (more than 100%) and still return to its original state. Figure 16 presents a typical stress-strain curve of a hyperelastic material.

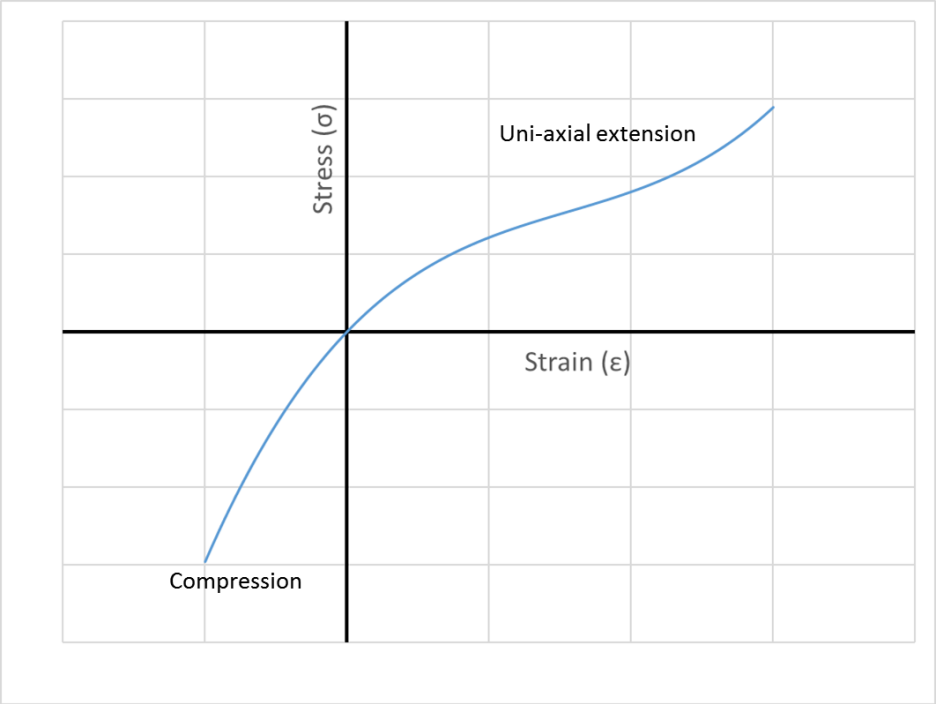

Figure 16: Typical stress-strain curve of a hyperelastic material

Regarding the hyperelastic behaviour of the elastomeric materials, the most important feature appears during its uniaxial extension. At first, the stress (σ) is almost directly proportionate to the strain (ε) when the strain is small, i.e lower than 10%. In this condition, the material behaviour may be considered as linear elastic. Once a deformation of the material reaches a certain level, the stress is no longer directly proportional to the strain. The stress-strain curve slope decreases first up to a specific strain level then increases. The rubber material behaves quite differently when submitted to compression. When the strain increases, the stress increases rapidly and tends toward infinity. This aspect of the behaviour is linked to the fact that the material is nearly incompressible. This incompressibility leads to consider that an equibiaxial extension induces the same effect on the material as a compression.

In this thesis, the investigated filled rubber is conveniently supposed as incompressible. Moreover, although the internal molecular arrangements are not perfectly regular in the material, the rubber elastomers are generally considered as isotropic.

To be able to predict the rubber behaviour, a hyperelastic model, similar to the Hook model, needs to be defined, expressing a relation between the stress and the strain.

Among the different hyperelastic models presented in the literature, one of the most suited for our application is the Yeoh model [51]. This model links the strain density function to the Cauchy-Green tensor ($\bar{\bar{C}}$), presented in the following section. The strain density function is a scalar value and relates to the energy stored in an elastic material during a physical transformation (deformation). This leads to the following expression:

$$W = \sum_{i=1}^{3} C_{i0}(I_1 - 3)^i \qquad 37$$

where I_1 is the first invariant of the Cauchy-Green tensor.

Therefore, to model completely the rubber hyperelastic behaviour, it is required to determine the three coefficients C_{10}, C_{20} and C_{30}. According to the hypothesis of small deformations, where the first invariant is nearly equal to three, the first Yeoh coefficient is predominant. Thus, a relation between this first coefficients and the young modulus of the Hook law may be established. This will be developed in the next section.

Considering the non-linear rubber behaviour, a fundamental feature is called the Mullins effect introduced by Mullins [52] in 1969. This phenomenon, exhibited in several elastomeric materials, appears when successive loading and unloading cycles are applied on the rubber. Figure 17 gives a representation of the Mullins effect where 3 successive loading and unloading cycles have been applied.

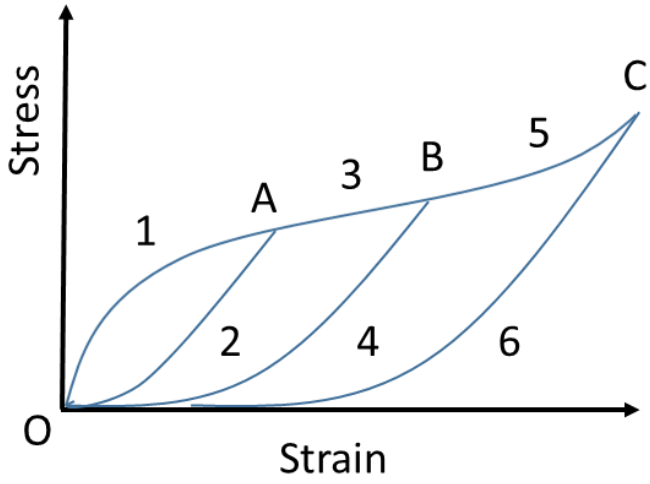

Figure 17: Qualitative representation of the Mullins effect

For example, a first loading is applied on an elastomeric material, which follows the **curve 1** from its initial sate (point **O)** up to a first stress (point **A)**. Then, the unloading of the materials follows the **curve 2** from the previous stress (point **A**) to the relaxed state (point **O**). The second loading follows the previous unloading path (**curve 2**), from point **O** to point **A,** and the path from point **A** to point **B** (**curve 3**). The related unloading path follows the **curve 4**, from point **B** to **O**. The third loading follows the **curve 4**, from point **O** to **B** and the **curve 5**, from **B** to **C.** The last unloading path follows the **curve 6** from point **C** to **O**.

In conclusion, the stress–strain curve of a specific loading depends on the maximum loading previously encountered. The Mullins effect is also called irreversible stress softening

Even if the Mullins effect is an important feature concerning the rubber behaviour, considering the maximum dynamic amplitude specified in part I.A.3, the area of the hysteresis should be negligible due to the low dynamic amplitude (unlike the static one) applied on the RME and then, the filled rubber (<1mm). Then the material law of the rubber could be linearize at the working point.

d) Consistency between linear elastic and hyperelastic laws

In this thesis, the response of a mounting system modelled using a linear elastic behaviour law will be compared to the one based on the Yeoh hyperelastic laws. To do this, it is necessary to establish a relation between the coefficient C_{10} introduced in the Yeoh model and the Young modulus involved in a classical linear elastic law. A possible way to establish such a relation is to obtain the partial derivative of the strain density function presented in equation 35 on a side and the one associated with a Hook law.

At first, some elements of the continuum mechanics are presented [53] to acknowledge the relations between material laws and between related coefficients. When a structure or material is loaded, a transformation ($\mathscr{F}$) occurs from an initial state (relaxed) to a deformed state (final). The initial state is supposed to be related to a first coordinate system (X1, X2, X3) and the deformed state to a second one (x1, x2, x3). In this part, the type of transformation, that is studied here, is a linear bijective homogenous morphism. This morphism possess the commutative, associative and distributive properties. Therefore, in this part, the influence of the time will not be considered. To establish a relation between the constitutive law coefficients, it is not necessary to consider the time, even for dynamic problematics, because of the previous properties. Moreover, the dynamic transformation can be decomposed in several homogenous transformations (for each time step). Such transformation may be illustrated as shown in Figure 18.

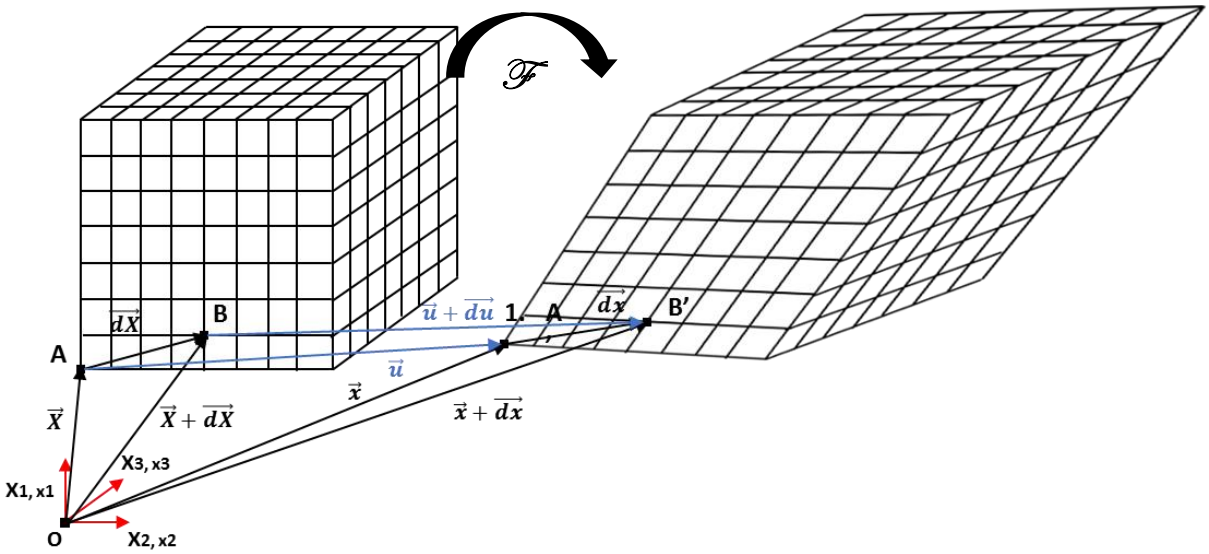

Figure 18: Un-deformed (relaxed) and deformed structure

Inside a material, a constitutive particle is characterize by its position relative to the current coordinate system origin. Therefore, it is possible to express the position of any particles (points) of the solid, depending on the coordinate system, for example point A, as follows:

$$\vec{X} = \begin{bmatrix} A1 \\ A2 \\ A3 \end{bmatrix}_{(X1,X2,X3)} \qquad 38$$

And

$$\vec{x} = \begin{bmatrix} A'1 \\ A'2 \\ A'3 \end{bmatrix}_{(x1,x2,x3)} \qquad 39$$

Let us then introduce the vectors $\overrightarrow{dX}$ and $\overrightarrow{dx}$, where $\overrightarrow{dx}$ refers to the vector $\overrightarrow{AB}$, and $\overrightarrow{dX}$ to the vector $\overrightarrow{A'B'}$:

$$\overrightarrow{dX} = \begin{bmatrix} B1 - A1 \\ B2 - A2 \\ B3 - A3 \end{bmatrix} \quad 40$$

$$\overrightarrow{dx} = \begin{bmatrix} B'1 - A'1 \\ B'2 - A'2 \\ B'3 - A'3 \end{bmatrix} \quad 41$$

To formulate mathematically the material deformation, a relation between each un-deformed geometrical element (point, segment, and polyhedron) with their related deformed element is needed. Vector $\overrightarrow{dX}$ is thus transformed to $\overrightarrow{dx}$ and the so-called transformation tensor $\mathbf{F}$ is introduced. The relation between initial state (reference configuration) and local state (current configuration) can be written as follows:

$$\overrightarrow{dx} = \overline{\overline{grad}}\ \mathbf{F} \,.\, \overrightarrow{dX} \quad 42$$

The tensor $\bar{\bar{F}}$ is then introduced as:

$$\bar{\bar{F}} = \overline{\overline{grad}}\ \mathbf{F} \quad 43$$

As a consequence, $\overrightarrow{dx}$ and $\overrightarrow{dX}$ are related as follows:

$$\overrightarrow{dx} = \bar{\bar{F}} \,.\, \overrightarrow{dX} \quad 44$$

The strain tensor ($\bar{\bar{F}}$) which links the descriptions of 3D solids may be expressed as follows:

$$\bar{\bar{F}} = \begin{bmatrix} F_{11} & F_{12} & F_{13} \\ F_{21} & F_{22} & F_{23} \\ F_{31} & F_{32} & F_{33} \end{bmatrix} = \begin{bmatrix} \frac{\partial x_1}{\partial X_1} & \frac{\partial x_1}{\partial X_2} & \frac{\partial x_1}{\partial X_3} \\ \frac{\partial x_2}{\partial X_1} & \frac{\partial x_2}{\partial X_2} & \frac{\partial x_2}{\partial X_3} \\ \frac{\partial x_3}{\partial X_1} & \frac{\partial x_3}{\partial X_2} & \frac{\partial x_3}{\partial X_3} \end{bmatrix} \quad 45$$

A scalar number J, inverse of the determinant of this tensor, is introduced for further use:

$$J = \frac{1}{\det \bar{\bar{F}}} \quad 46$$

To describe the mechanical behavior of materials, it exists two methods of cinematic description. The first one, the Eulerian description, focus on the description of the movement of materials particles trough a small area, defined, according to a local coordinate system (current configuration), of the studied material during a specified time. The second one, the Lagrangian, focus on the description of the movement of those particles during time according to the initial coordinate system (reference configuration). In consequence, all the vectors an scalars must be expressed with respect to $\vec{X}$.

The Lagrangian description, method used in solids mechanics, is sufficient to described the discussed features here. The transformation ($\mathscr{F}$) can be decomposed in two superimposable transformations, a rigid-body motion (translation and rotation) and a deformation. In Figure 18, the translation vector of the motion is denoted by $\vec{u}$. Therefore $\vec{x}$ can be expressed as follows:

$$\vec{x} = \vec{X} + \vec{u} \tag{47}$$

Then, it is possible to write:

$$\overrightarrow{dx} = \overrightarrow{dX} + \overrightarrow{du} \tag{48}$$

And, using equation 38:

$$\bar{\bar{F}} = \overline{\overline{grad}}\ \vec{X} + \overline{\overline{grad}}\ \vec{u} \tag{49}$$

The strain tensor can then be expressed as follows:

$$\bar{\bar{F}} = \bar{\bar{I}} + \bar{\bar{h}} \tag{50}$$

where $\bar{\bar{h}}$ is the gradient of the displacement vector $\vec{u}$.

In order to evaluate the strain, the square of $\overrightarrow{dx}$ vector magnitude is set as:

$$\left\|\overrightarrow{dx}\right\|^2 = \overrightarrow{dx}.\overrightarrow{dx} \tag{51}$$

Substituting the vector $\overrightarrow{dx}$ for $\overrightarrow{dX}$ and using equation 42, the previous equation becomes:

$$\left\|\overrightarrow{dx}\right\|^2 = \overrightarrow{dX}\ \bar{\bar{F}}^T.\bar{\bar{F}}\ \overrightarrow{dX} \tag{52}$$

The so-called right Cauchy-Green tensor is then introduced:

$$\bar{\bar{C}} = \bar{\bar{F}}^T.\bar{\bar{F}} \tag{53}$$

which matrix expression writes:

$$\bar{\bar{C}} = \begin{bmatrix} F_{11} \times F_{11} & F_{12} \times F_{12} & F_{13} \times F_{13} \\ F_{21} \times F_{21} & F_{22} \times F_{22} & F_{23} \times F_{23} \\ F_{31} \times F_{31} & F_{32} \times F_{32} & F_{33} \times F_{33} \end{bmatrix} \tag{54}$$

According to equation 48, the right Cauchy-Green tensor $\bar{\bar{C}}$ may be decomposed as:

$$\bar{\bar{C}} = (\bar{\bar{I}} + \bar{\bar{h}})^T.(\bar{\bar{I}} + \bar{\bar{h}}) \tag{55}$$

Which may also be written as:

$$\bar{\bar{C}} = \bar{\bar{I}} + \bar{\bar{h}} + \bar{\bar{h}}^T + \bar{\bar{h}}^T\bar{\bar{h}} \tag{56}$$

If the current configuration is considered, it is necessary to evaluate all the strain components with respect to the local coordinate system. The square of vector $\overrightarrow{dX}$ magnitude may be written as:

$$\left\|\overrightarrow{dX}\right\|^2 = \overrightarrow{dx}\,\bar{\bar{B}}^{-1}\overrightarrow{dx} \qquad 57$$

The so-called left Cauchy-Green tensor may thus be introduced:

$$\bar{\bar{B}} = \bar{\bar{F}}.\bar{\bar{F}}^T \qquad 58$$

This tensor $\bar{\bar{B}}$ can be decomposed as the tensor $\bar{\bar{C}}$, leading to:

$$\bar{\bar{B}} = (\bar{\bar{I}} + \bar{\bar{h}}).(\bar{\bar{I}} + \bar{\bar{h}})^T \qquad 59$$

Or:

$$\bar{\bar{B}} = \bar{\bar{I}} + \bar{\bar{h}} + \bar{\bar{h}}^T + \bar{\bar{h}}\bar{\bar{h}}^T \qquad 60$$

The use of the two previous tensors depends on the considered reference coordinate system (initial or final). It is worth noting that the invariants of both tensors $\bar{\bar{B}}$ and $\bar{\bar{C}}$ are the same.

The resulting strain can be calculated from expressions 50 and 55:

$$\left\|\overrightarrow{dx}\right\|^2 - \left\|\overrightarrow{dX}\right\|^2 = \overrightarrow{dX}\,\bar{\bar{C}}\,\overrightarrow{dX} - \overrightarrow{dX}\,\bar{\bar{I}}\,\overrightarrow{dX} \qquad 61$$

At this point, the so-called Green-Lagrange strain tensor is introduced:

$$\bar{\bar{E}} = \frac{1}{2}(\bar{\bar{C}} - \bar{\bar{I}}) \qquad 62$$

Tensor $\bar{\bar{E}}$ may be expressed in term of the displacement gradient $\bar{\bar{h}}$:

$$\bar{\bar{E}} = \frac{1}{2}(\bar{\bar{h}} + \bar{\bar{h}}^T + \bar{\bar{h}}\bar{\bar{h}}^T) \qquad 63$$

It is worth noting that this tensor is not linear due to the second order term $\bar{\bar{h}}\bar{\bar{h}}^T$.

The matrix form of the tensor $\bar{\bar{E}}$ can formulated as follows:

$$\bar{\bar{E}} = \begin{bmatrix} \varepsilon_{11} & \varepsilon_{12} & \varepsilon_{13} \\ \varepsilon_{21} & \varepsilon_{22} & \varepsilon_{23} \\ \varepsilon_{31} & \varepsilon_{32} & \varepsilon_{33} \end{bmatrix} \qquad 64$$

For isotropic material, the physical properties of a material are the same in all directions, leading to the symmetry of the tensor $\bar{\bar{E}}$ ($\varepsilon_{12} = \varepsilon_{21}$; $\varepsilon_{23} = \varepsilon_{32}$; $\varepsilon_{13} = \varepsilon_{31}$). Therefore, if the studied elastomeric material is considered as isotropic, the related strain tensor $\bar{\bar{E}}$ is symmetrical.

It is then possible to find a coordinate system in which the Green-Lagrange strain tensor is diagonal. This leads to an easiest calculation of the invariants and simplifies the solution of the mechanical problem.

$$\bar{\bar{E}} = \begin{bmatrix} \varepsilon_I & 0 & 0 \\ 0 & \varepsilon_{II} & 0 \\ 0 & 0 & \varepsilon_{III} \end{bmatrix} \qquad 65$$

Where (ε_I; ε_{II}; ε_{III}) are the principal strains.

The so-called Cauchy tensor $\bar{\bar{\Sigma}}$, which express the stress state in the current configuration, is also symmetric and may be written as:

$$\bar{\bar{\Sigma}} = \begin{bmatrix} \sigma_{11} & \sigma_{12} & \sigma_{13} \\ \sigma_{12} & \sigma_{22} & \sigma_{23} \\ \sigma_{13} & \sigma_{23} & \sigma_{33} \end{bmatrix} \quad 66$$

As for the Green-Lagrange tensor, this tensor can be diagonalized as:

$$\bar{\bar{\Sigma}} = \begin{bmatrix} \sigma_I & 0 & 0 \\ 0 & \sigma_{II} & 0 \\ 0 & 0 & \sigma_{III} \end{bmatrix} \quad 67$$

When it is necessary to work in the reference configuration (initial coordinate system), the Cauchy tensor is no longer adapted so the first Piola-Kirchhoff tensor is introduced. This tensor relates the forces in the current configuration (local) to areas in the reference configuration (initial). It is linked to the Cauchy tensor as follows:

$$\bar{\bar{P}} = J\bar{\bar{\Sigma}}\bar{\bar{F}}^{-T} \quad 68$$

However, the first Piola-Kirchhoff relates elements that are not in the same configuration and is nearly never symmetrical. To solve this problem, the second Piola-Kirchhoff tensor is introduced. It relates the forces from the initial configuration (initial coordinate system) to the final configuration (final coordinate system) and may be expressed as follows

$$\bar{\bar{S}} = J\bar{\bar{F}}^{-1}\bar{\bar{\Sigma}}\bar{\bar{F}}^{-T} \quad 69$$

To solve complex mechanical problem, a valuable method is the energetic approach. This scalar approach works in all configurations and does not need the establishment of vectors and coordinate system. During a transformation endured by a material (elastic or hyperelastic), a potential elastic energy (W) is stored in the material. This energy may be calculated from the Green-Lagrange strain tensor and Cauchy stress tensor as follows:

$$W = \frac{1}{2}\,\bar{\bar{\Sigma}} : \bar{\bar{E}} \quad 70$$

After this brief presentation of mechanical features, it is possible to focus on the hyperelastic features in terms of stress and strain tensor. A first hyperelastic model with a phenomenological approach, called Saint-Venant-Kirchhoff model, introduces a relation between the Hook law and the second Piola-Kirchhoff tensor [53]. Then, this tensor can be expressed as:

$$\bar{\bar{S}} = \lambda\, tr\left(\bar{\bar{E}}\right)\bar{\bar{I}} + 2\mu\bar{\bar{E}} \quad 71$$

where λ and μ are the Lamé coefficients, $\bar{\bar{I}}$ the identity tensor and $\bar{\bar{E}}$ the Green-Lagrange strain tensor.

Considering an incompressible material, $tr\left(\bar{\bar{E}}\right)$ is equal to 0. Using equation 60, equation 68 becomes:

$$\bar{\bar{\Sigma}} = \mu\,(\bar{\bar{C}} - \bar{\bar{I}}) \qquad 72$$

Furthermore, the second Piola-Kirchhoff tensor $\bar{\bar{S}}$ is energy conjugated to the Green-Lagrange tensor $\bar{\bar{E}}$. It may therefore be obtained from the potential elastic energy *W* as:

$$\bar{\bar{S}} = \frac{\partial W}{\partial \bar{\bar{E}}} \qquad 73$$

Or, using equation 60, as:

$$\bar{\bar{S}} = 2\frac{\partial W}{\partial \bar{\bar{C}}} \qquad 74$$

Using the Invariants of the tensor $\bar{\bar{C}}$ (I_I, I_{II}, I_{III}), Equation becomes:

$$\bar{\bar{S}} = 2\left(\frac{\partial W}{\partial I_I}\frac{\partial I_I}{\partial \bar{\bar{C}}} + \frac{\partial W}{\partial I_{II}}\frac{\partial I_{II}}{\partial \bar{\bar{C}}} + \frac{\partial W}{\partial I_{III}}\frac{\partial I_{III}}{\partial \bar{\bar{C}}}\right) \qquad 75$$

with:

$$\frac{\partial I_I}{\partial \bar{\bar{C}}} = \bar{\bar{I}} \qquad 76$$

and

$$\frac{\partial I_{II}}{\partial \bar{\bar{C}}} = I_I\bar{\bar{I}} - \bar{\bar{C}} \qquad 77$$

and

$$\frac{\partial I_{III}}{\partial \bar{\bar{C}}} = det(\bar{\bar{C}})\bar{\bar{C}}^{-1} \qquad 78$$

thus,

$$\bar{\bar{S}} = 2\frac{\partial W}{\partial I_I}\bar{\bar{I}} + \frac{\partial W}{\partial I_{II}}\left(I_I\bar{\bar{I}} - \bar{\bar{C}}\right) + \frac{\partial W}{\partial I_{III}}\left(det(\bar{\bar{C}})\bar{\bar{C}}^{-1}\right) \qquad 79$$

When the material incompressible, one has to note that:

$$det\left(\bar{\bar{C}}\right) = I_{III} = J = 1 \qquad 80$$

Furthermore, in a case of compression, the second Piola-Kirchhoff tensor can be expressed only by the first and second invariants:

$$\bar{\bar{S}} = 2\left(\frac{\partial W}{\partial I_I}\frac{\partial I_I}{\partial \bar{\bar{C}}} + \frac{\partial W}{\partial I_{II}}\frac{\partial I_{II}}{\partial \bar{\bar{C}}}\right) \qquad 81$$

Hence, equation 76 finally becomes:

$$\bar{\bar{S}} = 2\left(\frac{\partial W}{\partial I_I}\,\bar{\bar{I}} + \frac{\partial W}{\partial I_{II}}\left(I_I\bar{\bar{I}} - \bar{\bar{C}}\right)\right) \quad 82$$

Then, to express the Cauchy tensor ($\bar{\bar{\Sigma}}$) using the last equation and equation 67:

$$\bar{\bar{\Sigma}} = \frac{1}{J}\,\bar{\bar{F}}\bar{\bar{S}}\bar{\bar{F}}^T \quad 83$$

Combining equation 80 and equation 79 leads to:

$$\bar{\bar{\Sigma}} = 2\left(\frac{\partial W}{\partial I_I}\,\bar{\bar{F}}\bar{\bar{F}}^T + \frac{\partial W}{\partial I_{II}}\left(I_I\bar{\bar{F}}\bar{\bar{F}}^T - \bar{\bar{F}}\bar{\bar{C}}\bar{\bar{F}}^T\right)\right) \quad 84$$

And finally,

$$\bar{\bar{\Sigma}} = 2\left(\left(\frac{\partial W}{\partial I_I} + \frac{\partial W}{\partial I_{II}}\,I_I\right)\bar{\bar{B}} - \frac{\partial W}{\partial I_{II}}\,\bar{\bar{B}}\bar{\bar{B}}\right) \quad 85$$

However, it is necessary, to enforce the incompressibility constraints. Therefore, equation 85 becomes:

$$\bar{\bar{\Sigma}} = 2\left(\left(\frac{\partial W}{\partial I_I} + \frac{\partial W}{\partial I_{II}}\,I_I\right)\bar{\bar{B}} - \frac{\partial W}{\partial I_{II}}\,\bar{\bar{B}}\bar{\bar{B}}\right) - p\bar{\bar{I}} \quad 86$$

where p is an undetermined pressure.

However, the strain density function linked to the Yeoh model dependent only on the first invariant of the Cauchy-Green tensor. In this case, equation 86 becomes:

$$\bar{\bar{\Sigma}} = 2\left(\frac{\partial W}{\partial I_I}\right)\bar{\bar{B}} - p\bar{\bar{I}} \quad 87$$

It is possible to notice that, using equation 35:

$$\frac{\partial W}{\partial I_I} = C_{10} \quad 88$$

In consequence, for the consistency between both models, the following relation needs to be respected:

$$\mu = 2\,C_{10} \quad 89$$

The relation between the second Lamé coefficient and the Young modulus is given by the following formula [53]:

$$\mu = \frac{E}{2(1+\upsilon)} \quad 90$$

In conclusion, when the stress is uniaxial (compression) and the considered material isotropic and nearly incompressible ($\nu \approx 0{,}5$), the first Yeoh coefficient (C_{10}) of the hyperelastic law is related to the Young modulus of a linear elastic law (E) by the following expression:

$$C_{10} = \frac{E}{6} \qquad 91$$

C. RME CHARACTERIZATION TYPES

In the state of art, several aspects of the damping systems, as resilient mounting elements, and their related application fields were discussed. However, methods to characterize the RME were not presented. Before introducing the practical features of the thesis, related to the experiment that will be conducted, it is judicious to study and investigate methods to characterize a resilient mounting element (RME). Indeed, the characterization objective is to provide a potential prediction model the RME behaviour depending on the environmental parameters. As it was previously discussed in the previous part (I.B.4), those environmental parameters can be the environment temperature, excitation frequency or stress amplitude for instance, when studying frequency related problems. However, the characterization focus mainly on the elastomer behaviour prediction in function of external excitation frequency. The most appropriate element, that characterize the RME in function of the frequency, especially in the low frequencies, is the dynamic transfer stiffness [42]. In section I.B.3.b, the dynamic transfer stiffness (DTS) was introduced and considered as a complex number. Therefore, it can be decomposed in a real part and in an imaginary part integrating a viscoelastic aspect.

In this section, methods to estimate and calculate the DTS, leading to the creation of predictive model, will be discussed. In fact, the DTS can be obtained by the three evoked approaches: the experimental, numerical and analytical ones. At first, the classical experimental methods, that was early developed, discussed and debated, will be presented. Then the analytical methods will be examined with the introduction of the simplest analytical models that use a rheological approach. Finally, the numerical methods, which came lately with the development of the finite element theory combined with the computing power, will be developed. At the end of this part, a small recapitulative section lists the different advantages and disadvantages of each methods.

1. Experimental characterization methods

Among the three presented characterization type, the most extensive, accurate and well-documented one is the DTS determination using an experimental approach. This type of characterization is also quite different from the two other methods. Indeed, this method does not use any modelling to determine the DTS. In fact, in this method, the necessary data to elaborate and calculate the DTS are obtained via the measured physical quantities. However, the DTS cannot be directly calculated from the measured physical quantities. As it was previously mentioned in section I.B.3.b, the dynamic transfer stiffness is a transfer function, ratio between an input signal and output signal. In fact, the experimental methods rely on acquisition of the DTS of a RME. Furthermore, the RME should be a representative sample of the studied resilient mounts.

To be able to calculate the DTS, several steps must respected. These steps depends on the experimental method. It exist two main experimental method. The first experimental method is the method using an impact testing as excitation. The second is the method using a controlled dynamic excitation. The choice of the method is generally related to the size of the tested element. Indeed, the first method is for relatively small and light structures [15] unlike the second method, which is for bigger and heavier structures [14] [41].

a) Method using impact testing

In this method, the input signal is an impact, therefore an input force, and the resulting output physical quantities, displacements [47]. The impact, or better known as Dirac impulse, by its nature, excites all the natural frequencies of the tested element or structure. Indeed, the Fourier transformation of the Dirac impulse is a constant function in the frequency domain. In consequence, this method is generally interesting and chosen to perform experimental normal mode analysis. In this case, the tested element or structure must be mechanically isolated to avoid any interaction with the environment (ground, walls, etc.). In practical, it is impossible to isolate completely the structure. Therefore, at best the structure is partially isolated. This partial isolation could be achieved, for example, when the structure is placed on springs [55] with very low stiffness or when the structure is suspended to strings [15].

Figure 19 shows a typical configuration of a normal mode analysis of a steel disk.

Figure 19: Suspended disk for its normal mode analysis

In fact, the output displacement can be measured at the desired spots in the wanted direction. To be able to calculate a proper DTS, the output displacement and input force should have the same temporal window. Therefore, the measurement of the output displacement should starts at the same time as the impact. Then, it is possible to acquire the DTS, using the FFT to transform the temporal signals into frequency spectra. Finally, the DTS could be expressed in the frequency domain.

b) Method using dynamic exciter

The other method is quite different from the previous method. In this method, the four-pole parameters theory is considered as verified. In fact, this method is the one presented in the ISO standard 10846 [42], and more especially in the ISO 10846-2, called the direct method. This method will be exhaustively analyzed in the section I.D.1. Unlike the previous method, the input used in this one is a dynamic excitation. This excitation can have several form, as it will be explained in section I.D.1.a. This excitation is performed by a dynamic exciter, which is controlled by the user via a DAQ.

Figure 20 shows a typical configuration of a direct DTS determination.

Figure 20: Compressed spring during its characterization

The excitation is generally a controlled displacement signal. Then, measuring the reaction force under the spring it is possible to calculate the DTS via the use of the FFT on the temporal signal to obtain frequency spectra of the displacement and force. Finally, the DTS could be expressed in the frequency domain.

The advantages and disadvantages will be presented in section I.C.4.

2. Analytical characterization methods

In the perspective of the DTS determination in function of the environmental parameters, especially for frequency related issues, in function of the excitation frequency, analytical models bring opportunities to create methods for this determination.

As it was previously evoked in section I.B.3.a by Ferry [47], it is possible to use rheological models to simulate the behaviour of viscoelastic material and, by extension, rubberlike material. Analytical models are mathematical models that describe a phenomenon related to a system, using a governing equation composed by constitutive and defining equations. These equations relate the external physical quantities that interact with the system such as the environmental physical quantities (temperature, pressure) to the response of the system, predicting its behaviour under certain circumstances. Therefore, for a determined set of environmental parameters, the response of the system is obtained by solving the governing equation of the system. The equation solving depends on the form of the established equation. The form of this equation is defined by its potential linearity, stationary condition, and determinism. Furthermore, the description of the environmental parameters evolution and the interaction between the system and its environment should be sufficiently accurate and exhaustive.

Therefore, the pertinence of an analytical model relies on the precision of the description and the complexity of the equation solving. Generally, if the precision increases, the complexity increases. In consequence, the constitution of an analytical model relies on a compromise between the precision of the description and the complexity of the model.

In mechanic, the analytical models relate the physical quantities of the system motion (acceleration, velocity, displacement and strain) to the constraints applied on the system via, for instance, the second law of Newton and material laws. In mechanic, the studied elements are defined in the 3D space, at the exception of few where a reduction in 2D or 1D is possible under certain circumstances. Due to the definition of these elements in the three dimensions, a governing equation should be expressed in the $\mathbb{R}^3$ vector space. Therefore, the governing equation should be expressed in the 3D, decomposed or not. If the vectorial governing equation is decomposed, six components are obtained, three for each translation and three for each rotation. In fact, analytical models are mostly used when considering a one degree of freedom system or six non-coupled degree of freedom system. The coupling often generates an escalation in terms of complexity.

To reduce the complexity of an equation, initial or boundary conditions can be used. Then they permit the solving of the equation, setting a value at a certain time for an initial condition and a value at a certain point of the model for a boundary condition.

Another possibility to reduce the complexity of the governing equation is concerning the environmental parameters. Although environmental physical quantities generally depend on each other (temperature, pressure) their effect on the structure could be decoupled and then, could be studied separately. In fact, the multiplication of environmental variables in the equation increases exponentially the complexity of the model. Therefore, to avoid the increase of the complexity, it is possible to decompose the governing equation and to express the equation at certain environmental parameter constants.

In consequence, the analytical models are limited to strict conditions, such as cases with constant environmental parameters, at the exception of one, to study the effect of this parameter on the system response.

Concerning the investigations about the use of analytical models to predict the behaviour of the RME by determining the DTS, the study of the damping material viscoelasticity is necessary. To study the viscoelasticity of a material, several mechanical phenomena, which emerge from viscoelastic behaviour examinations, such as the creep and relaxation, should be considered in the model description. Then, it is required to realize a prospection of the different analytical models that consider the creep and relaxation as fundamental feature to estimate the quality of the model.

This prospection about the different rheological models will then be limited to simple rheological models. Among all the rheological that could be handled easily, three will be exposed: the Maxwell model, the Kelvin-Voigt model and the Zenner model. The three models use only two elementary rheological models: a Hookean spring and a Newtonian dashpot. When subjected to an axial stress, both elements relate individually this axial stress and an associated strain.

Figure 21 represents a Hookean spring model.

Figure 21: Hookean spring model

The Hookean spring model relates the axial stress to the strain as follows:

$$\sigma_s = E_s \, \varepsilon_s \tag{92}$$

where, σ_s refers to the axial stress and expressed in Pa, ε_s, the resulting strain and E_s the Young modulus or elastic modulus associated with the model, expressed in Pa.

Figure 22, as for it, represents a Newtonian dashpot.

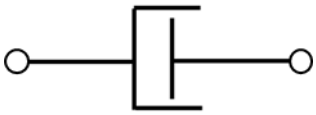

Figure 22: Newtonian dashpot model

The Newtonian dashpot relates the axial stress to the strain as follows:

$$\sigma_d = \eta_d \, \frac{d\varepsilon_d}{dt} \tag{93}$$

where, σ_d refers to the axial stress and expressed in Pa, ε_d, the resulting strain and η_d the dynamic viscosity associated with the model, expressed in Pa.s.

a) Maxwell model

At first, one of the two simplest rheological model to describe a viscoelastic material is the Maxwell model introduced in 1867 [56]. The Maxwell model is composed by a Hookean spring and a Newtonian dashpot associated in series.

Figure 23 exposed a schematic representation of Maxwell model.

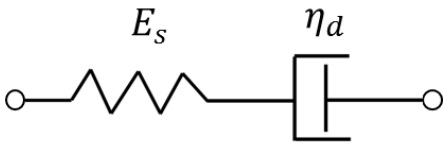

Figure 23: Maxwell rheological model

When two mechanical elements, which are associated in series, are subjected to an axial stress, the total stress is the same in the two elements and the total resulting strain is the sum of the strain in the respective elements. The total stress and strain can be expressed as follows:

$$\sigma_{tot} = \sigma_s = \sigma_d = \sigma \quad (94)$$

$$\varepsilon_{tot} = \varepsilon_s + \varepsilon_d \quad (95)$$

Therefore, considering the total strain time derivative, it is possible to obtain the following equation:

$$\dot{\varepsilon_{tot}} = \frac{\sigma}{\eta_d} + \frac{\dot{\sigma}}{E_s} \quad (96)$$

Multiplying each term of the previous equation by η_d, it gives:

$$\eta_d \dot{\varepsilon_{tot}} = \sigma + \frac{\eta_d}{E_s}\dot{\sigma} \quad (97)$$

The ratio between the dynamic viscosity and the elastic modulus is called the relaxation time t_r, previously introduced in section I.B.4.a.

In fact, this particular model is quite appropriate to model the stress relaxation of a viscoelastic material [56]. The stress relaxation of a viscoelastic material appears when the material is subjected to a constant strain. Moreover, the related stress is decreasing over time. Indeed, if a constant strain (ε_0) is considered in the Maxwell model, the previous equation becomes:

$$0 = \sigma + \frac{\eta_d}{E_s}\dot{\sigma} \qquad 98$$

Figure 24 displays a qualitative evolution of stress and strain of two types of viscoelastic material during a relaxation, a solid and a liquid. A constant strain (ε_0) is applied at t_1, that create a resulting stress that decrease through frequency. For a liquid, the stress converge to 0, but, for a solid, it converges to a residual stress (σ_∞).

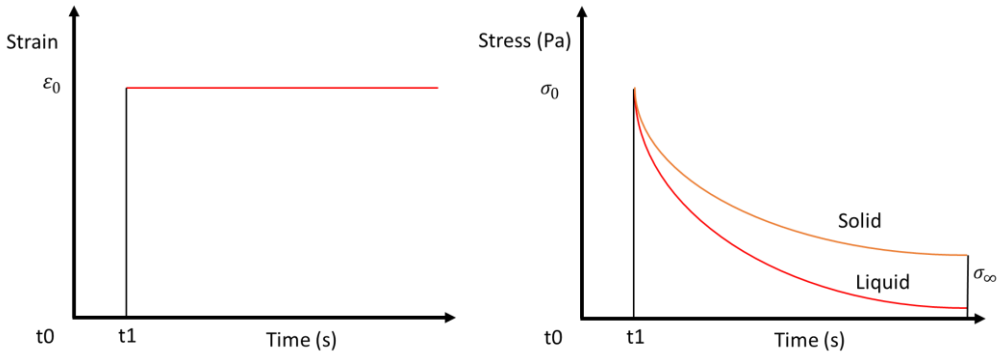

Figure 24: Qualitative representation of the strain and stress evolution through time during a relaxation

The resolution of the previous equation leads the establishment and the resolve of a homogenous first order linear differential equation. Therefore, the solution of this differential equation has the following form:

$$\sigma(t) = \sigma_0 \times \exp\left(-\frac{E_s}{\eta_d}t\right) \qquad 99$$

where, σ_0 is the stress at t_1.

As the final form of the relation between the stress and the strain in a decrescent exponential curve, the Maxwell represents appropriately the relaxation of a liquid viscoelastic material.

Furthermore, when a constant stress is considered in the Maxell model, the equation relating the stress and the strain becomes:

$$\dot{\varepsilon_{tot}} = \frac{\sigma}{\eta_d} \qquad 100$$

Integrating, the previous equation from t_0 to infinity, it is possible to express the strain in function of the stress:

$$\varepsilon_{tot} = \frac{\sigma}{\eta_d}\, t \qquad 101$$

Therefore, the evolution of the strain when a constant stress is applied, is a linear function that increases through time.

The creep of a solid viscoelastic material appears when this material is subjected to a constant stress. Then, the related strain in the material increases through time.

Figure 25 displays a qualitative evolution of stress and strain of a solid viscoelastic material during a creep. A constant stress (σ_0) is applied at t_1, that create a resulting strain that increase through frequency after an instaneous strain (ε_0).

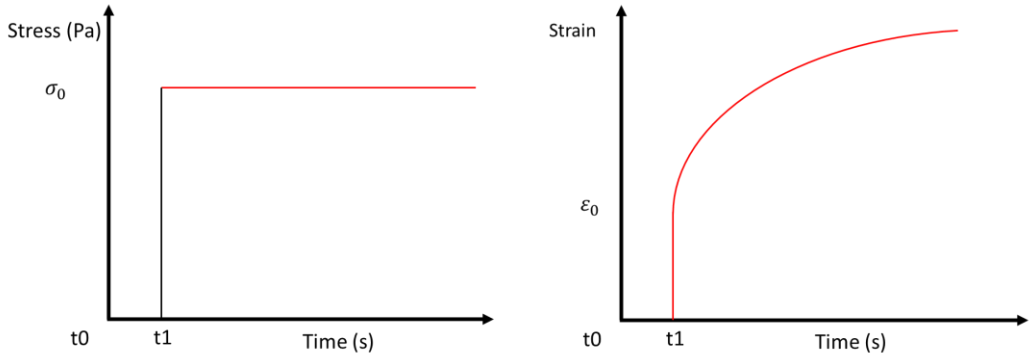

Figure 25: Qualitative representation of the strain and stress evolution through time during a creep

As it is presented in Figure 25, the evolution of the strain does not follow a linear function curve. Therefore, the Maxwell model seems to be not appropriate to model the creep of a viscoelastic solid material. Considering that, the Maxwell model is not capable to model correctly the creep of a solid viscoelastic material; it should be more adapted to model a viscoelastic fluid behaviour.

b) Kelvin-Voigt model

The other simplest rheological model is the Kelvin-Voigt model, which is named after a German scientist, Woldemar Voigt, and the well-know Lord Kelvin. The Kelvin-Voigt model is composed of a Hookean spring and a Newtonian dashpot associated in parallel [56].

Figure 26 exposes a schematic representation of Maxwell model.

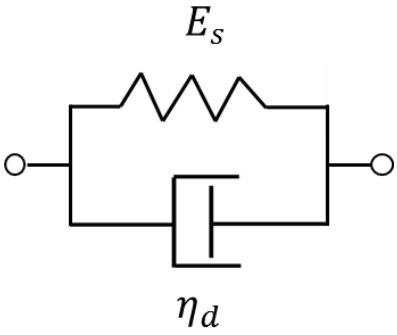

Figure 26: Kelvin-Voigt rheological model

When two mechanical elements, which are associated in parallel, are subjected to an axial stress, the total stress is the sum of the stress in the respective elements and the total resulting strain is the same strain in the two elements. The total stress and strain can be expressed as follows:

$$\varepsilon_{tot} = \varepsilon_s = \varepsilon_d = \varepsilon \quad (102)$$

$$\sigma_{tot} = \sigma_s + \sigma_d \quad (103)$$

Therefore, it is possible to relate the strain and the stress of the model, using the two previous equations, as follows:

$$\sigma_{tot} = E_s\,\varepsilon_s + \eta_d\dot{\varepsilon_d} \qquad 104$$

As with the Maxwell model, considering the relaxation of a viscoelastic material (constant deformation), it is possible to write:

$$\sigma_{tot} = E_s\,\varepsilon_s \qquad 105$$

In this case, the Kelvin-Voigt model imply that, during a relaxation, the stress should be linearly proportionate with the strain, which is not coherent with the relaxation curves displayed in Figure 24. Therefore, the Kelvin-Voigt is not adapted to model the relaxation of a viscoelastic solid behaviour.

Moreover, also as with the Maxwell model, considering the creep of a viscoelastic material (constant stress), it is possible to write:

$$\sigma_0 = E_s\,\varepsilon_s + \eta_d\dot{\varepsilon_d} \qquad 106$$

The resolution of this first order inhomogeneous linear differential equation, leads to the following expression relating the strain and the stress:

$$\varepsilon(t) = \frac{\sigma_0}{E_s}\ (1 - \exp\left(-\frac{E_s}{\eta_d}\ t\right)) \qquad 107$$

The previous equation gives a strain curve in function of the time similar to the strain curve displayed in Figure 25. Therefore, the Kelvin-Voigt model is appropriate to model the creep of a solid viscoelastic material. Furthermore, considering that the Kelvin-Voigt model is not capable to described properly the relaxation of a viscoelastic material, this model should be adapted to model only the behaviour of solid viscoelastic material.

c) Zener model

In order to have a model that permit to describe appropriately the relaxation and the creep of a viscoelastic material at the same time, another model can be use. However, this model is slightly more complex than the two previous models. This model, known as the Zener model or standard linear solid (SLS) model, integrates only the elementary rheological models, previously mentioned. However, they are associated in a manner that describes well the relaxation and creep [56]. This model can have two possible representations.

Figure 27 exposed the first schematic representation of the Zenner model.

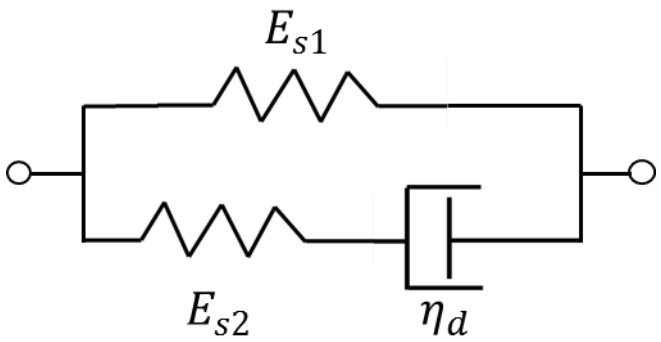

Figure 27: first representation of the Zener rheological model

At first, the association of a Hookean spring and Newtonian dashpot in the lower branch gives the followings resulting stress and resulting strain, as discussed in the Maxwell model:

$$\sigma_{int1} = \sigma_{s2} = \sigma_d \quad (108)$$

$$\varepsilon_{int1} = \varepsilon_{s2} + \varepsilon_d \quad (109)$$

Furthermore, associating the two branches of the model, it gives:

$$\varepsilon_{tot} = \varepsilon_{s1} = \varepsilon_{int1} = \varepsilon \quad (110)$$

$$\sigma_{tot} = \sigma_{s1} + \sigma_{int1} = \sigma \quad (111)$$

Therefore, considering the total strain time derivative, it is possible to obtain the following equation:

$$\dot{\varepsilon} = \frac{\frac{E_{s2}}{\eta_d}\left(\frac{\eta_d}{E_{s2}}\dot{\sigma} + \sigma - E_{s1}\varepsilon\right)}{E_{s1} + E_{s2}} \quad (112)$$

The previous can also be expressed with strain related parameters in a side of the equation and stress related parameters in the other side:

$$E_{s1}\varepsilon + \frac{\eta_d(E_{s1} + E_{s2})}{E_{s2}}\dot{\varepsilon} = \sigma + \frac{\eta_d}{E_{s2}}\dot{\sigma} \quad (113)$$

Considering a creep (constant stress σ_0) of a viscoelastic material, the previous equation gives:

$$E_{s1}\varepsilon + \frac{\eta_d(E_{s1} + E_{s2})}{E_{s2}}\dot{\varepsilon} = \sigma_0 \quad (114)$$

The resolution of this first order inhomogeneous linear differential equation, leads to the following expression relating the strain and the stress:

$$\varepsilon(t) = \frac{\sigma_0}{E_{s1}}\left(1 - \exp\left(-\frac{E_{s1}E_{s2}}{\eta_d(E_{s1} + E_{s2})}\,t\right)\right) + \varepsilon_0 \quad (115)$$

where ε_0 is the instantaneous deformation resulting of the stress and:

$$\varepsilon_0 = \frac{\sigma_0}{E_{s1}} \quad (116)$$

The associated curve of the time-dependent equation 116 seems to describe well the evolution of the strain of a solid viscoelastic material during a creep.

Considering a relaxation (constant strain ε_0 different from the previous ε_0) of a viscoelastic material, equation 113 becomes:

$$E_{s1}\varepsilon_0 = \sigma + \frac{\eta_d}{E_{s2}}\dot{\sigma} \quad (117)$$

The resolution of this first order inhomogeneous linear differential equation, leads to the following expression relating the strain and the stress:

$$\sigma(t) = E_{s1}\varepsilon_0\ \left(1 + \exp\left(-\frac{E_{s2}}{\eta_d}\,t\right)\right) \quad (118)$$

The associated curve of the previous time-dependent equation seems to describe well the evolution of the strain of a solid viscoelastic material during a relaxation.

According to the analysis of this sub-model of the Zener model, in terms of creep and relaxation, it appears that this sub-model could represent the behaviour of a solid viscoelastic material

Moreover, a second representation of the Zener model is possible.

Figure 28 exposed the second schematic representation of the Zenner model.

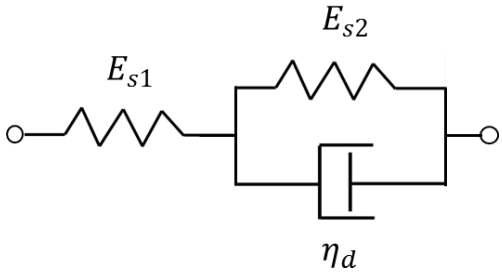

Figure 28: second representation of the Zener rheological model

At first, the association of a Hookean spring and Newtonian dashpot gives the followings resulting stress and resulting strain, as discussed in the Kelvin-Voigt model:

$$\varepsilon_{int2} = \varepsilon_{s2} = \varepsilon_d = \varepsilon \quad (119)$$

$$\sigma_{int2} = \sigma_{s2} + \sigma_d \quad (120)$$

Furthermore, associating the two branches, right and left, it gives:

$$\sigma_{tot} = \sigma_s = \sigma_d = \sigma \quad (121)$$

$$\varepsilon_{tot} = \varepsilon_s + \varepsilon_d \quad (122)$$

Therefore, considering the total strain time derivative, it is possible to obtain the following equation:

$$\frac{E_{s1} \times E_{s2}}{E_{s1} + E_{s2}} \varepsilon + \frac{E_{s1}\eta_d}{E_{s1} + E_{s2}} \dot{\varepsilon} = \sigma + \frac{\eta_d}{E_{s2} + E_{s1}} \dot{\sigma} \quad (123)$$

Considering a creep (constant stress σ_0) of a viscoelastic material, the previous equation gives:

$$\frac{E_{s1} \times E_{s2}}{E_{s1} + E_{s2}} \varepsilon + \frac{E_{s1}\eta_d}{E_{s1} + E_{s2}} \dot{\varepsilon} = \sigma_0 \quad (124)$$

The resolution of this first order inhomogeneous linear differential equation, leads to the following expression relating the strain and the stress:

$$\varepsilon(t) = \frac{\sigma_0(E_{s1} + E_{s2})}{E_{s1}E_{s2}} \left(1 - \exp\left(-\frac{E_{s1}}{\eta_d} t\right)\right) + \varepsilon_0 \quad (125)$$

where ε_0 is the instantaneous deformation resulting of the stress and:

$$\varepsilon_0 = \frac{\sigma_0(E_{s1} + E_{s2})}{E_{s1}E_{s2}} \quad (126)$$

The associated curve of the time-dependent equation 126 seems to describe well the evolution of the strain of a solid viscoelastic material during a creep, as with the first representation of the Zener model.

Considering a relaxation (constant strain $\varepsilon_0$different from the previous one) of a viscoelastic material, equation 123 becomes:

$$E_{s1}\varepsilon_0 = \sigma + \frac{\eta_d}{E_{s2}}\dot{\sigma} \qquad 127$$

The resolution of this first order inhomogeneous linear differential equation, leads to the following expression relating the strain and the stress:

$$\sigma(t) = E_{s1}\varepsilon_0 \ (1 + \exp\left(-\frac{E_{s2}}{\eta_d}\ t\right)) \qquad 128$$

The associated curve of the previous time-dependent equation seems to describe well the evolution of the strain of a solid viscoelastic material during a relaxation, as with the first representation of the model.

In conclusion, although the relative higher complexity of the SLS model could be more difficult to manage, it is capable to model appropriately the behaviour of a solid viscoelastic material in relaxation and creep.

3. Numerical characterization methods

The last characterization method that is possible use to determine the DTS of the RME is the numerical simulation. As the analytical one, this method is based on the creation of predictive models to evaluate the DTS in function of the frequency. In fact, the numerical methods share many common features with the analytical method. Indeed, constitutive, defining and governing equations are present in the numerical models. The initial and boundary conditions are also present in the model.

However, even though, the numerical characterization share the same objective and same components to create the predictive model, the method to resolve the governing equations using numerical methods are completely different. In fact, the numerical models use derivative equations to solve the problem. However, it is impossible to solve these derivative equations by hands. Therefore, computing system are used. Due to the fact that the computer are increasingly powerful, especially during the last twenty years, the numerical methods are the most studied and used for the characterization in frequency. It exists several types of numerical methods but most of them are based on the finite element theory even though some numerical methods could be based on the super element theory or other element formulations, such as finite volume. In fact, the finite element models constitute the main part of the numerical studies. However as for the analytical methods, external data are needed to set the models.

As it is not really interesting to study in depth the functioning of the numerical methods, it is more interesting to investigate on the previous numerical studies on the resilient mounting elements.

An interesting work concerning the characterization via the creation of a predictive model of a rubber isolator in high frequency (50 -5000 Hz), integrating a non-linear material law to model the rubber behaviour was effected by Kari L. [57]. The main objectives was the creation of a cylindrical isolators numerical model to determine the DTS, which integrated viscoelastic features and non-linear behaviour, to represent the most exactly possible the rubber behaviour.

In the previous work, the Yeoh hyperelastic material law was not used for the constitutive law of the rubber. Therefore, the proximity of this work from the work is not as satisfying as it would be.

However, another work, effected by Beijers and de Boer, [58] was using the constitutive model DTS determination proposed by Kari, integrating the Yeoh hyperelastic law as the constitutive rubber law. The DTS was acquires by performing a simulation similar as the experimental method using a dynamic exciter, in terms of followed procedure. Indeed, the excitation (displacement) was applied at the top of the rubber element along the vertical direction and the output parameter was the reaction force at the bottom of the rubber isolator, where it was clamped. It is worth noting that the work was also conduct in high frequency, from 150 Hz to 1000 Hz. In this example, it was shown that, considering the presented Yeoh coefficient values, rubber isolator has a rigid-body behaviour until 350Hz.

The last interesting point to be studied here is the work effected by Moro L. In fact his work is the nearest from the work presented in the thesis. His work, on the same RME as the on in the thesis was performed in high frequency. Therefore, several data from his work were used in this thesis such as the same Yeoh parameter

4. Particularities each methods

After the prospection on the important features of the three types of method presented, the particularities of each one could be exposed. For each one the advantages and disadvantages will be exposed.

- Experimental methods
    - **Advantages**

At first, the experimental methods offer the possibility to determine the DTS without the need of predictive models. The only calculation that is presented in the experimental characterization is the transformation of temporal signals into frequency spectra via the Fourier transformation to be able to obtain the DTS in the frequency domain. In fact, the experimental characterisation is the nearest to the reality because the only source of variability comes only on the evaluation of the representativeness of the tested element. Therefore, the experimental is considered as the most accurate characterisation and complete of the characterisation.

    - **Disadvantages**

However, the experimental one is potentially long, depending on the test length and costly due to the required material to perform the characterisation. The length of the experiment is generally high for the frequency characterisation of passive isolators. In general, it varies from one day to one week depending on the expected results. Furthermore, as it was mentioned previously, the representativeness of the tested element induce a disadvantage. Indeed, a potential non-linearity in the tested element could induce an unwanted variation of the results, leading to a loss in term of representativeness. Therefore, the characterised passive isolator are considered linear to be able to consider the results as representative of the other RME of the same type.

- Analytical methods
    - **Advantages**

As it was previously evoked, the analytical method characterizes the RME in frequency via the creation of predictive models. Those models are generally simple and easy to manage as discussed in section I.C.2. Furthermore, due to its form its prediction can be effected quickly. In fact, for an simple model, the analytical method is the fastest of the three. Depending on the expected results and model configuration, an estimation can be effected in just a few seconds.

- Linear
    - **Disadvantages**

However, the analytical method is limited to few simple cases and the accuracy of the estimation depends on the accuracy of the model. The non-linearity is well managed in those models. As it was previously discussed, the models require data, to, at least, set the model. The data could originate from the literature but in general, it originate from previous experimental results.

- Numerical methods

The numerical method could be considered as between the two other methods in terms of advantages and disadvantages. Indeed, the numerical methods are quicker than the experimental ones but slower than the analytical ones. On the contrary, in terms of precision, the numerical methods are less precise than the experimental ones, but more precise than the analytical ones. However, the precision of the model depends on the refinement of the model. More the model is refined, more the model is precise. Concerning the velocity, more the model is refined, slower the model is. The numerical methods require also external data to set the model.

To conclude, each type of method has advantages and disadvantages, especially the analytical and numerical methods. Indeed they require, at least, initial data to create the model or, for more complex modelling, an initial tuning of the model using experimental data as it was mentioned by Moro L. [40]. After, these initial steps, those models could model the resilient mounting element in various configurations. However, if an exclusively experimental method is chosen, each different RME working configurations needs to be experimentally investigated. It could lead to long experimental campaign with high costs. The possibility to use transverse methods such as the one developed by Moro L. [40]., integrating an experimental part and a numerical part for example, gives possibilities to compensate the disadvantages of a method by the advantage of another.

D. RULES AND PRACTICAL ASPECTS

In this section, the practical aspects of the PhD work are discussed. The standard specifications, regarding both DMA and full scale experimental tests, are presented and discussed. At first, the principle guideline (ISO 10846-2) recommendations, concerning the experimental determination of T200 RME dynamic transfer stiffness, are presented and reviewed. Then, the ISO 6721 standard recommendations for DMA tests are introduced and specific implications on damping rubber material characterization highlighted. Finally, a quick presentation of the finite element software used in this thesis, and the related theorical features, are introduced.

1. ISO 10846 Standard for full scale RME characterization

As it was previously introduced, the determination of the dynamic transfer stiffness is the key point of the studies on resilient mounting elements. The International Society Organization (ISO) provides guidelines to perform measurements of the dynamic transfer properties of resilient mounting elements under static preload. Such rules provide help for the measurements of a preloaded RME dynamic transfer stiffness (DTS) whether in low frequency range (1-80Hz) or in high frequency range (> 50 Hz).

The ISO 10846 Standard: “Acoustic and vibration – laboratory measurements of vibro-acoustic transfer properties of resilient elements” is divided in three main parts:

- ISO 10846-1: Global presentation and frame
- ISO 10846-2: Resilient mounting element dynamic transfer stiffness determination using the so-called direct method
- ISO 10846-3: Resilient mounting element dynamic transfer stiffness determination using the so-called indirect method

For experimental characterizations in low frequency range, it is specified to follow the recommendations of ISO 10846-2 Standard which is based on the so-called direct method.

a) ISO 10846-2: Direct method

This method prescribes an experimental procedure to measure the dynamic transfer stiffness of a resilient mounting element (RME) under a certain preload for a normal and transverses directions depending on the geometry of the element. In order to perform the characterization, it specifies a typical test rig configuration which should fulfil structural requirements, from both dynamic and static pints of view.

Figure 29 presents the configuration for an axial unidirectional excitation.

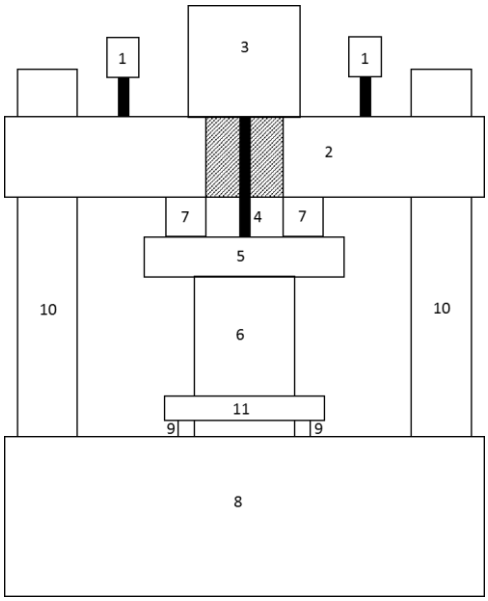

Figure 29: Test rig configuration for a normal/vertical excitation

This test rig is composed by several parts which perform specific tasks. The static preload is created by pistons (1) which exert a force on a mobile traverse (2) guided by pillars (10). This mobile traverse transmits the static load on the tested element (6) through soft isolators (7) which their main function is to decoupled the excitation mass from the test rig structure. The dynamic actuator (3) generates a dynamic excitation which is applied on the tested element by the exciting mass (5). A stinger (4) which is linked with the mobile traverse by a sliding pivot, achieves the connection between the exciting mass and the actuator. The distributing plate (11) ensures a good measurements of the resulting transmitted force to the load cells (9) located below the plate. All this elements are placed on the rigid foundation of the test rig (8).

According to the standard, the dynamic transfer stiffness is defined as the ratio between the dynamic force vector on the blocked side of the element, here measured by the loads cells, and the displacement vector of the excited side, here measured by accelerometers and by a displacement transducer. For the determination of the RME matrix of complex DTS, the excitation should be applied along only one direction and the post treated force measured along one direction. In a case of a uniaxial excitation, the vertical dynamic transfer stiffness can be expressed as follows:

$$K_{i1j1}{}^{*}(f) = \frac{F_{j1}{}^{*}(f)}{u_{i1}{}^{*}(f)} \qquad 129$$

In the experimental vibration analysis, it is more common to measure accelerations instead of displacements. In this case, if the displacement sensor is replaced by an accelerometer, when the displacement is supposed sinusoidal the previous equation becomes:

$$K_{i1j1}{}^{*}(f) = (-2\pi f)^2 \times \frac{F_{j1}{}^{*}(f)}{a_{i1}{}^{*}(f)} = (-2\pi f)^2 \times T_{i1j1}{}^{*}(f) \qquad 130$$

Furthermore, a particular attention is paid on critical components (such as mobile traverse or exciting mass) of the test rig and measurements system to ensure a good quality of the results. For example, during the measurements, the modal behaviour of such components may induce unwanted biases in the results.

The distributing plate, located just above the loads cells, is necessary to spread the vibrations uniformly on the load cells but it is crucial that the own characteristics of the plate does not induce unwanted deformation modes, which could disturb the measurements. The exciting mass serves to ensure a uniform and unidirectional vibration excitation on the tested element. As for the distributing plate, its design must ensure that the dynamic behaviour of the mass through frequency will not disturb the measurements.

Furthermore, accelerometers, force transducers, and displacement sensors are the main components of the sensors list. Accelerometers are needed in order to measure the level of vibrations at significant points of the test rig. Force transducers are required to measure the output force above the tested element. For the determination of the vertical DTS, the respective vertical components of the force transducers and vertical component of the displacement sensor or accelerometers are used.

As previously presented, the dynamic transfer stiffness is a complex number that may be described by its magnitude and its phase. Therefore, the sensors' sensibility must be chosen so that the physical quantity variation is measured with sufficient accuracy both in magnitude and phase.

According to the standard, the dynamic excitation system and its related components is considered as a critical part of the test rig. In the standard, a dynamic actuator and a sting rod compose the dynamic excitation system with the exciting mass. During the constitution of the dynamic excitation system, potential configurations leading to potential measurement disturbance should be avoided. Indeed, the dynamic behaviour of the rod could disturb the measurements if one or more of its natural frequencies are in the frequency range of the experiments. Thus, this rod should be sufficiently rigid to avoid a low natural frequency. The actuator, as for it, may be a hydrodynamic, pneumatic, or electromagnetic shaker. In fact, the recommended type of actuator depends on the operated frequency bandwidth related to the test rig. Thus, due to the multiple possibilities when choosing or conceiving the actuator, the proper mechanic excitation creation is left at user's discretion but should sustain the excitation management requirements.

The rule does not provide particular advices about the signal management system but, as for a global experimental perspective, the system should ensure controllable and measurable signal generation and analysis. The only recommendation of the standard concerns the type of input signal which should be applied. It specifies four types of signal that need to be generated when measuring the RME vibrating response:

- Discretely stepped sinusoidal signal
- Sine sweep
- Periodically swept sine signal
- A bandwidth-limited noise signal, generally white noise

The discretely stepped sinusoidal signal is a sine wave signal with a fixed frequency for each determined stepped time interval in the all test duration. The frequency generally increases gradually during the experiment. The sine sweep signal is similar to the stepped sine signal. This signal is a sine wave with a continuous increase of the frequency during the experiment.

The sine signal can also be periodically swept. At first, a sine wave at one frequency is generated during a determined duration. After this duration, the frequency of the sine wave varies leading to a sine sweep. This signal is, in consequence, similar to the sine sweep. The white noise signal is a random signal with a constant power spectral density in the frequency domain.

The use of the fast Fourier transformation to estimate the DTS in the frequency domain from data acquired in the time domain, several conditions should be respected concerning the form of the data to be able to have a precise transfer function. In fact, to calculate the FFT from the temporal signals, it is required to have a sufficiently long temporal window. Due to the potential variability of the temporal signals through the experiment time, the calculated FFT are different from a temporal window from another. Then, it is necessary to average the different FFT to obtain the most representative of the RME. The averaging is performed between the FFT of the current temporal window and the previous one calculated. Hence, when performing the experiment, the source signal should be sufficiently long to lead to a good averaging of the transfer function. An averaging could be considered good if the variation of magnitude level amplitude is less than 0.1 dB when the averaging time is doubled. In practical, the signal length depends on the studied RME and the test rig configuration. Then, the user should manage it, depending on its experience.

The RME could possess some geometrical symmetry which leads to simplify the response matrix calculation. If the RME is axis-symmetrical then the following simplification is possible for an excitation along this axis as displayed in Figure 29:

$$K_{i1j2}(f) = K_{i2j1}(f) = 0 \quad (131)$$

$$K_{i1j3}(f) = K_{i2j3}(f) = 0 \quad (132)$$

$$K_{i3j1}(f) = K_{i3j2}(f) = 0 \quad (133)$$

$$K_{i3j4}(f) = K_{i3j5}(f) = 0 \quad (134)$$

$$K_{i4j3}(f) = K_{i5j3}(f) = 0 \quad (135)$$

$$K_{i6j1}(f) = K_{i6j2}(f) = 0 \quad (136)$$

$$K_{i1j1}(f) = K_{i2j2}(f) \quad (137)$$

$$K_{i4j4}(f) = K_{i5j5}(f) \quad (138)$$

$$K_{i4j2}(f) = K_{i5j1}(f) \quad (139)$$

$$K_{i2j4}(f) = K_{i1j5}(f) \quad (140)$$

This leads the following expression of the dynamic transfer stiffness matrix:

$$\begin{pmatrix} F_{j1}(f) \\ F_{j2}(f) \\ F_{j3}(f) \\ M_{j4}(f) \\ M_{j5}(f) \\ M_{j6}(f) \end{pmatrix} = \begin{bmatrix} K_{i1j1}(f) & 0 & 0 & 0 & K_{i4j2}(f) & 0 \\ 0 & K_{i1j1}(f) & 0 & K_{i4j2}(f) & 0 & 0 \\ 0 & 0 & K_{i3j1}(f) & 0 & 0 & 0 \\ 0 & K_{i2j4}(f) & 0 & K_{i4j4}(f) & 0 & 0 \\ K_{i2j4}(f) & 0 & 0 & 0 & K_{i4j4}(f) & 0 \\ 0 & 0 & 0 & 0 & 0 & K_{i6j6}(f) \end{bmatrix} \begin{pmatrix} u_{i1}(f) \\ u_{i2}(f) \\ u_{i3}(f) \\ \gamma_{i4}(f) \\ \gamma_{i5}(f) \\ \gamma_{i6}(f) \end{pmatrix} \quad (141)$$

b) Requirement for results endorsement

At first, it is not possible to have a null displacement at the blocked side for practical reason. In fact there is still a residual displacement level and acceleration level. Furthermore, the equation, which is used to calculate the dynamic transfer stiffness of the resilient mounting element (**Equation 10)**, requires that the driving point DTS at the blocked side must be high in comparison. Therefore, a relation between the acceleration levels between the input acceleration level at the centre of the exciting mass and the acceleration level at the top of the distributing plate emerged. Hence, the following inequality should be considered:

$$L_{a1}(f) - L_{a2}(f) \geq 20\ dB \qquad 142$$

Where L_{a1} is the acceleration level at the input exciting mass and L_{a2} is the acceleration level at the output distributing plate.

From a practical point of view, it is not possible to place the force transducers right at the bottom of the tested element as displayed in Figure 30. Although it is necessary to have this distributing plate, its behaviour through frequency should not have an influence on the results. The dynamic modal behaviour of the distributing plate could induce an error on the measurements of the forces. Therefore, its modal behaviour should be taken into account. The modal behaviour should not have a significant impact on the measurements if it is verified the following relation:

$$R = 0.06 \times \frac{10^{\frac{L_{F_2}}{20}}}{10^{\frac{L_{a_2}}{20}}} \geq m_2 \qquad 143$$

where m_2 is the mass of the distributing plate, L_{F2} is the force level at the output distribution plate and L_{a2} is the acceleration level at the output distribution plate. For more convenience, the ratio **R** was introduced and will be used in section IV.B.1.

This relation is equivalent to the following one:

$$L_{F2,8}(f) - L_{F2,11}(f) \leq 0{,}5\ dB \qquad 144$$

where $L_{F2,8}$ is the force level at the top of the distributing plate and $L_{F2,11}$ is the force level at the bottom of distributing plate.

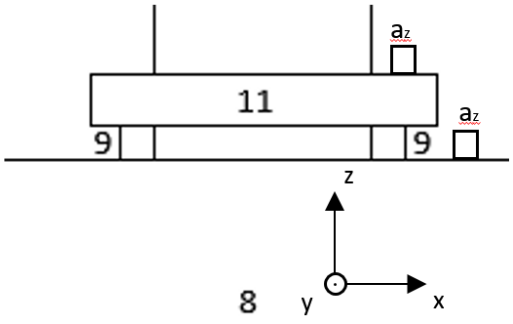

Figure 30: Bottom configuration

Figure 30 shows a configuration proposed by the standard. The force transducers (9) measure the forces on the test rig base (8) below the distributing plate (11).

Furthermore, to ensure good accuracy of the measures, the unwanted input vibrations should be as limited as possible. Indeed, it is not possible to acquire the DTS matrix components independently, if there is potential coupled responses due to unwanted response of the tested element. The standards recommend to avoid theses potentials coupling. The manner to avoid the coupling depends on the test rig configuration, but for a vertical axial direction excitation, which is the case in this thesis, the following relations should be certified:

$$L_{a1z}(f) - L_{a1x}(f) \geq 15\ dB \quad (145)$$

$$L_{a1z}(f) - L_{a1y}(f) \geq 15\ dB \quad (146)$$

where L_{a1z} is the acceleration level of the exciting mass in the vertical direction (main exciting direction) and L_{a1x} and L_{a1y} are the transverse acceleration levels of the exciting mass. As it already said, the axial symmetry of the RME helps also.

Considering the structure of the tests rig, it is possible to obtain flanking vibration transmission during the test. This vibrations originate from the exciter but spread in all the structure, especially through the pillars. As presented in Figure 29, the pillars are fixed to the basement, thus the flanking vibrations could disturb the measurement. However assuming the possible multiple arrangements of the test rig, the standards does not provide specific measurement requirements.

In the light of frequency related study, possible resonance modes of the test rig itself could disturb the measuring physical quantities. Then to ensure the good quality of the results, it is recommended to have the first natural frequency of the test rig 2 or 3 times higher than the maximum frequency reached during the test. Thus, it means that the possible frequency range of the study should be low depending on the mass or inertia of the test rig and its stiffness.

As it was previously displayed in section the I.B.4, the behaviour model of resilient mounts are not perfectly linear due to the behaviour of the constitutive rubber which only can be considered as a linear material in specific amplitude deformation range. However, a linearization at the working point is possible. For a specific pre-load, the system could be potentially considered linear if the dynamic transfer stiffness is invariant and respect the principle of superposition and proportionality. Thus, if, for two respecting input signals level A and B in a specific frequency range, with the B signal level 10dB higher, the relevant DTS levels do not differ by each other by more than 1.5 dB, the results should be regarded as good.

Finally, the tests should be considered reproducible, to be able to represent . Thus, a particular attention should be taken on the RME compression phase before the dynamic one. Indeed, possible variations are possible, coming from the positioning of the tested element, the speed of compression or the rubber relaxation. In order to avoid the variations, actions were adopted such as, the use of positioning tools or the respect of a buffer time of 24 hours between the end of the compression phase and the beginning of the dynamic test. Therefore, the initial parameters of the dynamic characterization, such as static deformation, can be considered constant and not to have a significant effect on the results.

2. ISO 6721 for the DMA

As it was previously evoked, the determination of the viscoelastic property of material, especially elastomer, is necessary to potentially predict its behaviour when subjected to vibration sinusoidal excitations. Among the possible ways to obtain the property of polymeric material, it is recommended to perform a dynamic mechanical analysis (DMA).

In the framework of this study, the DMA is focusing on the determination of the polymer linear viscoelasticity, more specifically on the determination of the complex moduli of the material. For a material which is mainly subjected to traction-compression or bending, the outcome parameter is the complex Young modulus E*. For a material which is mainly subjected to shear, the complex shear modulus G* is measured. These parameters depend on the excitation frequency, the temperature as well as the static and dynamic strain or stress states.

Among the DMA test procedures, it is advised to follow the ISO 6721 standard untitled: “Plastics - Determination of dynamic mechanical properties” for the linear viscoelasticity dynamic analysis, even if this standard is focusing on plastics materials instead of elastomers such as rubber. In fact, the complex moduli magnitude order of the rubber materials is the same as for plastics for the linear viscoelastic aspect.

a) Standard description

The standard prescribes several methods to perform DMA using several experimental dispositions to measure the complex moduli when the tested element is subjected to sinusoidal excitation. These moduli may be divided in two separate parts (real and imaginary): the storage and loss moduli with the following formulation:

$$M^* = M' + iM'' \tag{147}$$

where *M** is the complex modulus, *M’* the storage modulus and *M”* the loss modulus, both are expressed in Pascal (Pa). The modulus *M** may also be expressed in term of magnitude and phase angle such as:

$$M^* = |M| \times e^{i\delta} \tag{148}$$

where $|M|$ is the magnitude and δ is the phase angle.

Magnitude and phase angle are related to the storage and loss moduli by:

$$|M| = \sqrt{(M')^2 + (M'')^2} \tag{149}$$

$$\tan\delta = \frac{M''}{M'} \tag{150}$$

tan δ is also named “loss factor”.

In this thesis, compression is the main deformation mode on the RME. Thus, among the moduli, the studied one is the complex Young modulus. The procedure to determine the module is then simple and similar to the procedure for the DTS experimental characterization of the RME. The tested specimen is first pre-compressed and then subjected to mechanical oscillations. In our study, a static displacement was first imposed up to the required elastomer deformation then dynamic oscillations were applied. The resulting reaction force was then measured, as presented in figure 14.

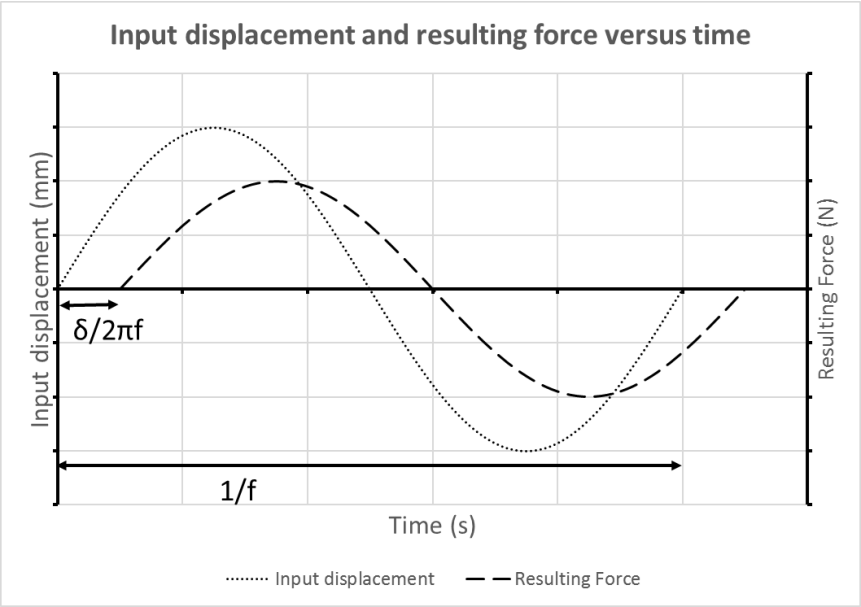

Figure 31: Input displacement and output froce measured in the DMA test

At first it is necessary to define correctly the input parameters required for the DMA test in order to obtain exploitable results. These parameters depend on the specifications of the test element application, the capacity of the test bench and the dimension of the specimen. Acknowledging the fixed specifications for the application, the dimensioning of the tested rubber specimen depend only on the bench characteristics.

b) *Samples dimensioning*

The device used during this campaign is a DMA test bench with the following characteristics:

- Low Frequency range mode: from 10-3Hz to 100Hz
- High Frequency range mode: from 5Hz to 200Hz
- Imposed dynamic force range : max 150N / min : 10-4N
- Imposed displacement range: +/- 1000 µm
- Sensibility: 10-3mm

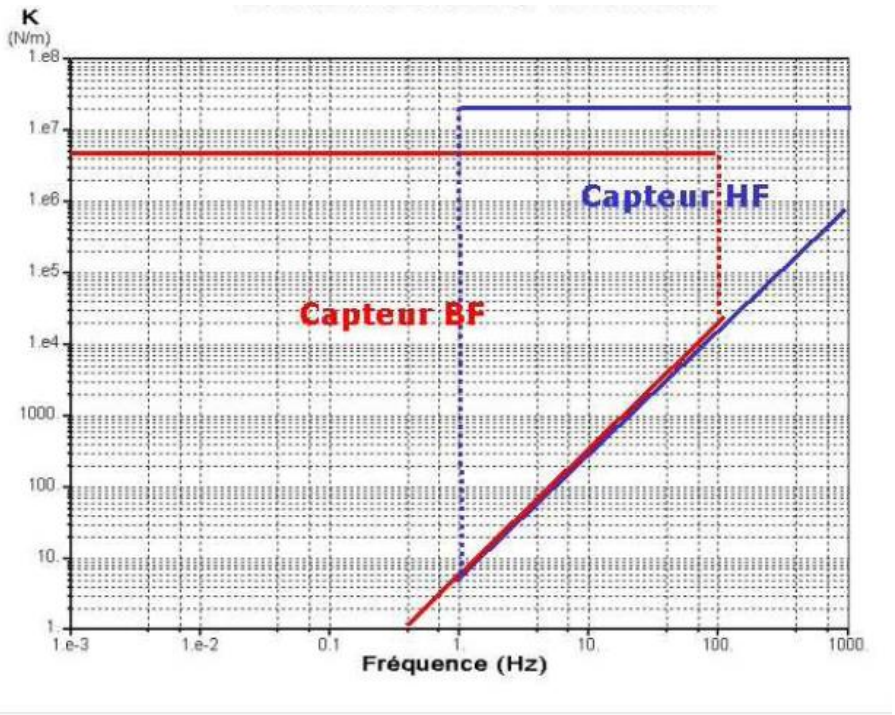

Figure 32: Sensors frequency range of accurate measurable stiffness

In Figure 32, the sensors (force transducers) working conditions are described. The sensor used for low frequency experiments ("capteur BF") is able to measure accurately the reaction force (and therefore the stiffness) between 10^{-3} and 100 Hz up to 4.10^{6} N/m, with restrictions between 1 and 100 Hz. The sensor used for high frequency experiments ("capteur HF"), as for it, is able to measure accurately the force (and therefore the stiffness) between 1 and 1000 Hz up to 2E+07 N/m, with restrictions.

The dimensioning of the specimen should respect two conditions for the measurements. At first, it should respect a shape factor F_c given by the following formula

$$F_c = \frac{1}{1 + 2 \times \left(\frac{S_e}{S_f}\right)^2} \qquad 151$$

Where S_e is the excited surface of the sample and S_f is the free surface.

F_c must be as near as possible to 1 but in all case it must be higher than 0.9, which leads to the inequality to respect when defining the sample dimensions

$$S_f \geq 4.25 \times S_e \qquad 152$$

The second shape factor F_f , which is the ratio between the height of the specimen and the excited surface, should be determine as the sample stiffness is in the measurable domain of the visco-analyser:

$$K = \frac{|E|}{F_f} \qquad 153$$

In our case, the expected stiffness has to be between 10^4 and 10^5N/m for a Young modulus approximately ranging between 10^6 and 10^7 Pa. This leads to a shape factor equal to **100 mm^{-1}**.

3. Finite element software

In the last years, thanks to the development of computers including more and more calculus power, the use of finite element method has drastically increased. At the beginning, FE codes were mainly used to assess the behaviour of structures submitted to static loads, where the main purpose is to resolve a static equilibrium equation. Dedicated software are now widely spread through the industrial field where they are available among the other tools to solve engineering problems.

Finite element numerical codes are nowadays also used to solve dynamic industrial problems. Numerical simulations are generally performed as substitution of experimental tests. For frequency response analysis, the classical resolution of the problem implies frequency dependent equations such as the ones presented in part I.B.2. However, in the thesis, the classical method is not adopted. On the contrary, in order to simulate correctly possible non-linear behaviours of the RME, the time dependent equilibrium equations are solved using step by step time integration scheme. Two types of time integration schemes are usually used: implicit and explicit.

Both time integration schemes allow to solve the characteristic equilibrium equation:

$$M\ddot{u}_t + C\dot{u}_t + Ku_t = F_t^{ext} \qquad 154$$

with:

$$Ku_t = F_t^{int} \qquad 155$$

where F_{est} are the external forces and F_{int} are the internal forces.

In implicit integration scheme, equation above is solved at time t+Δt:

$$M\ddot{u}_{t+\Delta t} + Cu_{t+\Delta t} + Ku_{t+\Delta t} = F_{t+\Delta t}^{ext} \qquad 156$$

with a prerequisite of knowing each physical quantities at time t and respecting the convergence of the solution at previous time step t. Here, the time step may be arbitrary fixed by the user and is generally around 10^{-1} or 10^{-2} seconds.

On the contrary, as the explicit integration scheme is concerned, the numerical solution depends only on the known physical quantities at time t. The numerical convergence is obtained by using a small time step, which depends on both the material characteristics and the dimensions of the smallest finite element. In explicit calculations, the time step is generally very small, around one microsecond or less.

The first drawback of the implicit integration scheme is the need to reach the force equilibrium at each time step, leading to an additional loop process within a time step. Furthermore, in order to calculate an accurate

transfer function using a discrete Fourier transformation, as presented in part I.B.1, it is necessary to have a sampling period or Δt small enough to ensure a good discretization of the sine signals. One may then loss the main advantage of the implicit integration scheme (large time steps).

Two different FE codes were used in the framework of this thesis: MSC Patran with its dedicated linear solver and LS-DYNA with its nonlinear solver.

Implicit and explicit integration schemes are implemented in LS-DYNA, allowing for the simulation of nonlinear material behaviour, such as hyperelasticity. On the other hand, MSC Patran/Nastran package is used for meshing, static simulations and linear normal mode analysis.

E. BIBLIOGRAPHY CONCLUSION AND SPECIFICITIES OF THE THESIS

After a small prospection about the use of passive isolators in the industry, the specificities of the passive isolators, and more specifically resilient mounting element, in maritime applications, were discussed with a brief presentation of the passive isolator working conditions, in term of potential dynamic excitations and working load.

Then, the theoretical background of the thesis, was presented. After a brief introduction of several mathematical features that were used in the thesis, the fundamental four pole parameter theory, that is the foundation of the experimental characterization method and, by extension, a fundamental point of the thesis, was examined. Then, the vibrations considerations were studied via the review damped oscillating system of and introduction of the transfer function. Furthermore, several material aspects were discussed, especially about the hyperelasticity and viscoelasticity of the rubber, as well as the material laws.

Moreover, the RME three possible characterization types were reviewed with the enhance of the interesting appeared features, such as some analytical models or particular numerical studies. The advantages and disadvantages were discussed.

Finally the specifications and practical aspects, concerning the experimental characterization and DMA were examined and a brief investigation on the functioning of the finite element software.

As it was mentioned, a similar study was conducted with relatively good results at the end concerning the validation of the developed procedure [41]. In this optic, the thesis procedure considered the previous procedure, leading to focus on several aspects, such as the consistency between the material laws or about the frequency range. Furthermore, as it was previously discussed, most of the human body natural frequencies are between 2 and 60 Hz. Therefore, the investigated frequency range of the thesis is fixed from 1 to 50 Hz.

To include the non-linearity of the rubber material, which is not the case for experimental characterization, it was decided to use a finite element software, that allowed the creation and execution of non-linear simulation for the numerical characterization of the RME.

As it was previously discussed, the compression of the rubber due to the working load, induced a change in the parameters of the rubber constitutive law. In fact, it increases of the rubber stiffness. To consider this feature, the rubber law parameter should be updated after the numerical static compression, to acquire an accurate DTS. Therefore, a characterization performed on the rubber was needed to evaluate the new rubber stiffness. This characterization was performed via a dynamic mechanical analysis. With the DMA it was possible to estimate the evolution of the rubber characteristics in function of the frequency, at the compression load static deformation.

The last specificities of the thesis concerns the possibility to compare two material law: the Yeoh hyperelastic laws and the Hook law. Using the consistency between the Yeoh model and Hook law, it was, at first, possible to estimate the Young modulus of the rubber. The value of the Yeoh coefficient was obtained from a previous study [41]. Then, after the first numerical quasi-static simulation it could be possible to compare the results obtained with the two material laws. If the difference between the results is small, the Hook law could be sufficient to model the rubber behaviour for further simulations.

II. PRELIMINARY STUDIES

Before the determination of the dynamic transfer stiffness (DTS) with the experimental or numerical methods, preliminaries studies were necessary. In fact, the experimental determination of the dynamic transfer stiffness in the low frequency range required the design of a specific test rig as it was displayed previously in part II.C.1. To acknowledge the influence of the pre-compression on the elastomer, a dynamic mechanical analysis at the exact element static pre-deformation strain was needed. Thus, it is necessary to obtain the strain deformation field in the element using static simulation results. This static simulation represents the compression of the element when the working load, presented in part I. is applied. Additional investigations on the natural frequencies and mode of the RME were imperative to endorse the DTS determination and avoid possible unwanted behaviour, especially during the experimental characterization.

In this part, the design of the test rig will be exposed, constituted by numerical simulations, static and normal modes analysis of specific elements of the structure. Then the static simulations on the RME will be presented. In the end, the RME normal modes analysis displayed.

A. DESIGN OF A CUSTOM TEST RIG

The design of the test rig was the first activity effected during the PhD. This design was achieved respecting ISO 10846-2 standard specifications the dynamic behaviour of the test rig and arbitrary fixed prescription for the static aspect. The CAD design of the test rig is presented in Figure 33.

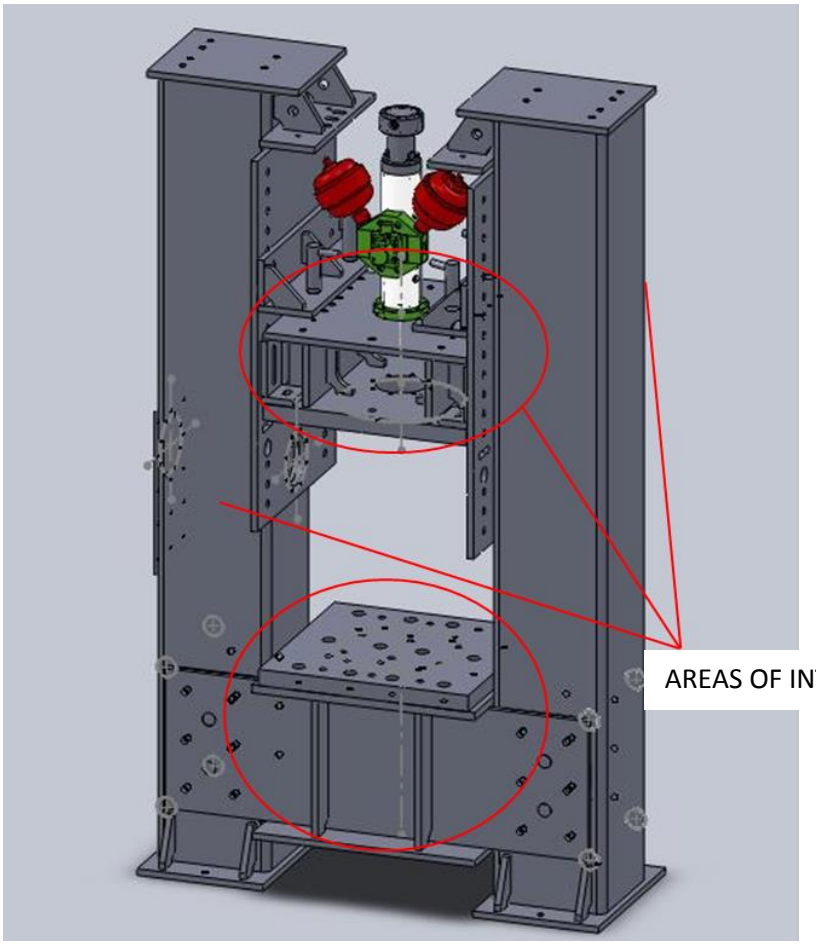

Figure 33: CAD isometric view of the test rig

In the future, this test rig will be principally used for experimenting various configurations of loading on specific samples and not only the T200 RME. The main part of the experimental campaigns will concentrate on the determination of the DTS of the tested sample at low frequencies according to ISO 10846 standard. As a consequence, the structure should be capable to sustain all type of loading configurations at low frequencies.

In this test rig design, the compression load was an important feature to focus, mostly because of the lack of specifications from ISO standards. This compression load is created by pistons that are connected to a manually pump controlled by the user. Each piston is able to apply a force up to 2500 N. At first, the RME specimen is placed, and then the moveable is carefully installed on the tested RME after the placement of the exciting mass. After this careful installation, the compression is performed using pistons. At the end of the compression load, the moveable traverse is bolted to the test rig structure. Finally, the dynamic test can be launched. A more exhaustive description of the test rig mechanics is described in the experimental campaign part.

The design of the test rig was based on following requirements:

- The test rig foundation should sustain a maximum compression force of 9.81E+04 N applied on the T200 RME which is transmitted to the foundation.
- The first natural frequency of the test rig frame should be 3 times higher than the studied frequency range upper bound.
- The exciting mass should behave as a rigid body at the studied frequencies
- The moveable transverse should sustain the reaction force of the element and should also behave as a rigid body at the studied frequencies

When the test rig conception was initiated, above requirements led to consider specifically some components of the test rig: the foundation, the moveable transverse, the exciting mass and the pillars.

Firstly, a global analysis was performed to assess the response of the global structure to different loads. The dimensions of the main components of the test rig were arbitrary fixed before performing any calculations. Then, the first calculations were executed and the dimensions that brought to unacceptable reactions of strains and stresses were changed. The successive steps of this step by step analysis will be not presented in this work, excepting the simulations based on last two models. The maximum admissible Von Mises(?) stress inside in the steel test rig frame and other critical parts was fixed at 160 MPa.

At the end of the test rig dimensioning, two similar models emerged. In fact, as displayed in Figure 33, the moveable traverse is bolted to the frame of the test rig. In the numerical simulations, it is difficult to model the connexion between bolted parts due to the complex connexion modelling between the screw and the bolt. If it is bolted with a sufficient tightening torque, the link is considered rigid but the effect of vibrations on the bond rigidity could decrease. Therefore one model will consider the bonds between the moveable traverse as rigid and the other does not integrate the moveable traverse in the frame (no bonds). Figure 34 displays the resulting two finite element models, both meshed using 2D QUAD elements.

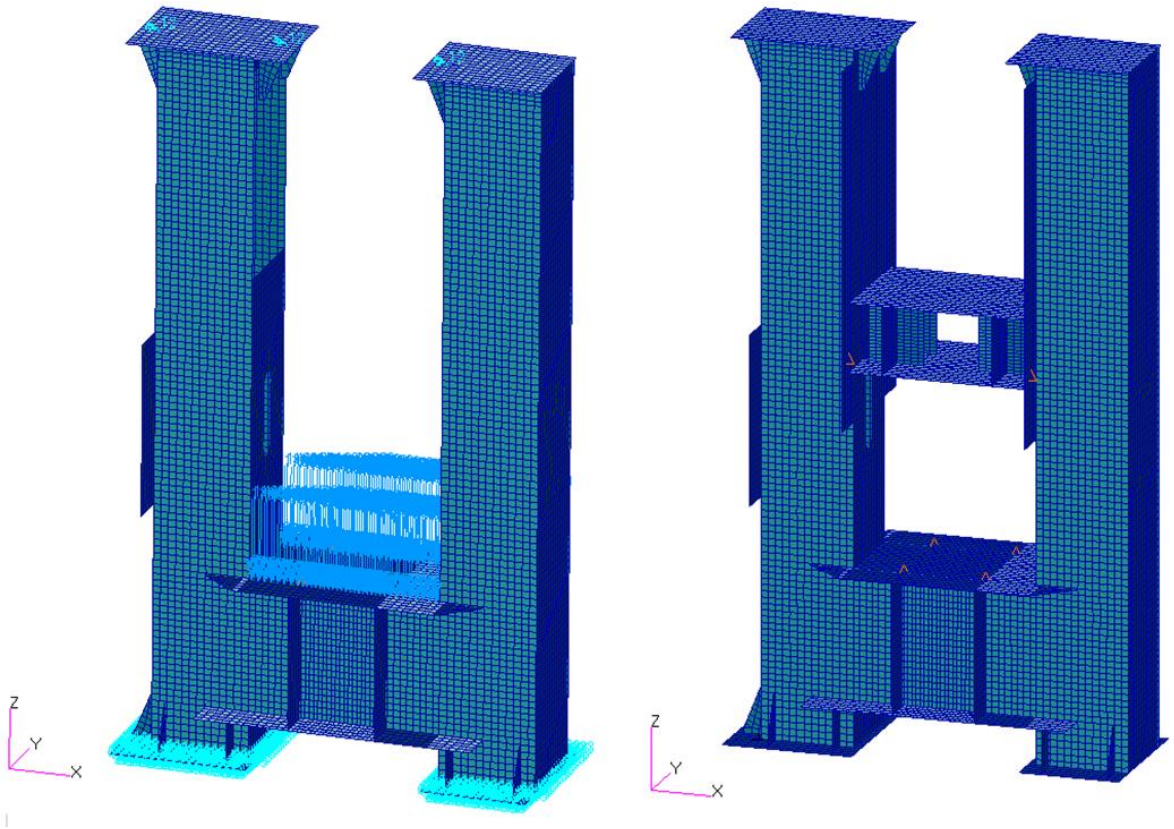

Figure 34: Isometric view of the two FE model

Two types of simulations were performed. The first one consisted in a static compression applied in the base frame of the test rig and in parallel a normal mode analysis of the unload frame. In Figure 34 the static load is represented by blue arrows applied in both models but are displayed in only one for clarity. As the static load, the boundary conditions, also displayed in only on model, are represented in cyan colour. To model the influence of the other components placed during the experiment (sample, piston, etc.), several punctual added mass are added on the frame, as displayed in Figure 34 by orange triangles.

1. Static analysis of the test rig frame

Although the working load of the T200 resilient mount corresponds to a force of 74 kN applied vertically on the element, it was decided to increase the compression force that should be sustained by the test rig up to 98 kN. This 25% increase allows to be conservative in our study and to use higher applied loads in the future.

The location of the maximum load was supposed to be located on the base frame. Then, the stresses are post-processed in this area. Although the two models are not the same, the resulted stresses in the base frame were similar, and somehow identical. Therefore the result post-treatment are presented for only one model. The Von MIses stresses are displayed in Figure 35.

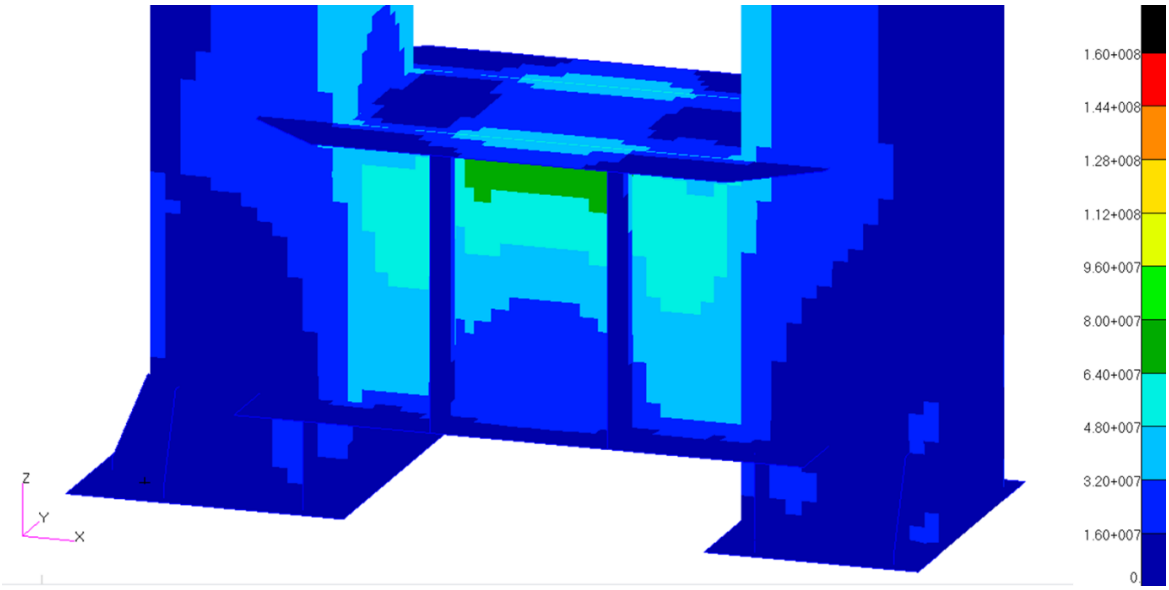

Figure 35: Von Mises stress in the base frame in Pascal (Pa)

For the resistance study of structure, the Von Mises stresses are post-processed and plotted in Figure 35. It appears that maximum values are less than 80 MPa, which shows that the proposed test rig is able to withstand the aforementioned maximum loads.

Another investigated point concerns the resulting local displacements after compression. Indeed, too much displacements may create errors in the measured dynamic displacement which depend on the reference point, and then, disturb the control management system, due to the displacement control (input displacement) (?). However, no requirement regarding the maximum deflection discussed exists in ISO standard (10846-2). As for the stress state post-treatment, results related to only one model are presented here.

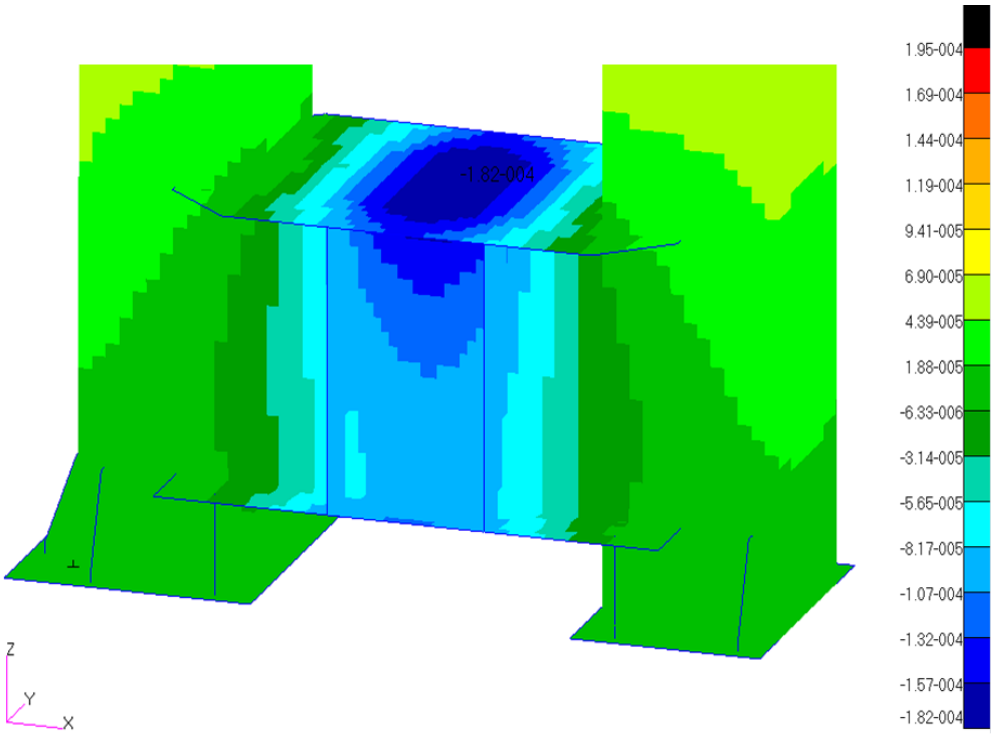

Figure 36: Static vertical deflection in m (z-axis) in the base frame in mm

The base frame vertical displacement field post-processed along z-axis is plotted in Figure 36 and it appears that the maximum deflection does not exceed 182 µm. Displacement fields along x and y axes were found significantly lower and are not displayed here.

2. Dynamic investigations of the test rig frame

After the static dimensioning, the modal characteristics of the test rig were also investigated. Unlike static results in terms of stress and deflection, the dynamic behaviours of the two models are quite different. A modal analysis was carried out to investigate the behaviour of the structure submitted to harmonic excitations and to verify the condition specified by the ISO standard concerning the lowest natural frequency of the test rig in relation to the planned frequency range of study [1Hz-50Hz].

a) First model

The first finite element model supposed that the link between the moveable traverse and the test rig frame is rigid. Therefore, the influence of the moveable traverse is considered in the model. Hence, its influence on the dynamic behaviour of the test rig structure could be determinant. In consequence, a normal mode analysis is required to evaluate this influence. Figure 37 shows the first normal mode of the structure.

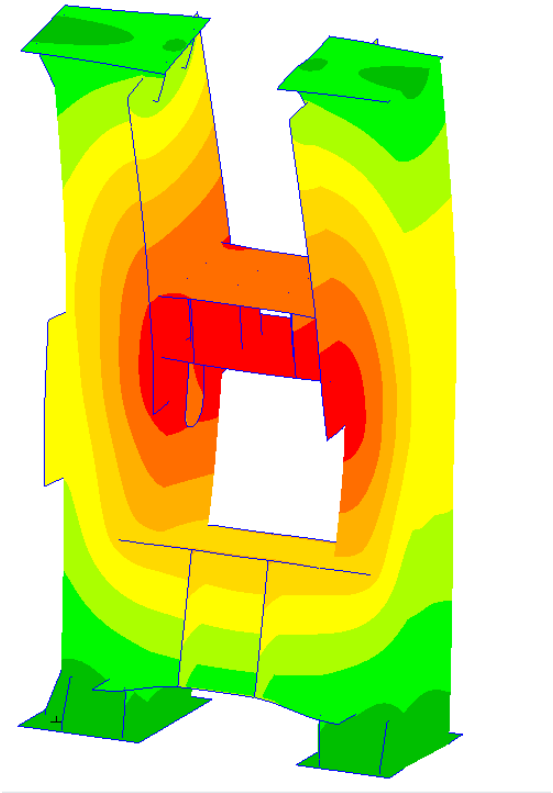

Figure 37: first normal mode of the first test rig model at 133Hz

The first mode of this model is a bending mode along the x-axis at 133 Hz. This mode is not as problematic as a translation mode along the z-axis would be. However, it may lead to measurement disturbance on the displacement captor so this first natural frequency (133 Hz) constitutes the highest operating frequency of the test rig.

Figure 38, as for it, shows the second normal mode of the structure.

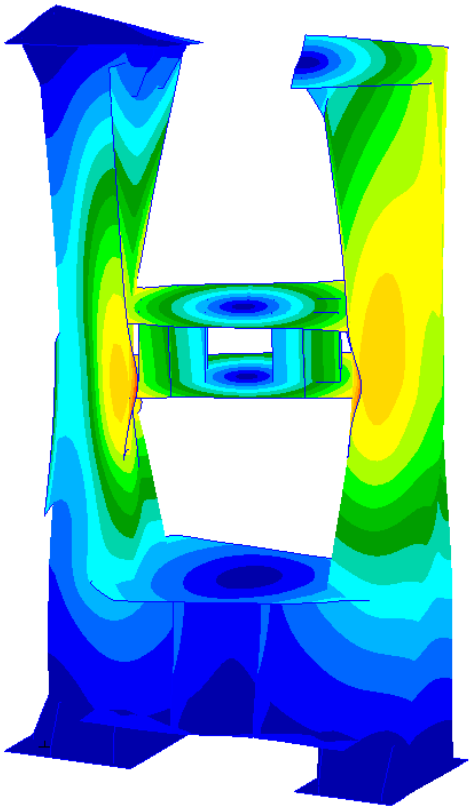

Figure 38: second normal mode of the first test rig model at 153 Hz

The second mode is a rotation mode along the z-axis at 153 Hz. This mode is also not as problematic as a translation mode along the z-axis but it is still problematic and limit the operating frequency range, especially because it may induce unwanted stresses inside the link between the moveable traverse and the frame.

Figure 39, as for it, shows the third normal mode of the structure.

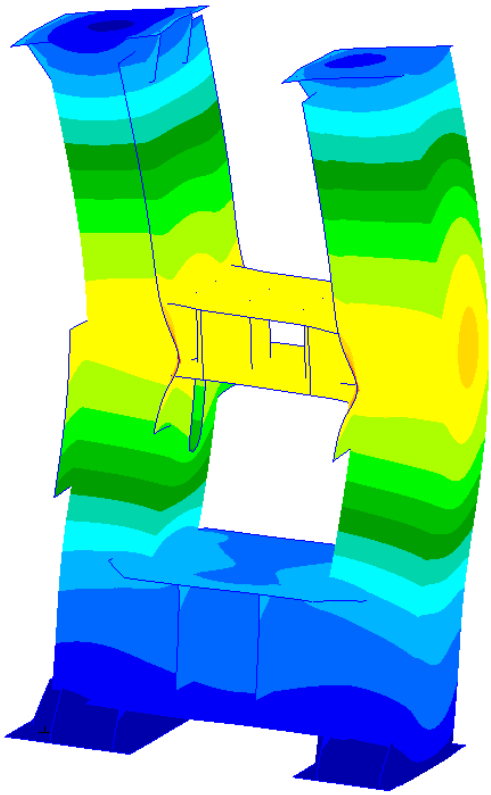

Figure 39: third normal mode of the first test rig model at 155Hz

The third mode is a bending mode along the y-axis at 155 Hz. This mode is also not as problematic as a translation mode along the z-axis but it also could induce unwanted stresses inside the link between the moveable traverse and the frame.

b) Second model

As it was previously mentioned, a second model was necessary regarding the dynamic behaviour of the test rig. In this model, the link between the moveable traverse and the test rig frame (pillars) was not considered as rigid. The modelling of the deformable connexion between the two parts being very complex, it was decided to ignore the moveable traverse in this model. With the help of the results from the first model, the dynamic behaviour of the real test rig may be estimated. In this case, the first natural frequencies of the real test rig were supposed to be close to the results obtained from both models. Regarding the second model, only the first four normal modes were post-processed. Figure 40 shows the first normal mode.

The first and second modes of this structure, presented in Figure 40 and Figure 41, are torsional mode of test rig pillars, respectively at 149 Hz and 160 Hz. These normal modes should have a negligible impact on the measurements during the experiments.

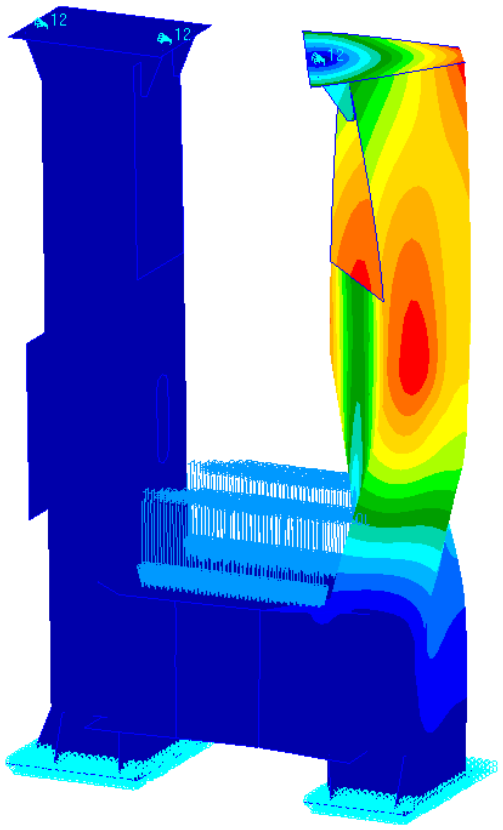

Figure 40: first normal mode of the second test rig model at 149 Hz

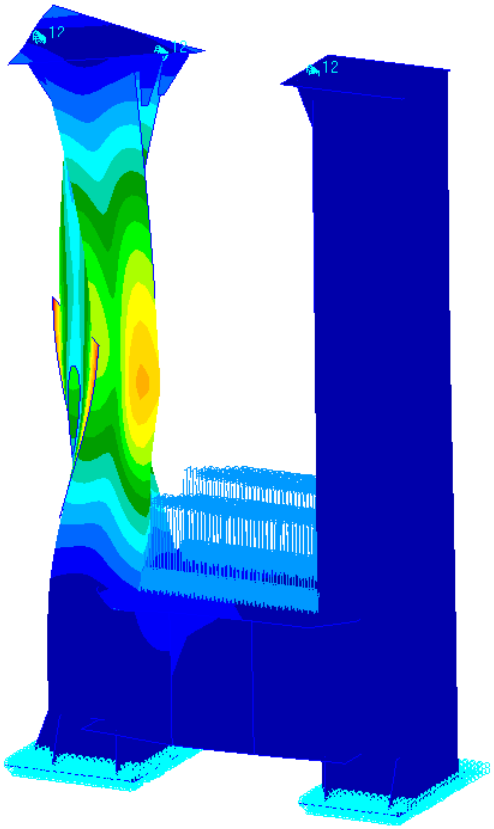

Figure 41: second normal mode of the second test rig model at 160 Hz

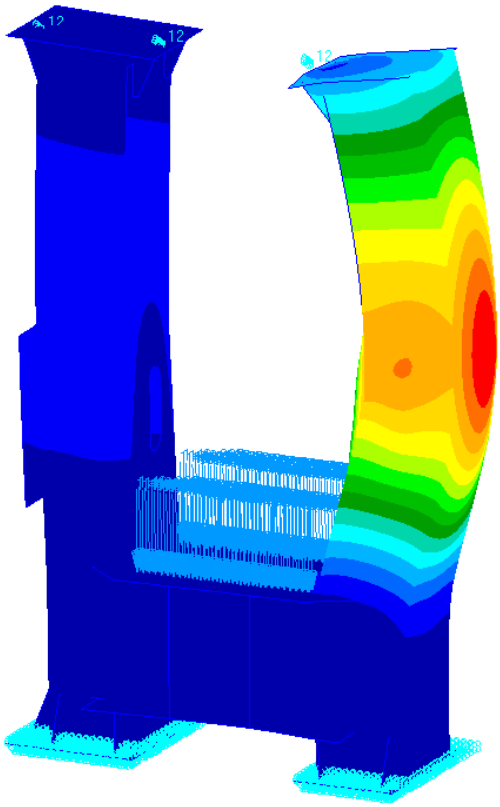

Figure 42: third normal mode of the second test rig model at 163 Hz

As shown in Figure 42 and Figure 11, the third and four modes are bending modes of test rig pillars, both at 163 Hz. As for the previous modes, these normal modes should have a negligible impact on the measurements during the experiments.

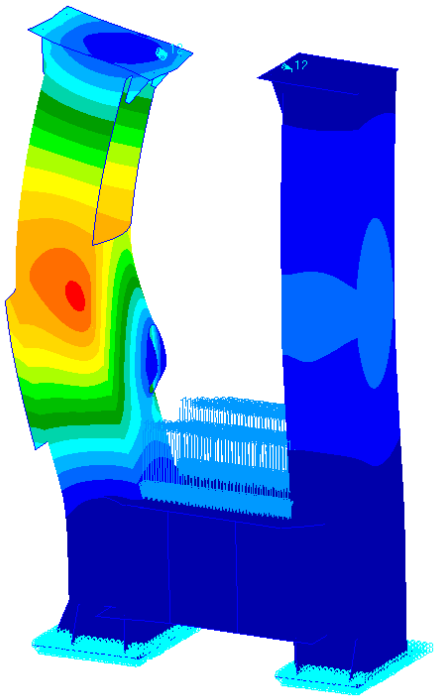

Figure 43: fourth normal mode of the second test rig model at 163 Hz

In conclusion, concerning the frequency limitation of the test rig, the first model should be taken in consideration due to, at first, the lowest frequency that emerged from this model, and the related bending mode that can induce some disturbance in the measurements. Then, it limits the use frequency range up to **44** Hz, three times lower less the minimum lowest frequency of the test rig. This could be problematic when performing the test in the frequency range between 44 Hz and 50 Hz, and particular attention will be taken during the tests.

3. Exciting mass dynamic behaviour

The modal characteristics of the exciting mass have also been studied. In this case, the main purpose is to verify its dynamic behaviour within the experiment frequency range. Indeed, the dynamic response of the exciting mass may disturb the experiment if its natural frequencies lie within the frequency range of the experiments. In this test rig, the exciting mass is a steel disk with the following dimensions:

- Diameter: 500 mm
- Height: 60 mm

In this work, the first third normal modes were calculated. Figure 45: displays the finite element model of the exciting mass, while Figure 13, Figure 46, and Figure 47 show the three first natural mode shapes.

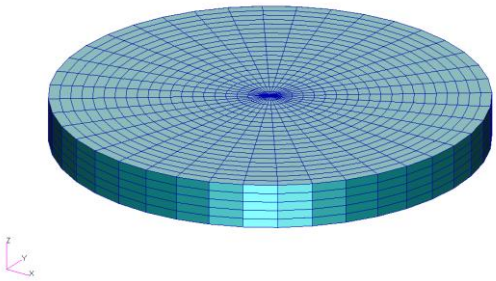

Figure 45: FE model of the exciting mass

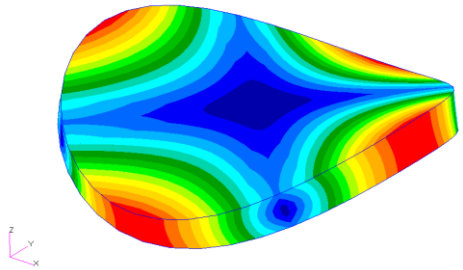

Figure 44: first mode of the exciting mass at 1200 Hz

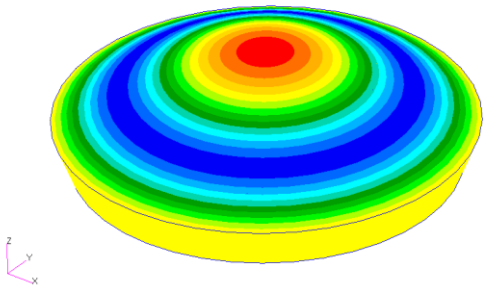

Figure 46: second mode of the exciting mass at 2002 Hz

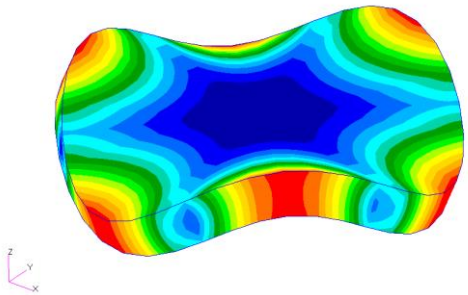

Figure 47: third mode of the exciting mass at 2625 Hz

As it is displayed in Figure 13, the first normal mode appears at 1200 Hz, quite higher than the maximum planned frequency of the test rig experiments. This normal mode is a first order bending mode. The second appears at 2002 Hz and is also a first order bending mode. The third one, as for it, appears sat 2625 Hz and is a second order bending mode.

In conclusion, the exciting mass should behave as a rigid-body in the expected test rig frequency range from 1 or 2 Hz to 50 Hz and should have a negligible impact on the measurements

4. Moveable traverse behaviour study

Finally, the last critical part of the test rig that should be investigated is the moveable traverse. Indeed, this component ensures 1) the good transmission of the static loads applied by the pistons, and 2) the stability of the dynamic exciter which it is fixed on the moveable traverse upper plate. Therefore, a static simulations has to be performed to verify the capacity of the moveable traverse to sustain the static loads (9.81E+04 N) and the reaction of the tested specimen. A normal mode analysis must also be carried out to ensure that the moveable traverse behaves like a rigid body in the experimental frequency range, as the exciting mass. Figure 48 displays the corresponding finite element model.

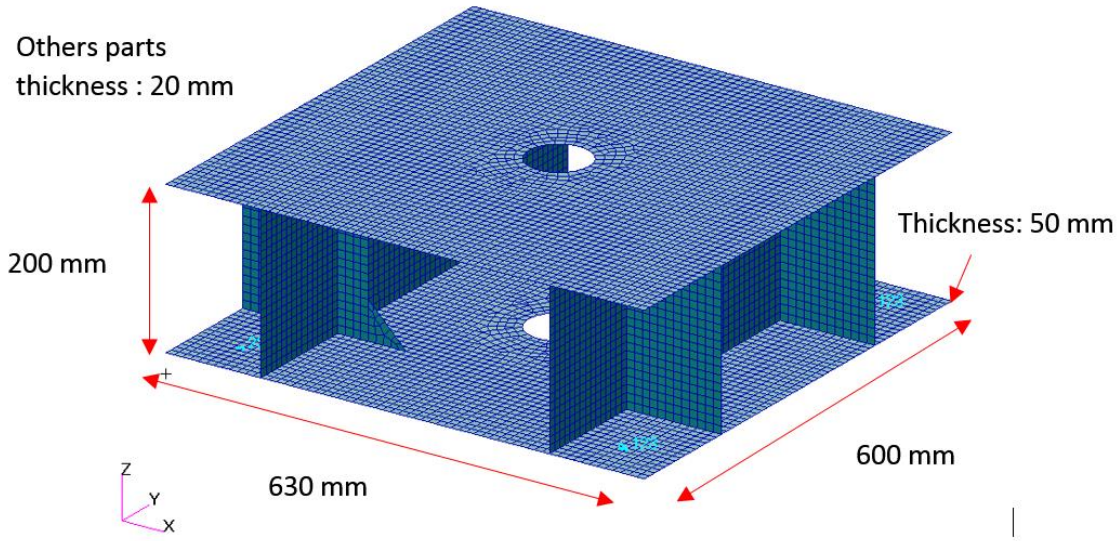

Figure 48: Finite element model of the moveable traverse with its dimensions

To verify the capacity of the moveable traverse to sustain the static loads, a static simulation is effected. To ensure the pertinence of the static simulation it is necessary to model a configuration of the test where the system reaches a mechanical equilibrium. The only configurations where the mechanical equilibrium is reached is the one obtained after the compression phase where the moveable traverse is bolted to the test rig frame and endure the reaction force of the tested sample that is equal to the static load.

The movable traverse is constrained along the three directions at bolted connections with the frame and the static load is represented by a compressive load field. Figure 49 displays the bottom view of the movable traverse where the compressive loads (internal radius = 0.25 m; exernal radius = 0.5 m) are represented in dark blue colour and the boundary conditions in cyan colour.

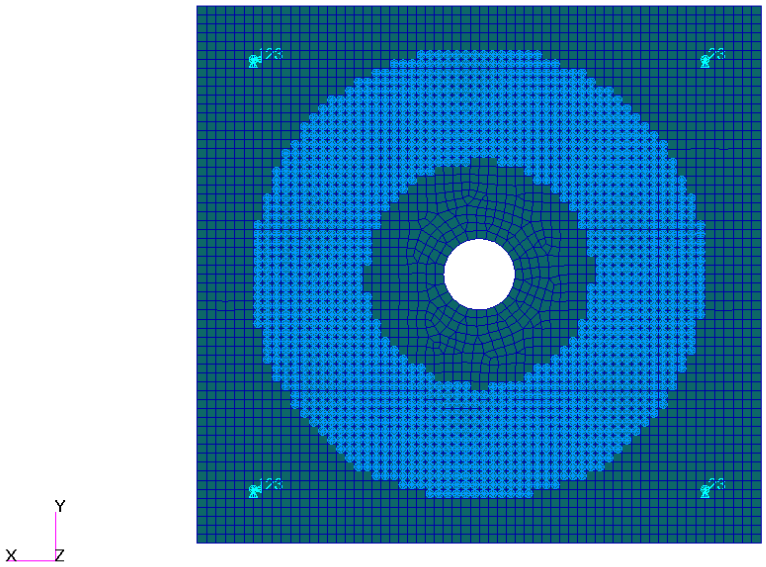

Figure 49: Bottom view of the moveable transverse

Figure 50 displays the resulting Von Mises stresses distribution through the moveable traverse.

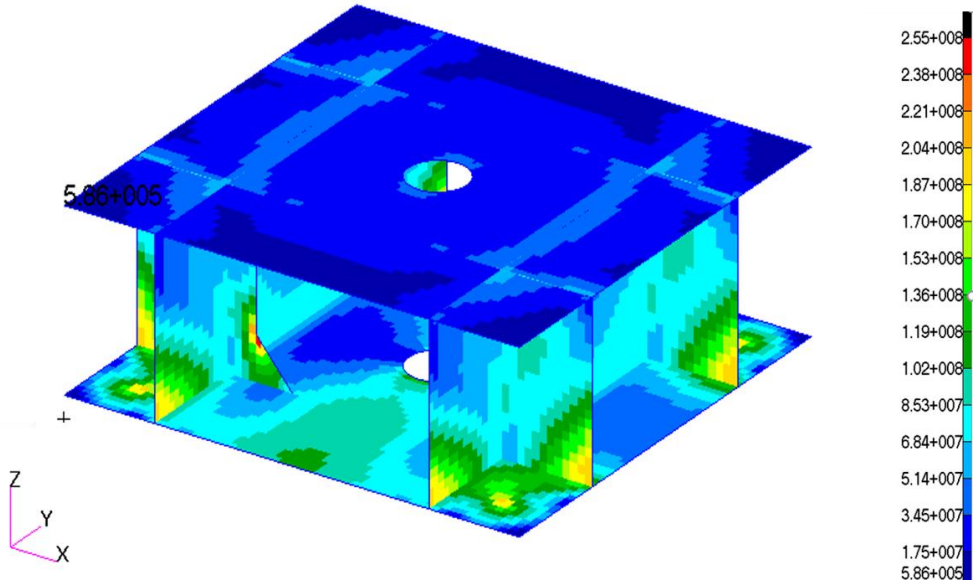

Figure 50: Von Mises stresses in the moveable traverse in Pascal (Pa)

Excepting some local stress concentrations where the stresses exceed the maximum stress criterion of 160 MPa (255 MPa and 204 MPa), the stress levels do not exceed 150 MPa for a compression load of 9.81E+04 N that is 25 % higher than within the RME experimental characterization where the compression load is about 9.81E+04 N. Then, it is possible to consider that the moveable can withstand the compression load.

Figure 51 displays the resulting vertical displacements in the moveable traverse.

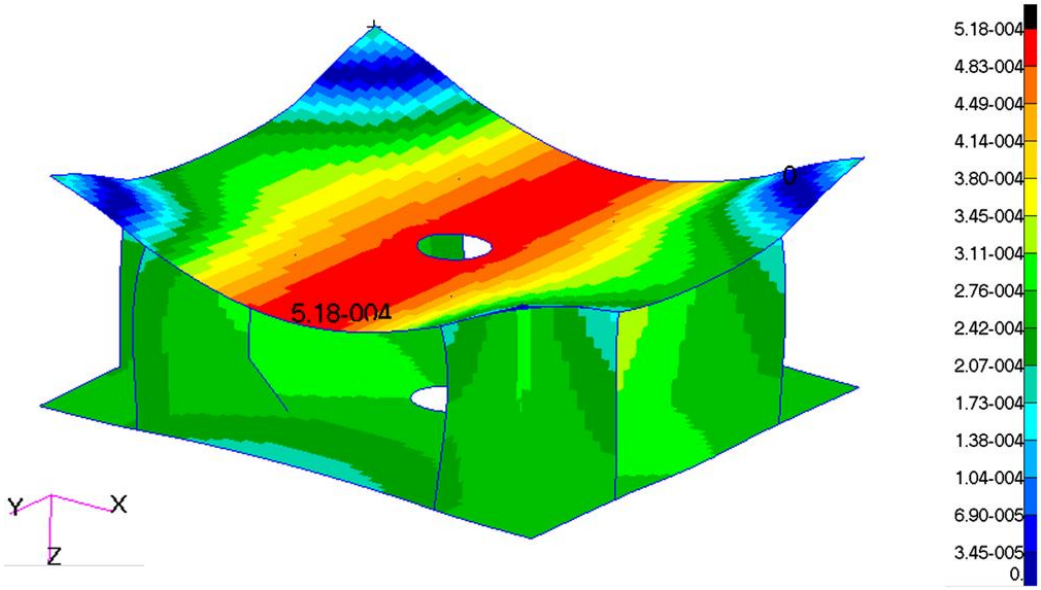

Figure 51: Vertical relative displacements in the moveable traverse in m

The resulting 0.5 mm maximum relative vertical deflection is considered as acceptable due to its relative limited impact on the measurements.

The last simulation that was planned in the preliminary studies concerning the test rig design was a normal mode analysis of the moveable traverse. Actually, the dynamic behaviour of the moveable traverse may lead to disturbances in the measurements during the experimental characterization. In this analysis, only the first four modes were post-processed.

As shown in Figure 52, the first mode corresponds to local bending along y-axis of the upper plate at 488 Hz and should have a negligible impact on the measurements during the experiments.

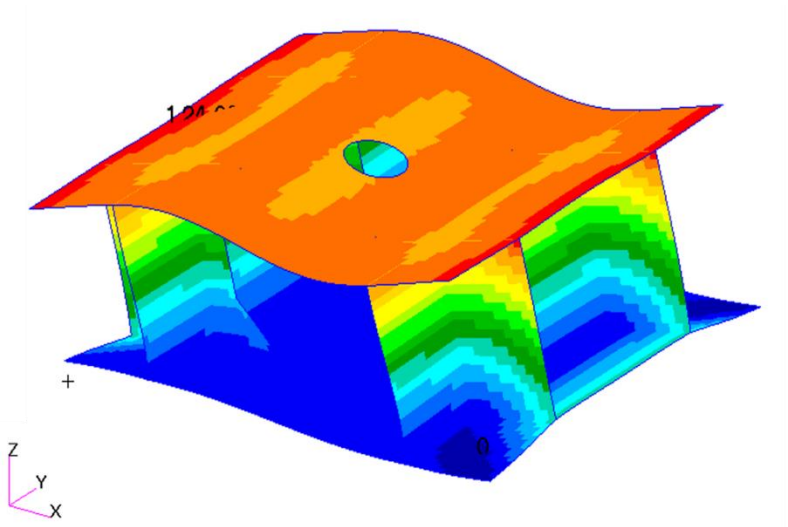

Figure 52: First mode of the movable traverse at 488 Hz

The second mode of this structure, shown in Figure 53, is a complex bending mode at 583 Hz, which should also have a negligible influence on the measurements.

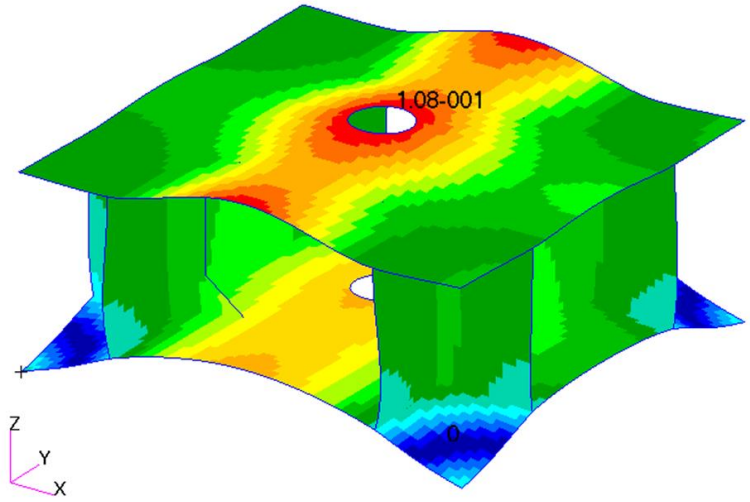

Figure 53: Second mode of the movable traverse at 583 Hz

The third mode presented in Figure 54 is a local bending mode of traverse upper plate along x-axis at 691 Hz. Like the two first normal modes, this one should also have a negligible impact on the measurements.

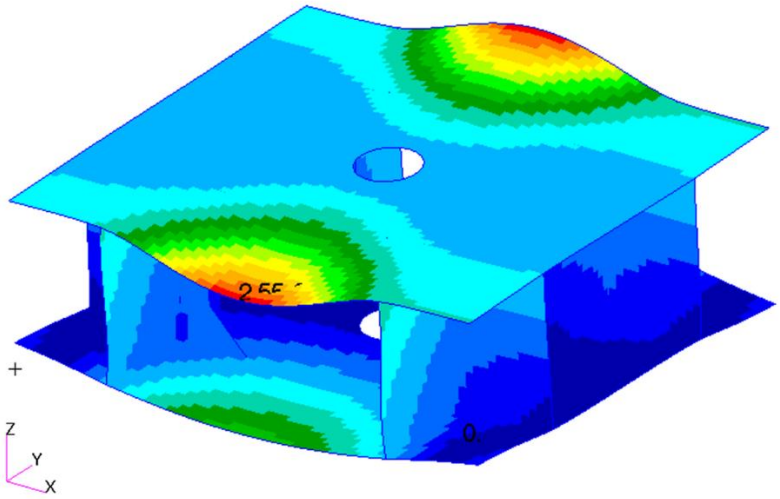

Figure 54: Third mode of the movable traverse at 691 Hz

Finally, the fourth mode represented in Figure 55 is a global torsional mode and, like the other ones, should not disturb the measurements.

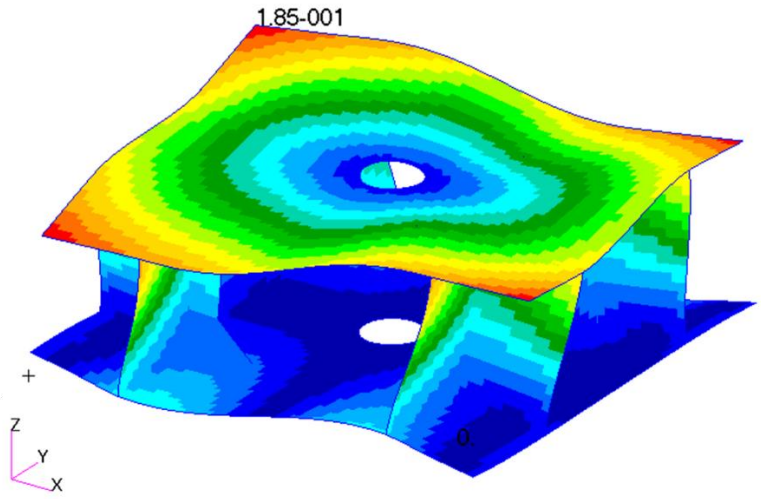

Figure 55: Fourth mode of the movable traverse at 769 Hz

To conclude, the moveable traverse static deformation is considered as sufficiently small to not disturb the measurements. Moreover, its dynamic behaviour can be considered, like the exciting mass, as a rigid-body behaviour within the experiment frequency range [1Hz-50Hz].

Concerning the design of the test rig, the only limitations that appears during this design concerns its dynamic behaviour. The test rig structures can endure the different loading conditions resulting from the static compression. The only issue concerns on of the test rig configuration where the moveable traverse is considered rigidly fixed to the test rig frame. In this configuration, the first natural frequency of the modelled structure is less than three time higher than the maximum frequency of the planned experimental frequency range. However, due to the two potential configurations, it is difficult to conclude that the first natural frequency of the real test rig is three times higher than the of the planned frequency range.

B. STATIC SIMULATION OF THE RME

After the conception of the test rig, the second part of the preliminary studies focused on the setting of the numerical models to simulate static and dynamic behaviours of the Resilient Mounting Element. The initial setting focus, at first, on the numerical calibration of the static load of the RME. A first numerical calibration of the numerical model was performed by Moro L. [40] and gave initial law parameters that will be used in the numerical model developed in the framework of this thesis. This calibration was performed in accordance with the static deflection curve, introduced in section I.A.3. In the present thesis, a quasi-static simulation representing the compression of the T200 at the working load was performed. The working load of the T200 was fixed at 74 KN, which corresponds to 10 mm vertical deflection, according to the static deflection curve. Therefore, the resulting T200 static deflection of the numerical model should be 10 mm. The first and main objective of the static simulation was to obtain the 3D strain field in the rubber material. This strain field is required to initiate the dynamic mechanical analysis (DMA) which will provide an updated material law with new coefficients (Yeoh coefficients and Young modulus principally). The second objective of the static simulation was to compare two models. In the first model, the rubber behaviour was represented by a hyperelastic material law and in the second one by a classical linear Hook law. If the post-treated results were sufficiently close, it would be possible to use only one material law to model the rubber behaviour. A last objective was perform a modal analysis in order to calculate the modal characteristics of the RME (natural frequencies and mode shapes)

1. T200 Finite element model

The numerical simulations of the T200 RME are based on the finite element approach, which is derived from the continuum mechanic theory. The continuum mechanic formulates the relations between several mechanical features such as deformations and loads for example. This features are divided in categories. Thus, the T200 finite element model developed in the framework of this thesis is composed of several features that can be classified in specific categories.

At first, the main category of the finite element model set with LS-DYNA software is the part. A part is related to a material law, which relates stresses and strains in solid finite elements (mesh). Furthermore, the relations between the parts and the external environment compose the second category. These relations can also be separated into two separate groups: the boundary conditions and loadings. Similar to the boundary conditions and loadings, the relations governing the contacts between parts constitute a third category. The last category contains all the material laws of the model. Therefore, the FE model will be presented according to these categories.

Furthermore, the mesh of the finite element model has been completed using MSC PATRAN software. The simulations have been performed using LS-DYNA solver where it is possible to use a hyperelastic law to model the behaviour of the rubber.

a) Part Meshing

Acknowledging the potential symmetries of the RME, it has been possible to model only a quarter of it, the objective being to limit both the FEM size and the simulation time. This model was also used to model the RME response when it is submitted to dynamic vertical excitation, which is the main subject of the investigation in the thesis. Figure 56 shows the corresponding model meshing. All finite elements are 8 or 6 nodes reduced-integrated solid elements.

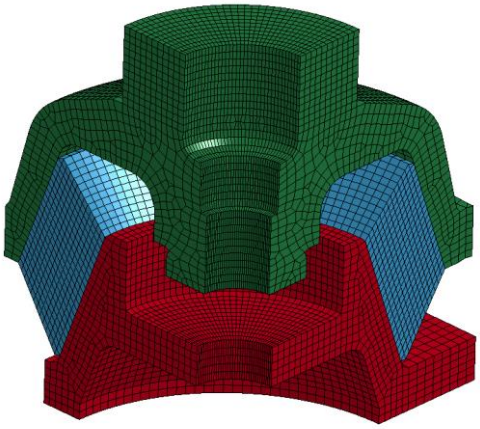

Figure 56: Finite element models of a quarter and half RME under LS-DYNA

The upper (green) and lower parts (red) are associated to a like-steel purely linear elastic material law. The intermediate part (blue) is associated to a hyper-elastic or linear elastic law. The viscosity was not implemented in the static calculation because of the irrelevance of its implementation. In a quasi-static simulation, variation of the displacements in function of the time are considered null.

b) Boundary conditions and loadings

The quarter RME PATRAN model is associated to several boundary conditions representing the symmetry effects. Rigid beam elements (yellow) allow to link all the upper nodes to a central one (fictive) on which a torque or a force can be applied. Then, the rigid beams were not used with vertical loadings that are applied on the steel top casting nodes.

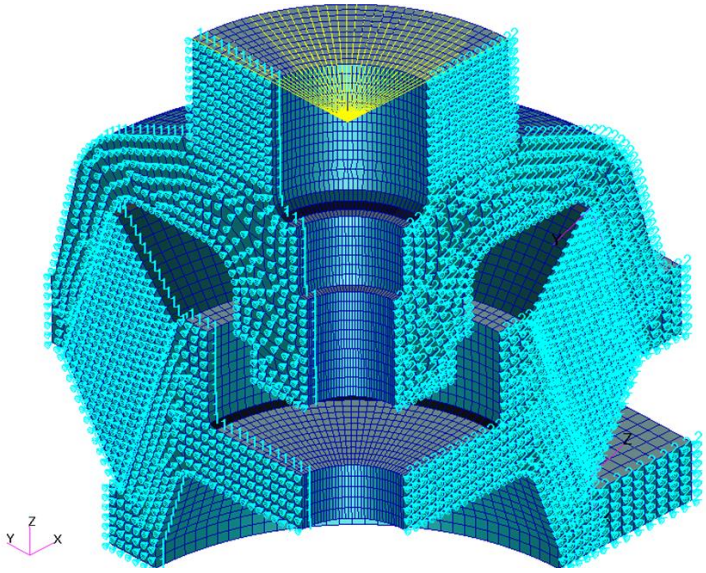

Figure 57: Isometric view of the RME quarter with boundary conditions under PATRAN

As the RME quarter model is concerned, the nodes located on the edges of the base drilling are clamped to represent the bolt fixation along the three directions (XYZ).

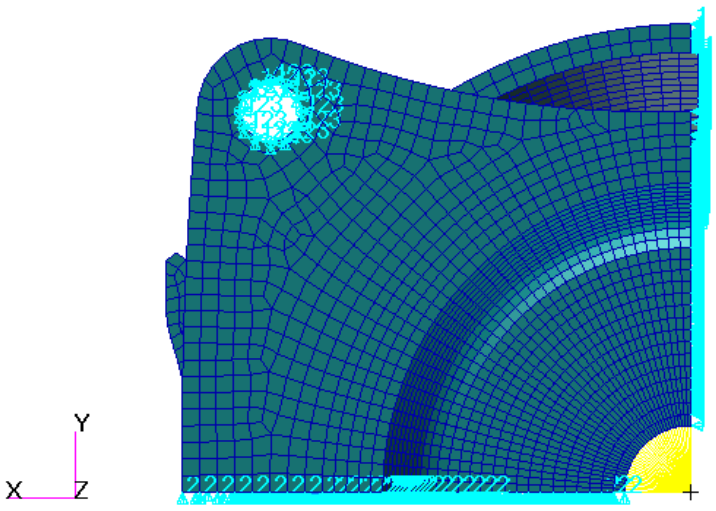

Figure 58: Bottom view of the RME quarter with boundary conditions under PATRAN

LS-DYNA explicit solver was used to perform the simulation. Thus, to avoid the occurrence of a shock when applying the load (abrupt variation of load), the input signal defined as a smoothed Heaviside step function with the amplitude of the working load applied on the nodes at the top of the T200.

c) Material law

The parts that constitute the RME top casting, intermediate rubber and the bottom support – have been associated to a specific element formulation and to a specific constitutive behaviour law. The top casting and bottom parts have been associated to a steel-like linear elastic behaviour law and to the "constant stress solid element" formulation. The intermediate part (rubber) is associated to a hyper-elastic behaviour law and the same "constant stress solid element" formulation.

The material used for non-rubber parts is a standard construction steel with the following characteristics (USI):

- Young modulus: 2.1^{E+11} Pa
- Poisson coefficient: 0.3
- Density : 7800 kg/m^3

The hyperelastic law formulated by Yeoh [51] allows to model the hyperelasticity of the rubber in LS-Dyna software. The different parameter values which have been used in our study are the following ones (SI), C_{10} , C_{20} and C_{30} being the so-called Yeoh coefficients. The coefficients are extracted from the precedent study on the RME [41]:

- Poisson coefficient: 0.49 (nearly incompressible material)
- Density: 1050 kg/m^3
- C_{10} : 1.000E+06 Pa
- C_{20} : 2571 Pa
- C_{30} : 1678 Pa

The other material law used to model the rubber is also a linear elastic law with the following mechanical characteristics (SI):

- Young modulus: 6.0E+06 Pa
- Poisson coefficient: 0.49
- Density: 1050 kg/m^3

When the solicitation is uniaxial and the considered material nearly incompressible ($\nu \approx 0{,}5$), the first Yeoh coefficient (C_{10}) of the hyper elastic law is related to the Young modulus of a linear elastic law (E) by the following expression, as it was introduced in part I.B.4:

$$C_{10} = \frac{E}{6} \qquad 157$$

These values should be confronted to the ones obtained from DMA tests. If there is a difference they will be updated for the dynamic analysis. A particular attention should be paid on the fact that Yeoh coefficients (C_{10}, C_{20}, C_{30}) may vary with the frequency. Unfortunately, LS-DYNA solver does not offer this possibility to account easily for this variation.

d) Contacts

The modelling of the contacts was a key feature of the numerical simulation. As it is displayed in Figure 56, the rubber material is in contact with the top casting and the base of the T200. At first, various attempts were undertaken with the integration of contact laws between the parts in several simulations. The contact laws were concerning the relation between the rubber part and the steel top casting, for one, and between the rubber part and the steel base, for the other. However, the results of those simulations were not satisfying primarily due to material penetration, which is not physically possible. Several methods were undertaken to solve this problem such as the local displacements of rubber part nodes to avoid the congruency nodes belonging to the steel top and base, but it didn't succeed. Therefore, it was not possible to post-process the results of these simulations. Then, the contacts laws were not integrated in the model. The nodes in the contact area of the steel base and rubber on one hand and the ones in the contact area of the rubber and steel top casting on the other hand were considered belonging to the two related parts (rubber part and steel base and rubber part and steel top).

2. Vertical deflections analysis results

The vertical deflection of the steel top casting under the working load applied to a RME quarter (divided by four) was firstly post-processed to verify the material consistency with the previous studies and the manufacturer data, and the thesis numerical model. The experimental test, which corresponds to this simulation led to a deflection of around 10 mm. Regarding the rubber material behaviour, two different models were built for these simulations: a first one based on the Yeoh hyperelastic law and the second one based on the Hook linear elastic law. **Error! Reference source not found.** displays the vertical deflection in meter.

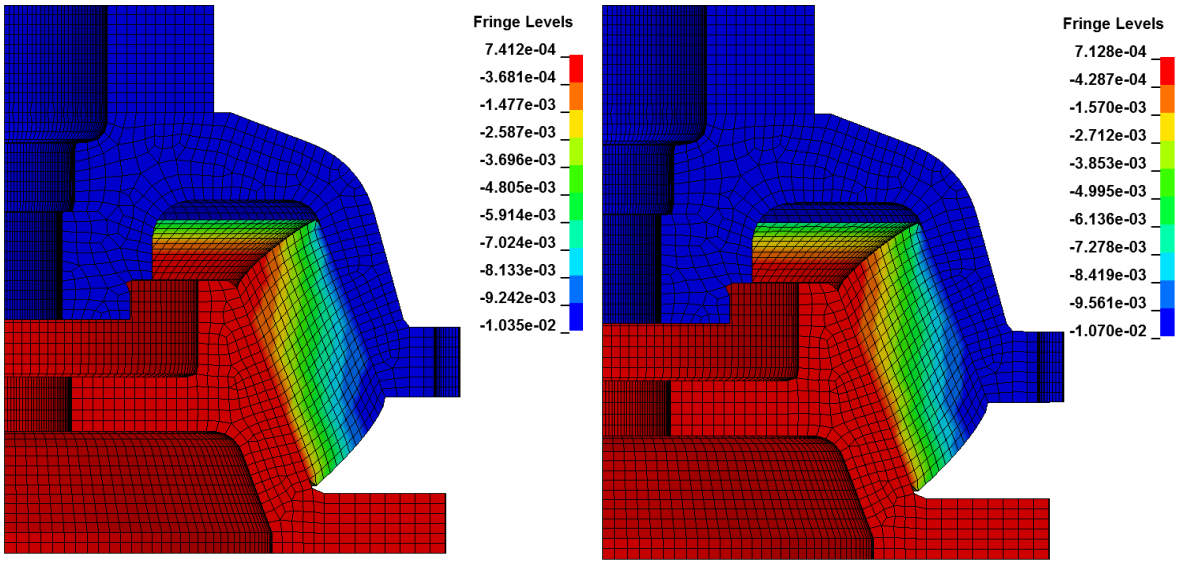

Figure 59: Vertical displacement (m) obtained using hyperelastic (left) and elastic law (right)

Whatever the used behaviour law (hyper-elastic or elastic), the resulting RME top casting deflection (10.35/10.7 mm) was very close to the provided data 10mm. The discrepancy between the deflection provided by the manufacturer and the deflections post-processed from numerical simulations was about 5.5%, which can be considered as acceptable. The discrepancy between the deflection levels obtained from the two numerical models was around 3.5%.

3. Rubber principal strain analysis

As it was previously introduced, the main objective of these preliminaries simulations was to determine the rubber 3D strain field, which was further used to set the dynamic mechanical analysis experimental initial parameters (static strain). These 3D field helped also to set for the DMA tests a strain working range, defined by the lowest and highest values of the deformation field,.

The 3D field was acquired by post-processing the rubber principal strains at the end of the quasi-static simulation, when the system is in equilibrium. The field continuity (no sudden variation in the field) of the strain field is a good way to evaluate the relevance of the simulation results. Figure 60 displays the 3D rubber principal strain field post-processed from both models.

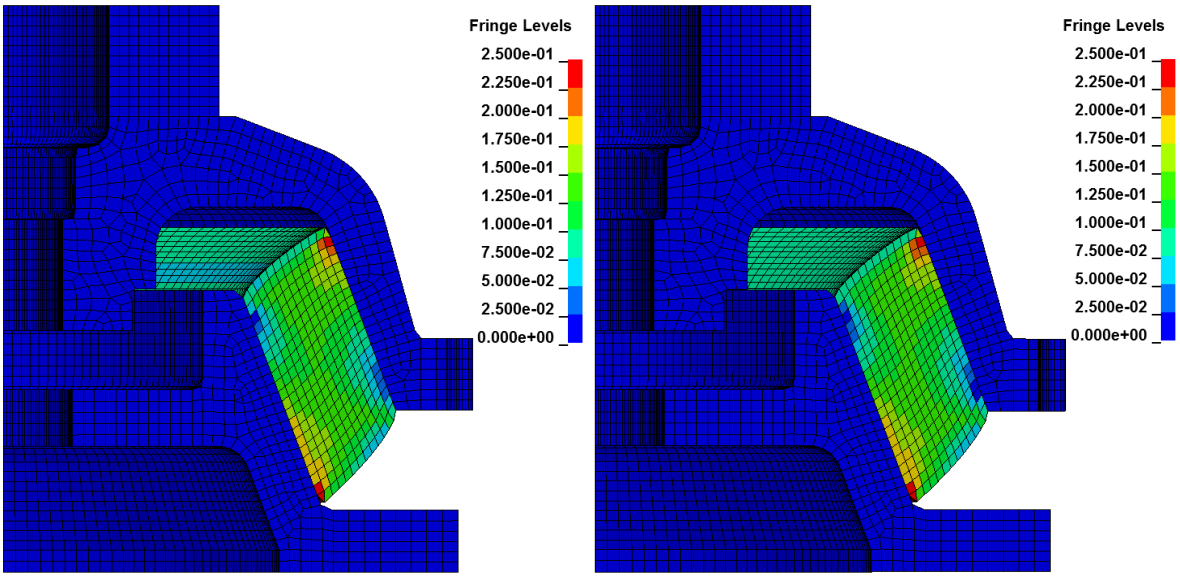

Figure 60: Maximum principal strains obtained using hyper elastic (left) and elastic law (right)

As the hyper-elastic model is concerned, the principal strain varied from 2.8 to 29.5%. As the linear elastic one is concerned, the principal strain varied from 2.8 to 31%

As mentioned before, a strain range of about [3-30%] was further used to set up the DMA tests performed on the rubber specimens. The resulting material characteristics were then used to define the updated Yeoh coefficients (hyperelastic law) and the Young modulus (linear elastic law).

A small statistical analysis was required to evaluate the discrepancy of the principal strains distribution in the two models and to ensure the practicability of the DMA experiments. Indeed the DMA test bench can only

generate one static strain on the tested rubber specimen. Therefore, the statistical analysis aimed to choose the static strain value to be reached before the DMA dynamic excitation.

Figure 61 displays the static strain distribution in the 3D strain field obtained in the model that is based on the linear elastic Hook law. Figure 62, as for it, displays the strain distribution obtained in the model based on the hyperelastic Yeoh model.

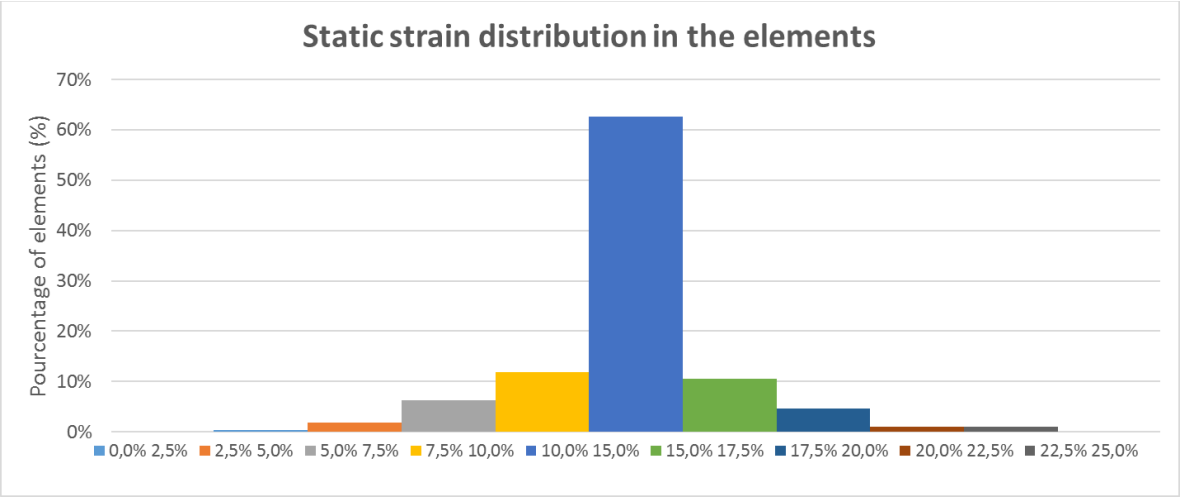

Figure 61: Strain static distribution of the rubber elements using the linear elastic law

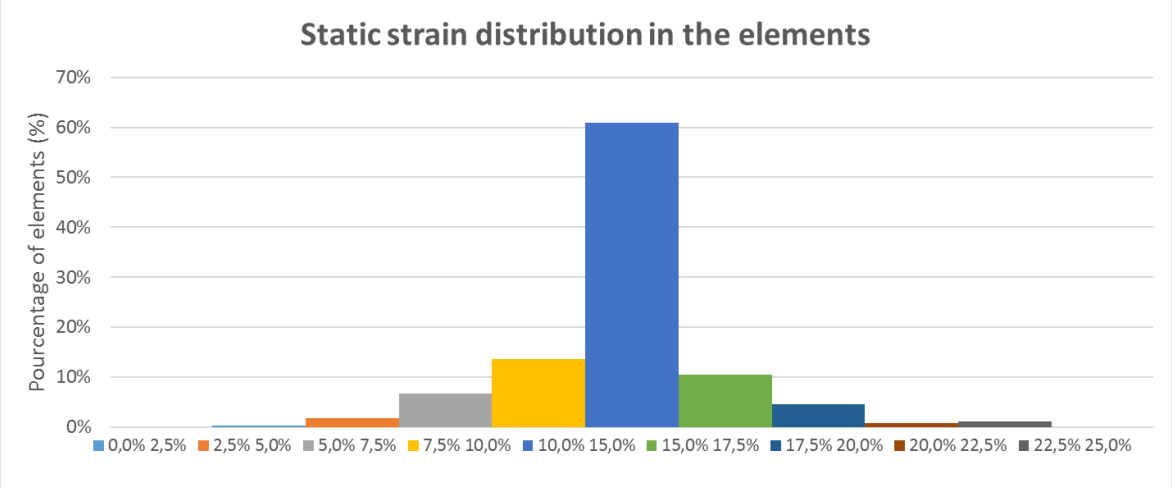

Figure 62: Strain static distribution of the rubber elements using the hyperelastic law

It is worth noting that the principal strain post-processed in most of the finite elements was found between 10 % and 15 %. The mean value of this interval (12.5%) was thus chosen to perform the DMA tests.

The discrepancy between hyper-elastic and elastic material model results did not exceed 5%. Therefore, the dynamic simulations were performed using the simplest behaviour law, i.e. the linear elastic one.

C. MODAL ANALYSIS OF THE RESILIENT MOUNTING ELEMENT

Finally, additional investigations were realized concerning the RME dynamic behaviour. Modal analyses were performed in parallel with static simulations. The principal aim of the RME modal analysis was to investigate the potential dynamic modal behaviour of the RME under testing, with the acquisition of the first RME natural frequencies and related mode shapes. In this case, the influence of the exciting mass should be taken into account. Indeed, the presence of this exciting mass at the top of the RME, when the experiment is performed, have an influence on the system dynamic behaviour (exciting mass and RME). The modal analysis cannot be completed on the RME under static pre-load (no consideration of the stiffening of the elastomer). As this compression leads to the stiffening of the elastomer, the first natural frequency should be higher than the one obtained with the uncompressed RME. Finally, modal analyses also allowed to compare the first natural frequencies calculated from the model based on the linear elastic law and from the model based on the hyperelastic one.

1. Finite element models

The finite element models (mesh, boundary conditions and material behaviour laws) are the same as previously presented, excepting a mass of about 93 kg which is added at the top of the RME. Of course, the compression forces are removed from the model for the normal mode analysis.

2. Results and comparison between both models.

The post-treatment of the modal analysis concerns only the first mode due to its critical potential influence on the dynamic measurements. Figure 63 shows the first normal mode post-processed from the model based on the hyperelastic law, while Figure 64 displays the same mode post-processed from the model based on the elastic law.

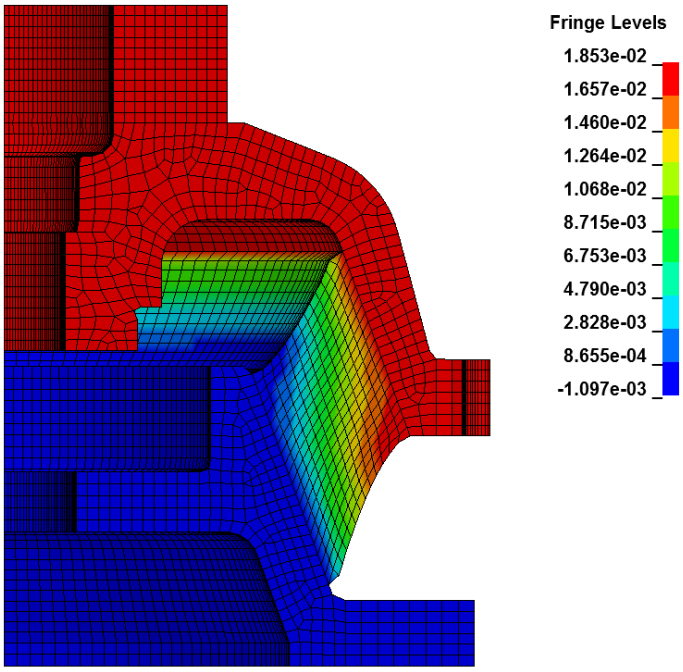

Figure 63: First RME natural mode shape at 37.059 Hz with the hyperelastic law

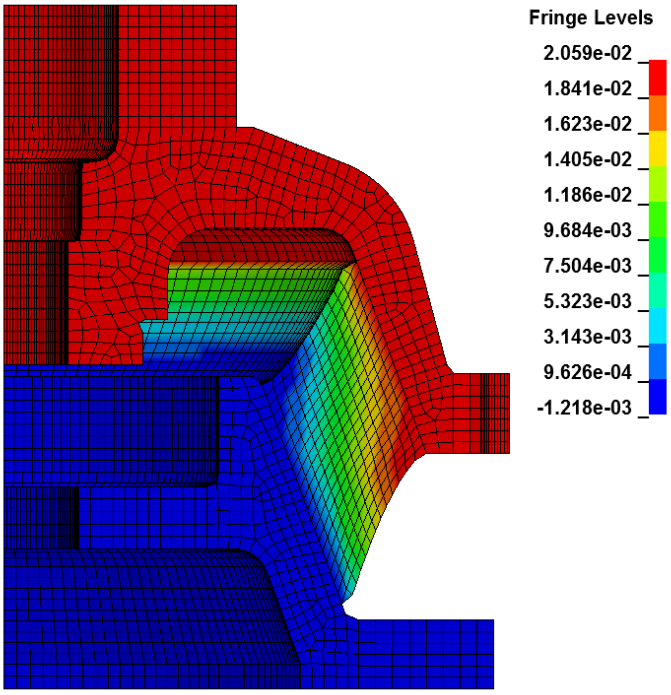

Figure 64: First RME natural mode shape at 37.053 Hz with the elastic law

As shown by figure above, the first mode is a vertical extension-compression mode at around 37 Hz. When the hyperelastic law is used to model the rubber behaviour, the first obtained natural frequency is at 37.059Hz. When the elastic law is used to model the rubber behaviour, the first obtained natural frequency is at 37.053 Hz. Referring to both natural frequencies of the two first modes, there is almost no difference between both models. In absolute terms, this mode could be excited during the dynamic tests, leading to serious disturbances in the measurements because 37.05 Hz actually lies in the frequency range planned for the experiment. However, the two models do not include the potential stiffening of the rubber after RME compression and the real natural frequency is expected to be higher than the calculated one.

In conclusion, a test rig was designed firstly to be used in a given frequency range. Then, static simulations were performed on the resilient mounting element (RME) using both elastic and hyperelastic material behaviour laws. Numerical results were further used to set up the parameters of the dynamic mechanical analysis (DMA) campaign. As small discrepancies were found between elastic and hyperelastic model results, it was decided to choose the Hook elastic law for frequency response simulations which will be presented further on. Moreover, dynamic modal analysis of the RME allowed to highlight the fact that during the experimental characterization, the tests should be carefully conduct from 37 Hz to 50 Hz due to the potential influence of the first RME vertical resonance mode.

III. RUBBER MATERIAL CHARACTERIZATION CAMPAIGN

After the determination of the 3D deformation field, it was possible to initiate the material characterization campaign. The statistical analysis performed on the resulting 3D deformation field provides a mean value of the deformations inside the rubber part. The campaign was conducted with the principal objective of an accurate and relatively exhaustive characterization of the T200 rubber. When a viscoelastic material is subjected to sinusoidal excitations, this characterization can be performed via a method called dynamic mechanical analysis (DMA), which was presented via its related ISO standard in section I.D.2. Therefore, the physical quantities, which are obtained via the DMA, are related to the material viscoelasticity characterizing the rubber behaviour. Although, the physical quantities depends on several environmental parameters, as discussed in section I.D.2, these physical quantities will only be expressed in function of the frequency excitation. The experimental campaign was performed at the LE2M laboratory of the Icam Nantes using a specific apparatus and procedure.

At first, the DMA preliminary works will be presented with the detailed objectives, the apparatus, the samples dimensioning, the followed procedure and the encountered issues. Then, the results of the DMA will be exposed and discussed.

A. DMA PRELIMINARY WORKS

1. Objectives

The main goal of this campaign is to characterize the rubber, which is used in the resilient mounting element. As discussed in section I.D.2, the physical quantities obtained with the DMA are the following material characteristics: the dynamic Young modulus and the loss factor or tangent angle loss. Considering that, the rubber is subjected to a static compression load and a dynamic excitation in the same direction, the rubber should be characterize in compression.

2. Apparatus

The experiment type was a characterization in compression a static pre-compression, with a dynamic excitation (sinusoidal signal), using parallel pans as samples holders. The description of the viscoanalyzer characteristics are presented in part I.C.2. This apparatus is controlled by a software that manage the DMA experiments. Figure 65 shows the apparatus called viscoanalyzer used for the DMA experiments. Figure 66, as for it, shows a rubber sample placed between two parallel pans.

Figure 65: Viscoanalyzer

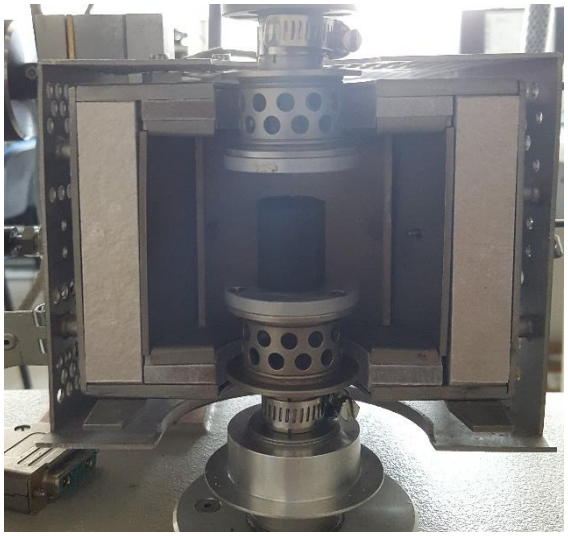

Figure 66: Parallel pans for compression tests

3. Sample design

Before initiating the DMA, it was necessary to have rubber samples that were representative of the rubber present in the tested T200 resilient mount. Due to the effect of the rubber aging on the material properties, the tested rubber should had the same age. Furthermore, because of the unknown date of the T200 rubber manufacturing, it was nearly impossible to acquire a rubber of the same age. Therefore, the best technique was to acquire the samples from the rubber part itself.

a) Origin of the samples

The DMA used samples were extracted from the rubber part of the resilient mounting element T200. At first, long rubber rod were wangled. Then the samples were cut at the right dimensions as presented in Figure 67.

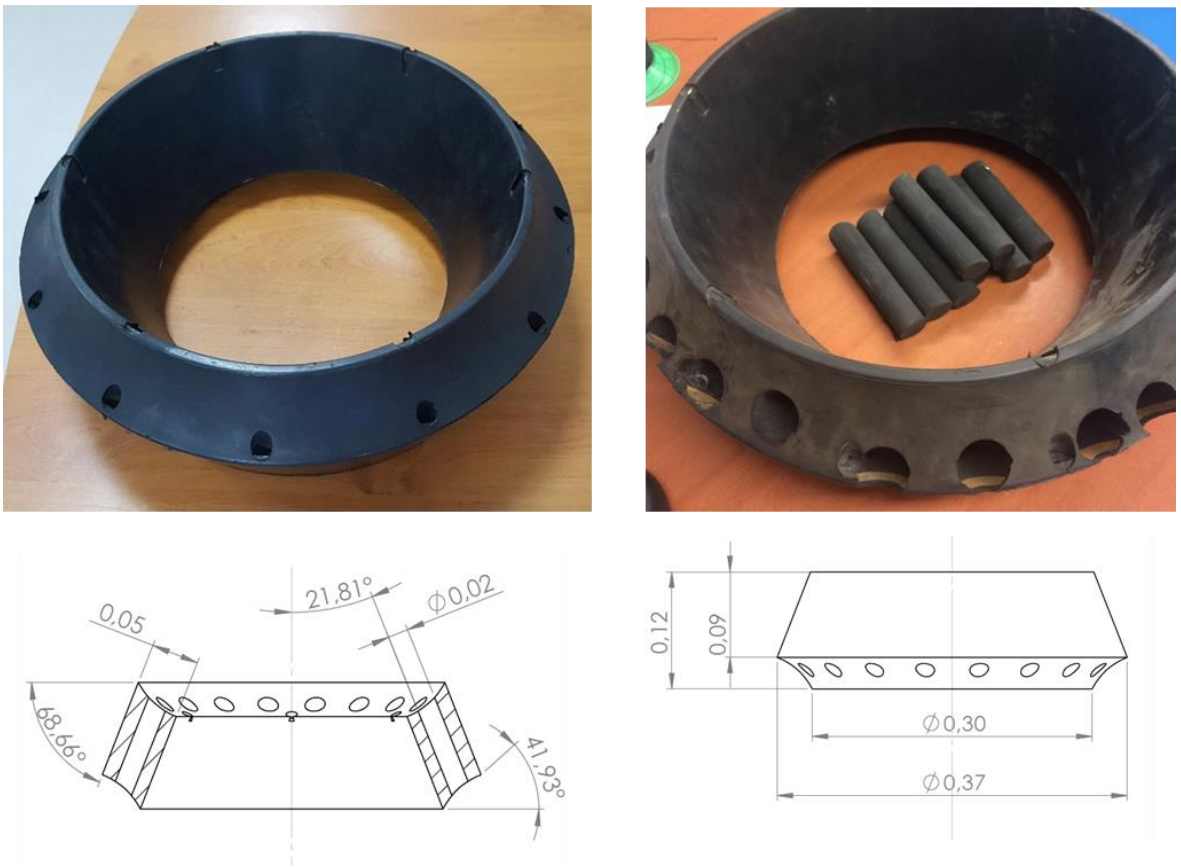

Figure 67: T200 rubber part with wangle sampled and related dimensioning drawings

To study the effect of the cutting on the rubber sample geometry, several cutting tests were firstly realized at l'Icam Nantes. Due to the incompressibility of the rubber, the rubber cutting led to problems concerning the sample shapes. Therefore, after this feedback, it was decided to let the cutting at the expense of a company specialized in the cutting of elastomeric material. This company advised to use waterjet cutting to created the rubber sample. However, the waterjet cutting, with the chosen wangling length, induced high diameter reduction through the sample (1 to 2 mm of reduction).

The dimensioning of the samples (cylinders) is explain in section I.D.2.b. Therefore, the dimensions of the rubber samples respected the specifications concerning both form factors.

b) Final samples presentation

Due to the rubber intrinsic heterogeneities coming from the manufacturing process, several samples were created to minimize the DMA results dispersion. Respecting the recommendations of the standard concerning the dimensions of the sample, the tested samples are presented below with their geometrical specificities:

- 15 samples of 25 mm height and 20 mm of diameter
- 10 samples of 12.5 mm height and 10 mm of diameter

Figure 68 shows the sample of 25mm height.

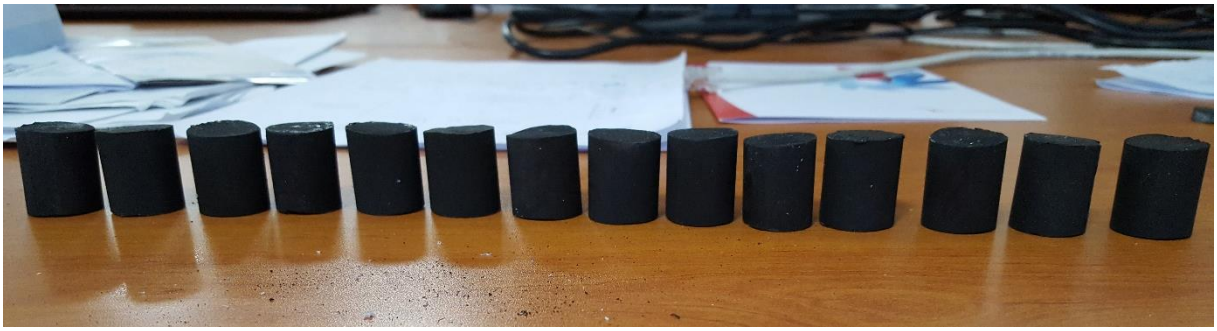

Figure 68: Samples of 25 mm height

It was noticed that these rubber samples were not perfect cylinders. For several samples, their top and bottom sections were not parallel.

Figure 69 shows the sample of 12.5mm height.

Figure 69: Samples of 12.5 mm height

It was noticed that, as for the 25 mm height samples, these samples were not perfect cylinders with the same issue about the parallelism. Furthermore, a cylindricity issue emerged as it is shown in Figure 69.

The 12.5 mm height samples were created from the 20mm diameter wangles. Those wangles were cut to obtain the 12.5 mm height. Then the samples were deep drawn to obtain the right diameter. These samples was produced due to the difficulty of the viscoanalyzer to reach 12.5 % of deformation during the experiment of the 25 mm height samples.

4. Procedure

A small procedure present in the technical data of the viscoanalyzer and the software should be respected to obtained valid results according to the standard. Figure 70 displays the procedure.

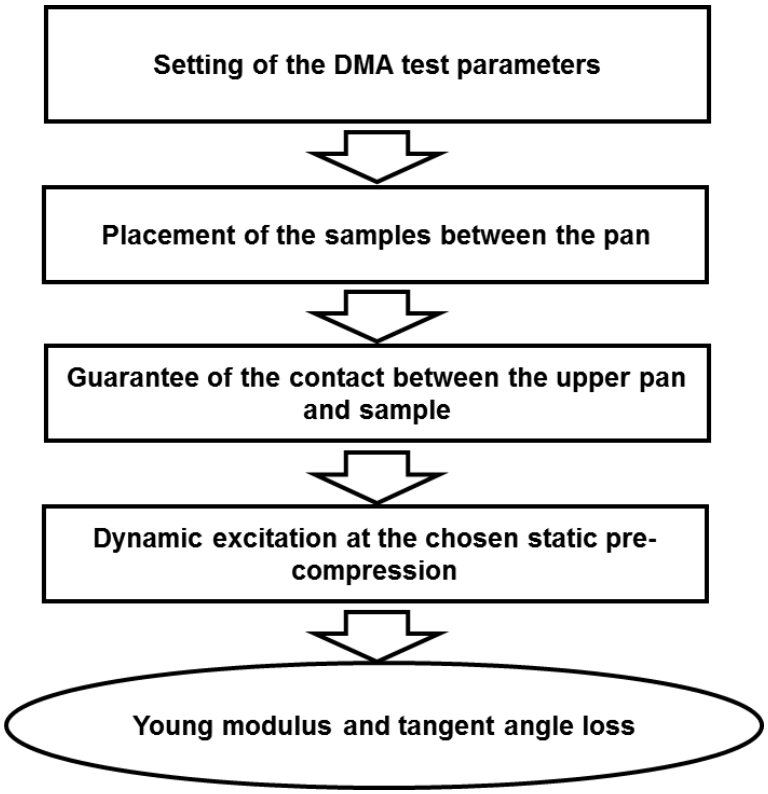

Figure 70: DMA test bench procedure

At first, the test parameters needed to be indicated in the software. The test parameters were composed by the sample dimensions, frequency range, static and dynamic amplitude. Then, the sample was be positioned between the pans. The characterization method of the DMA bench is similar to the direct method presented in section I.D.1. Indeed, the rubber dynamic stiffness was acquired using a force transducer below the lower pan and a displacement sensor place at the top of the upper pan. In fact, a vertical dynamic excitation was applied on the rubber sample via a pneumatic dynamic exciter connected to the upper pan. To ensure the good application of the dynamic excitation, a complete contact between the upper pan and the top section of the sample needed to be ensured. Then, the dynamic excitation, and, by extension, DMA experiment, were initited. Finally, the complex Young modulus and tangent angle loss was acquired.

5. Met issues

As for many experimental studies, several issues were encountered during this campaign. The main issues were related to the dimensioning of the samples and leading to disturbances in the measured data.

As it was specified previously, the contact between the upper pan and the sample top section and, between the lower pan and sample lower section needed to be verified. It supposed a perfect parallelism between the fourth surfaces. However, as it was also previously mentioned, the geometrical specifications concerning the parallelism were not respected for several samples. To rectify this issue, adhesive tape was used to bond the rubber to the higher and lower pan. An additional pre-compression of a few hundred micrometres was also performed to ensure the contacts.

Figure 71 shows the contact issue for a sample of 25 mm of height.

Figure 71: Contact issue for the sample

Another issue emerged with the 12.5 mm height sample. The cylindricity issue of these samples induced a post-treatment problem with the software. Indeed, for the calculation of the Young modulus from the acquired stiffness, the dimensions of the sample that needed to be indicated were the cylinder section and sample height. The sample respective heights were not considered as a problem. However, the no-respect of the cylindricity was a serious issue at first sight. Nevertheless, in a case of compression, it is possible to consider each sample minimum section in order to calculate the Young modulus.

Figure 72 shows the cylindricity issue for a sample of 12.5 mm of height.

Figure 72 : Non-cylindrical rubber sample

Those issues were considered in the result post-treatment and could explained the dispersion of the results.

B. DYNAMIC MECHANICAL ANALYSIS OF THE RUBBER MATERIAL OF THE T200

After the required preliminary work, the DMA experiments were initiated. Each rubber sample were characterize in frequency separately. Then, the results data were collected and compiled. This compilation provided an average curve of the Young modulus and an average curve of the tangent angle-loss in function of the frequency. Then, a small investigation about the influence of the amplitudes (dynamic and static) was accomplished. This investigation helped to evaluate the linearity of the rubber material behaviour. Finally, the DMA results relevancy will be discussed. Furthermore some calculations to estimate the viscous damping of the system will be presented.

1. Experiment setting

Before presenting the results, the experiment settings had to be exhaustively described. For each sample characterization, one experiment was performed. In the software, for each experiment, the dimensions was provided at first. Then, the frequency range was set with the required dynamic amplitude and static compression amplitude. The first experimental configuration can be presented as follows:

- Dynamic amplitude: $1.0x10^{-2}$ of deformation
- Frequency range: from 1 Hz to 50Hz with 99 measurement points using the HF frequency sensor
- Static amplitude (compression): $-1.25x10^{-1}$ of deformation

Furthermore, to investigate the influence of the amplitudes (dynamic and static), other experiments were performed with other amplitude values. However, each influence was studied separately. Indeed, when the variation study focused on one amplitude, the other was fixed to the value of the first configuration. In this investigation, the static amplitude variation is from $5.0x10^{-2}$ to $1.25x10^{-1}$ of deformation. The dynamic amplitude variation, as for it, is from $5.0x10^{-3}$ to $3.0x10^{-2}$ of deformation. The sweep in frequency is the same as in the first configuration.

2. Results

Considering that it was not possible to reach the wanted static pre-deformation (12.5%) with the 25 mm height samples (only 6%), the only presented results are the 12.5 mm height samples results.

The data post-treatment is realized in three steps, as follows:

1. Results compilation (Young modulus, tangent loss angle) of the 10 trials for the acquisition of mean value
2. Curves creation of the Young modulus and tangent loss angle in function of the frequency and deformation (static and dynamic), for the variation study.
3. Statistical analysis of the results with the representation of the ratio between the standard deviation and the mean, the coefficient of variation for each frequency
4. Statistical representation of results through frequency

For an analysis of the results relevancy, it is only possible to evaluate the dispersion of the 12.5mm height samples results. The following graphics display, at first, the value of the parameters for each sample. Furthermore, to analyse the distribution of the results, the standard deviation (σ) was calculated at each frequency and the coefficient of variation expressed in function of the frequency. To evaluate the dispersion of the results, it is possible to verify the three-sigma rule, better known as the "***68–95–99.7***" rule.

Then they display the mean value of each parameters (Young modulus and tangent angle loss) through frequency for all experimental configurations. The graphics also include the curves that represent the maximum and minimum values for each frequency. They also include the "mean ± 2 σ" curves that figure the statistic distribution of the results. The first assumption lead to consider the experimental results as "good" if the minimum and maximum curves are between the "median ± 2 σ" curves.

Then, the influences of the static and dynamic amplitude are investigated.

a) Sweep in frequency with fixed static and dynamic deformation

In this section, the post-treated results of the first configuration are presented, with, at first, the Young modulus and after the tangent angle loss of each sample. The associated coefficient of variation and statistical representation are also presented.

- Young modulus

Figure 73 displays the Young modulus in function of the frequency for each sample.

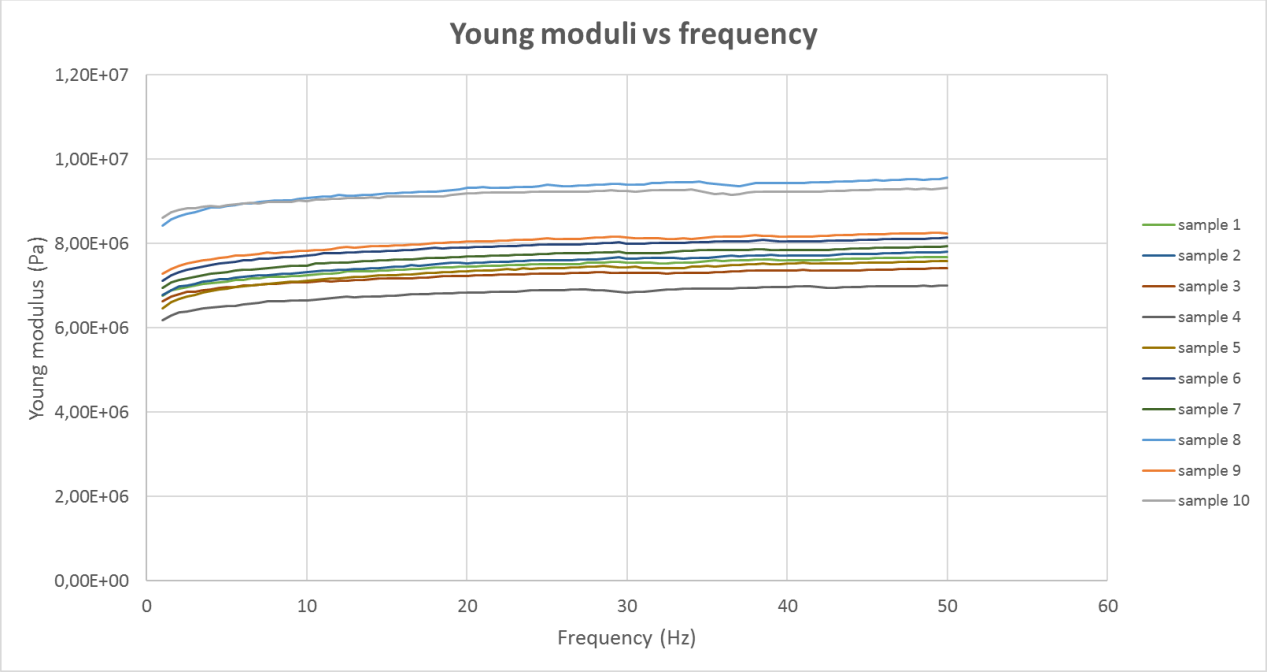

Figure 73: Results dispersion for the 10 samples of 12.5 mm height

Figure 74 displays the coefficient of variation in function of the frequency.

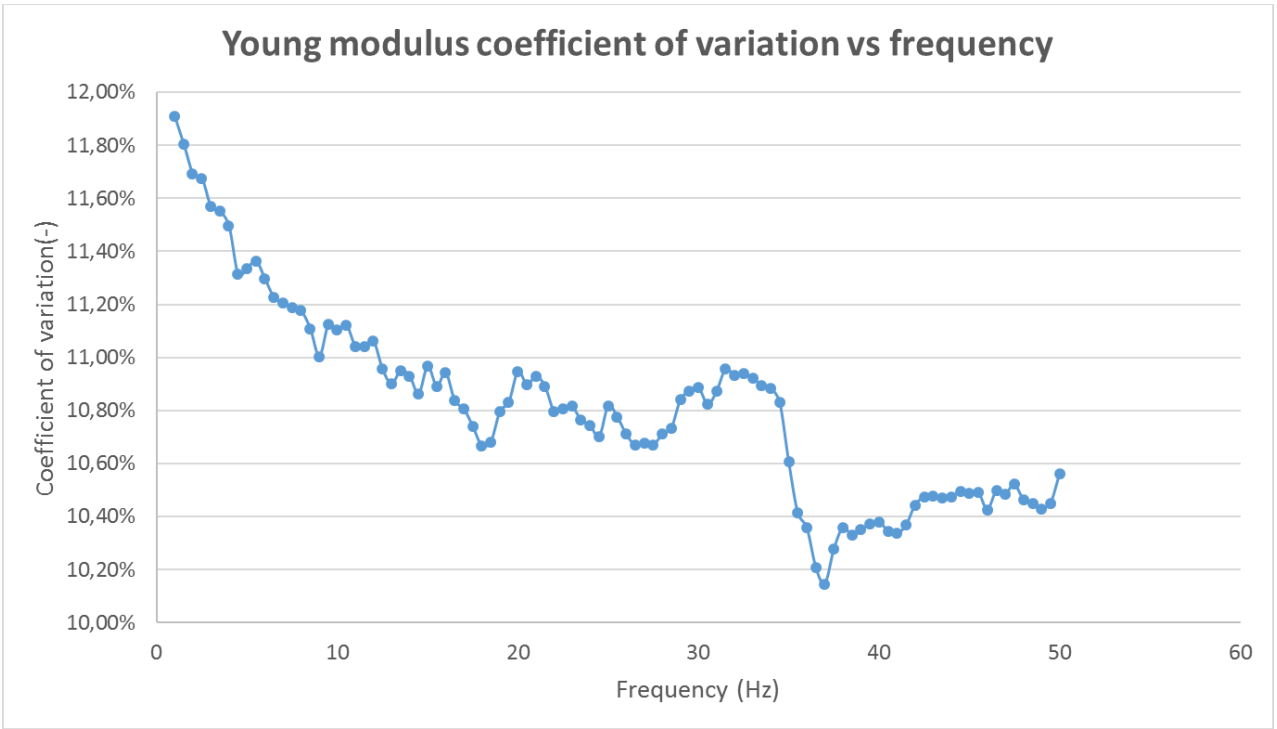

Figure 74: Coefficient of variation for the 10 samples of 12.5 mm height

Figure 75 displays the statistical analysis of the Young modulus in function of the frequency.

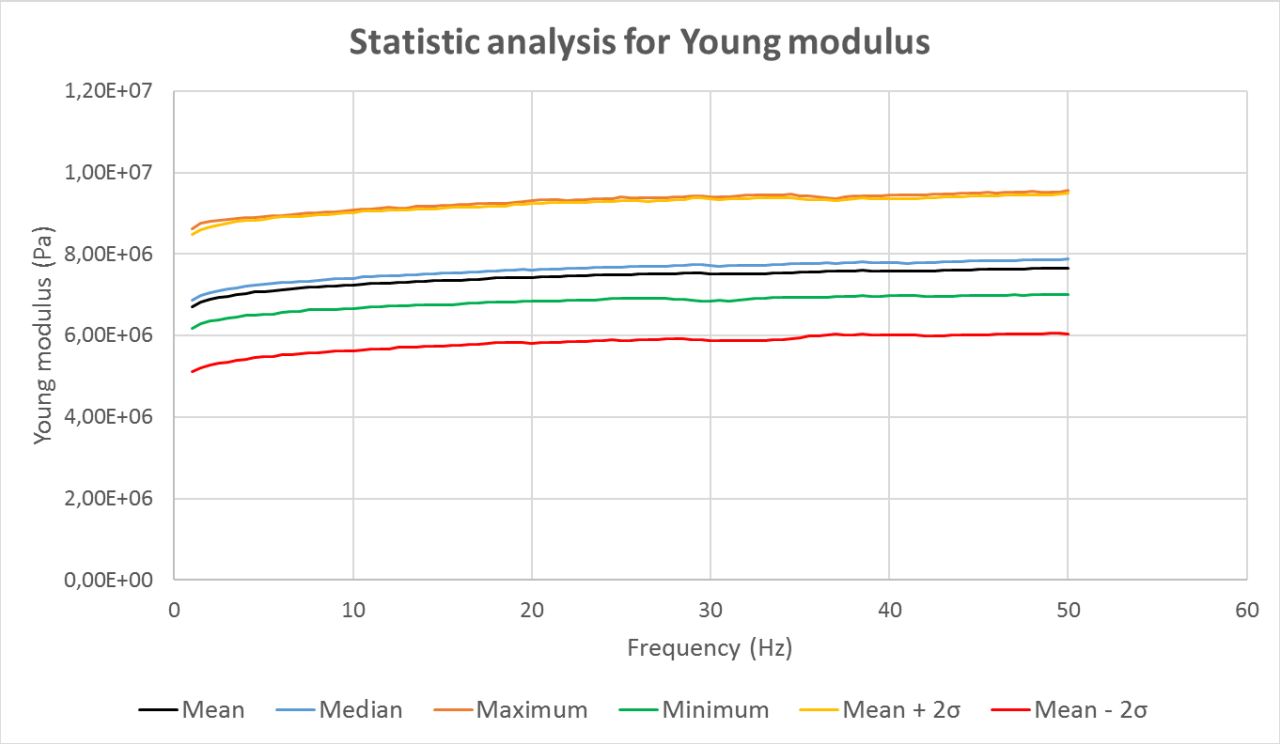

Figure 75: Synthetic description of the results for the Young modulus

Concerning the sample curves, it can be noticed that, at the exception of two, the curves are quite grouped. Furthermore, the evolution of the coefficient of variation shows that the dispersion of the results does not depend significantly on the frequency. Moreover, the statistical analysis reveals that maximum and minimum curves are in the interval [Mean - 2 σ; Mean + 2 σ], leading to consider the distribution as a normal distribution. Therefore, the dispersion could be considered relatively low for the first experiment configuration.

- Tangent angle loss

Figure 76 displays the tangent angle loss in function of the frequency for each sample.

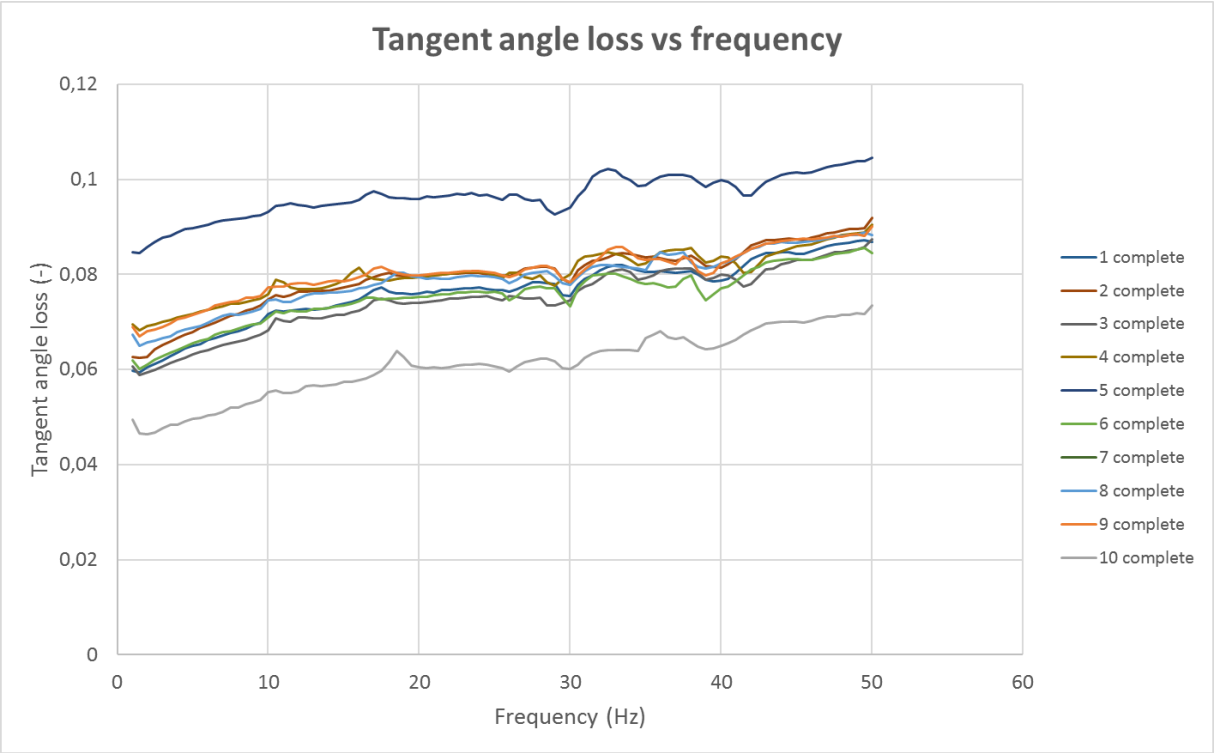

Figure 76 : Results dispersion for the 10 samples of 12.5 mm height

Figure 77 displays the coefficient of variation in function of the frequency.

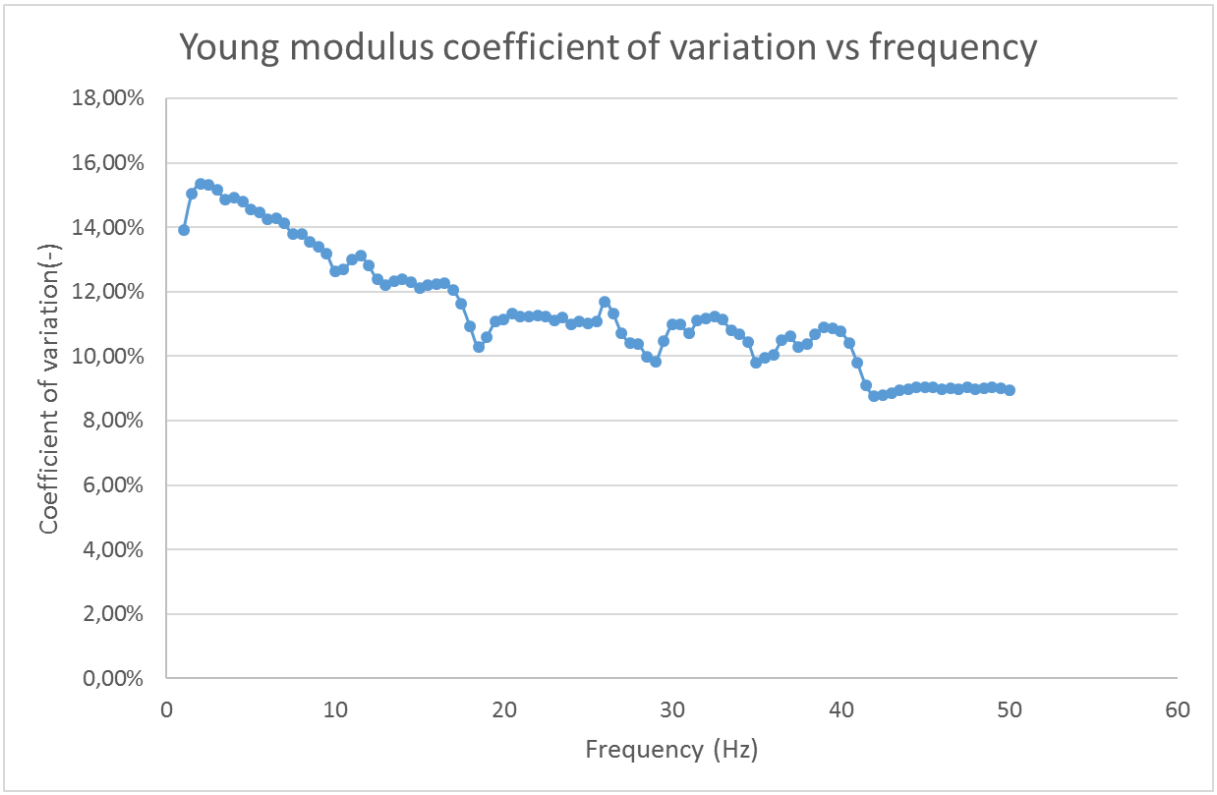

Figure 77: Coefficient of variation for the 10 samples of 12.5 mm height

Figure 78 displays the statistical analysis of the tangent angle loss in function of the frequency.

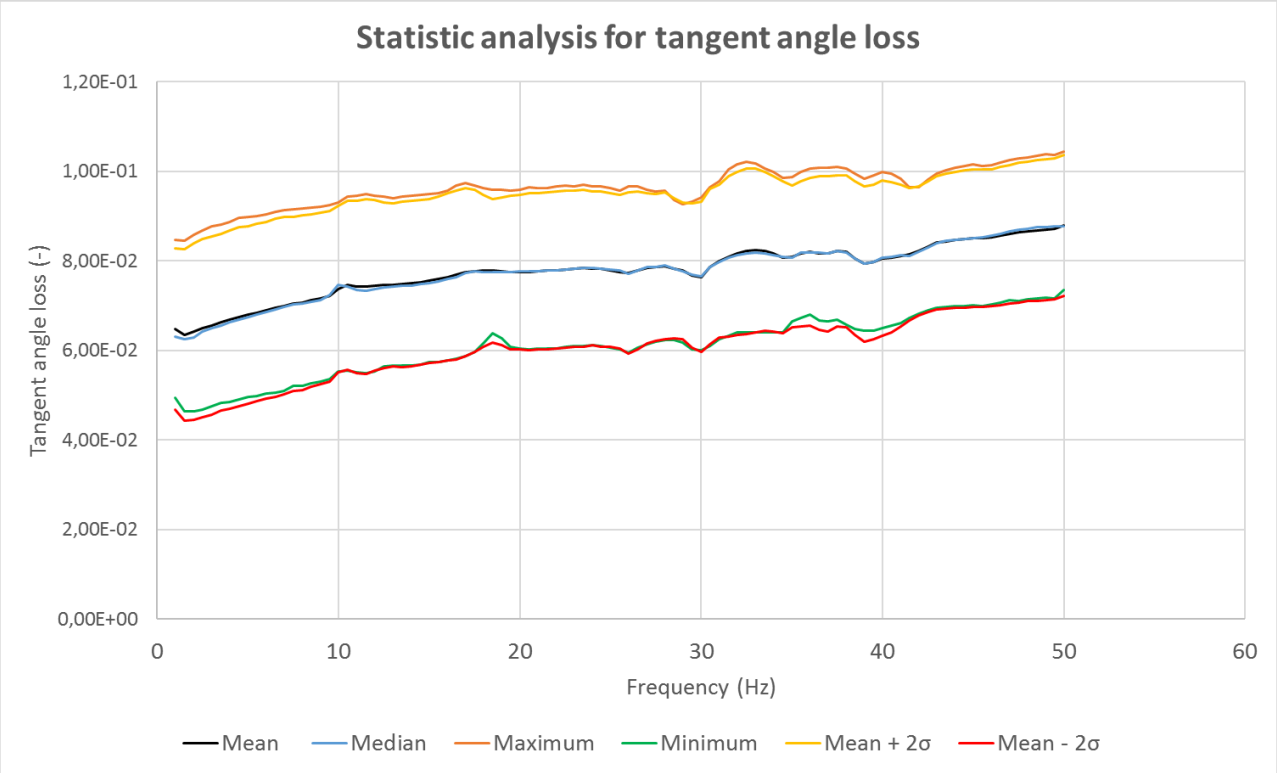

Figure 78: Synthetic description of the results for the tangent angle loss

Concerning the sample curves, it can be noticed that, at the exception of two, the curves are also quite grouped. Furthermore, the evolution of the coefficient of variation shows that the dispersion of the results does not depend significantly on the frequency. Moreover, the statistic analysis reveals that maximum and minimum curves are almost in the interval [Mean - 2 σ; Mean + 2 σ], leading to consider the distribution as a normal distribution. Therefore, the dispersion could be considered relatively low for the first experiment configuration.

b) Sweep in frequency and static deformation with fixed dynamic deformation

In this section, the post-treated results of the static deformation amplitude sweep are presented, with, at first, the Young modulus and after the tangent angle loss of each sample. The associated coefficient of variation and statistical representation are also presented.

- Mean Young modulus

Figure 79 displays the evolution of the mean Young modulus in function of the frequency for some values of static amplitude. Figure 80, as for it, displays the evolution of the mean Young modulus in function of the static amplitude for some values of frequency.

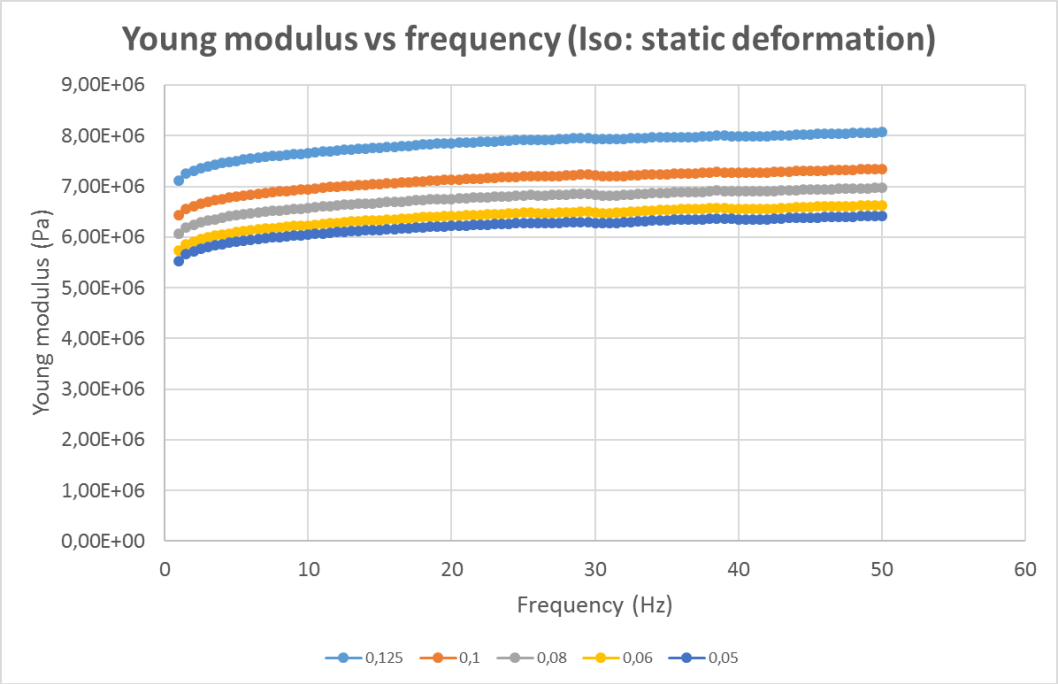

Figure 79: Young modulus evolution with frequency (ISO static deformation)

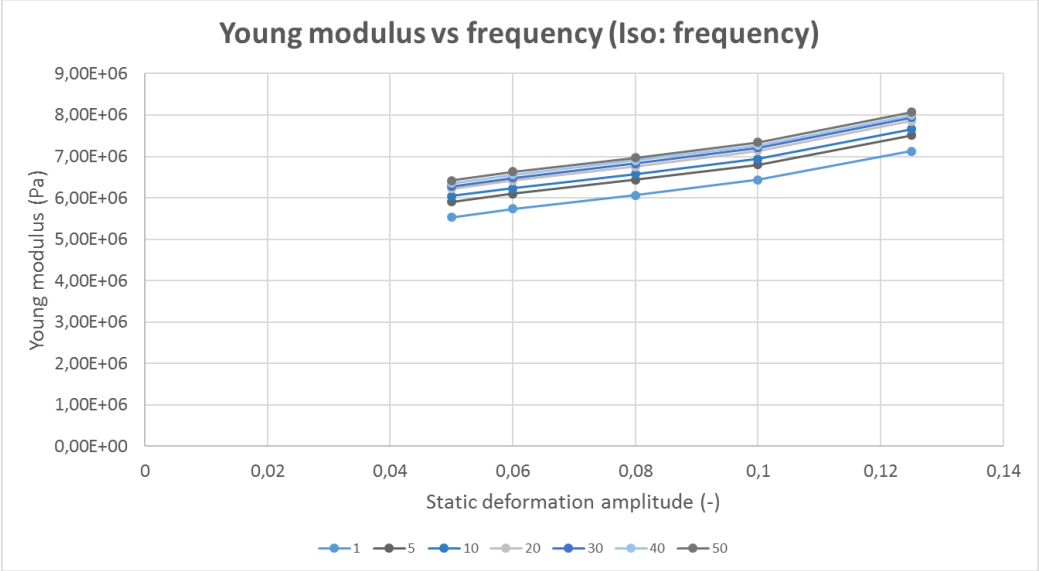

Figure 80: Young modulus evolution with static deformation (ISO: frequency)

- Mean tangent angle loss

Figure 81 displays the evolution of the mean tangent angle loss in function of the frequency for some values of static amplitude. Figure 82, as for it, displays the evolution of the mean tangent angle loss in function of the static amplitude for some values of frequency.

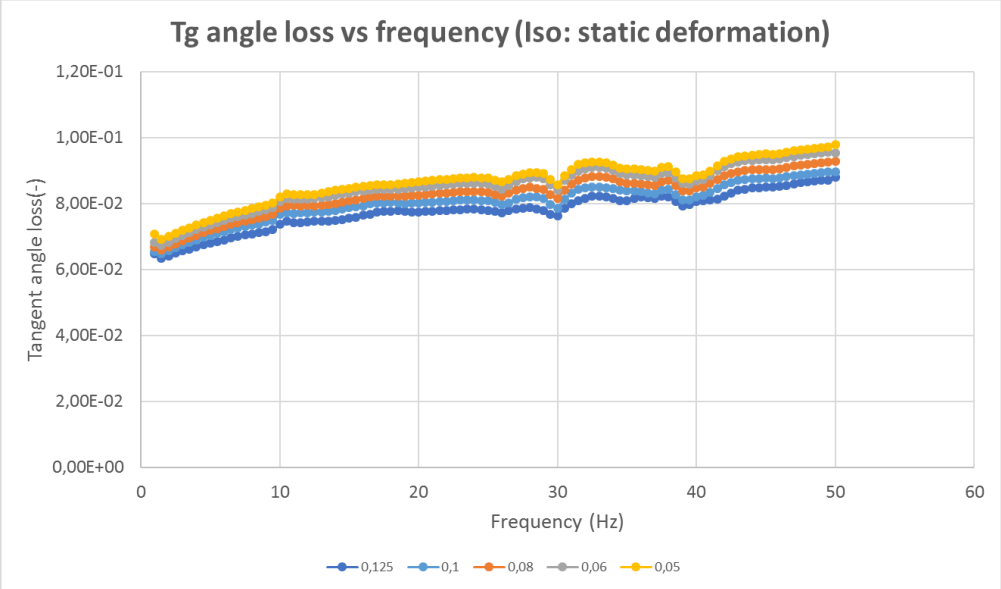

Figure 81: Tangent angle loss evolution with frequency (ISO static deformation)

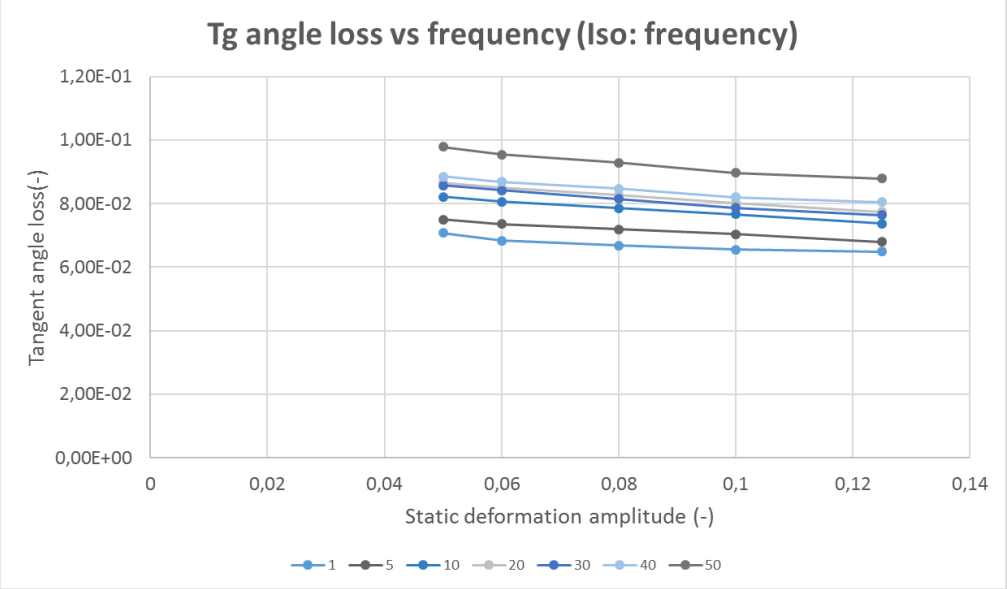

Figure 82: Tangent angle loss evolution with static deformation (ISO frequency)

Concerning the investigations on the static amplitude influence, it can be noticed that the Young modulus increases in function of the frequency and increases when the static compression amplitude increases. The tangent angle loss, as for it, increases in function of the frequency but decreases when the static compression amplitude increases. Regarding the Young modulus, the features developed in section I.B.4.b and I.B.4.c could explain those increases. For the elastomeric materials, the Young modulus should increase when the frequency and static compression increases. Regarding the tangent angle loss, it is difficult evaluate the coherence of the results. As it was discussed in section I.B.4.b., it is difficult to establish a global trend regarding the evolution of the tangent angle loss in function of the frequency and compression amplitude.

c) Sweep in frequency and dynamic deformation with fixed static deformation

In this section, the post-treated results of the dynamic deformation amplitude sweep are presented, with, at first, the Young modulus and after the tangent angle loss of each sample. The associated coefficient of variation and statistical representation are also presented.

- Mean Young modulus

Figure 83 displays the evolution of the mean Young modulus in function of the frequency for some values of dynamic amplitude. Figure 84, as for it, displays the evolution of the mean Young modulus in function of the dynamic amplitude for some values of frequency.

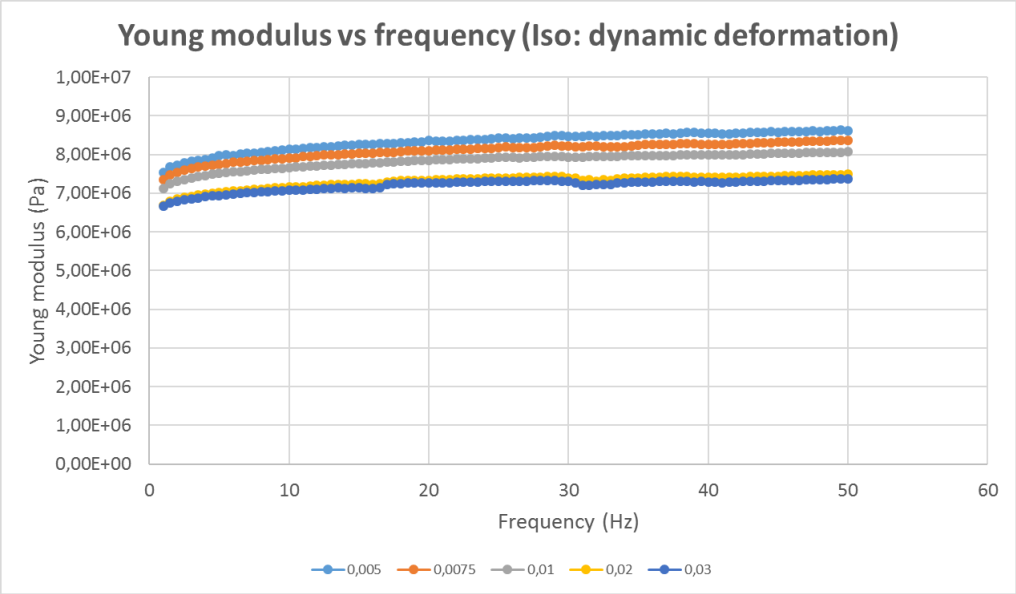

Figure 83: Young modulus evolution with frequency (ISO dynamic deformation)

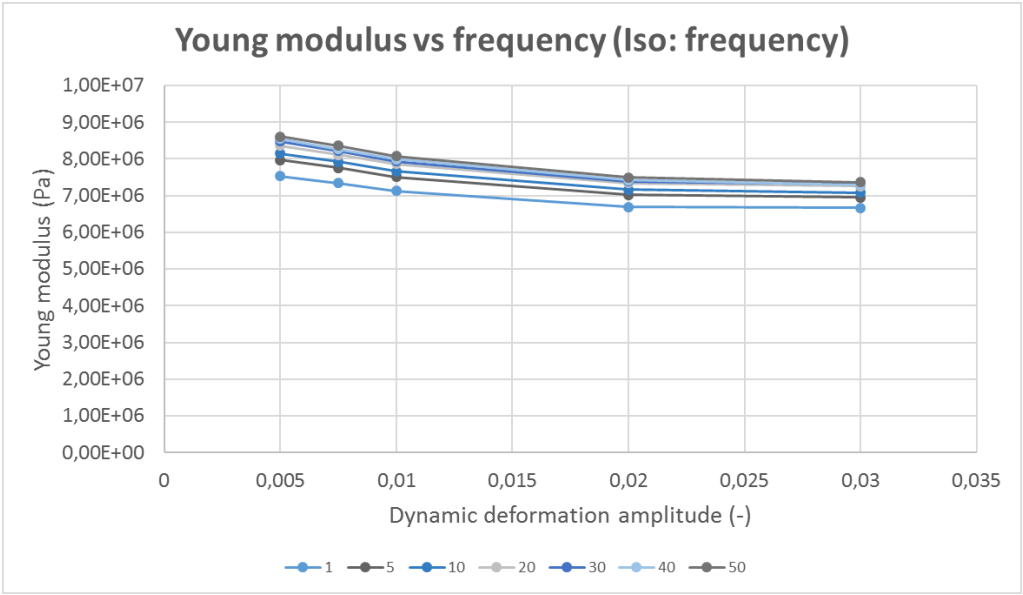

Figure 84: Young modulus evolution with dynamic deformation (ISO frequency)

- Mean tangent angle loss

Figure 83 displays the evolution of the mean tangent angle loss in function of the frequency for some values of dynamic amplitude. Figure 84, as for it, displays the evolution of the mean tangent angle loss in function of the dynamic amplitude for some values of frequency.

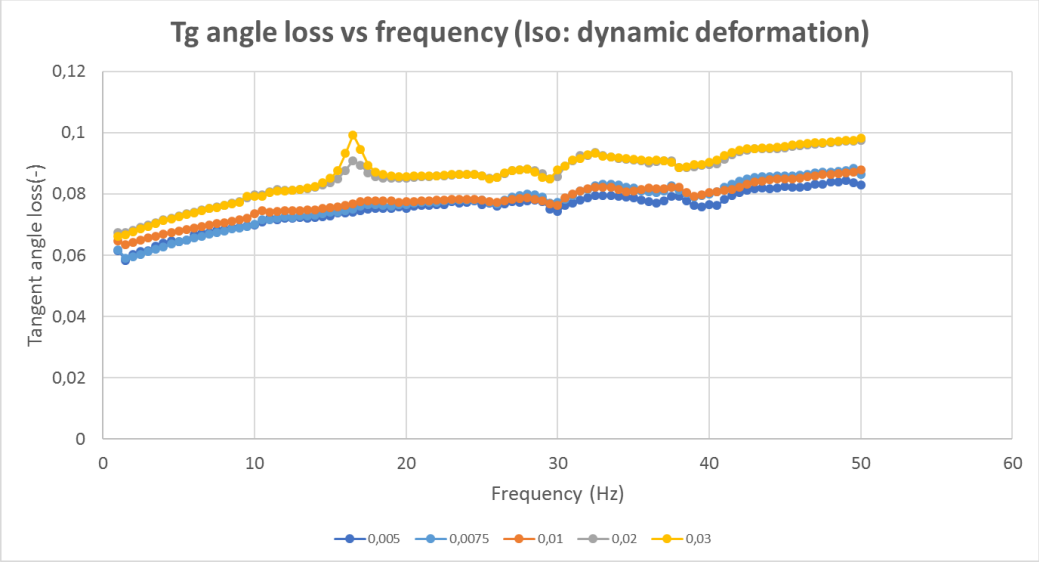

Figure 85: Tangent angle loss evolution with frequency (ISO dynamic deformation)

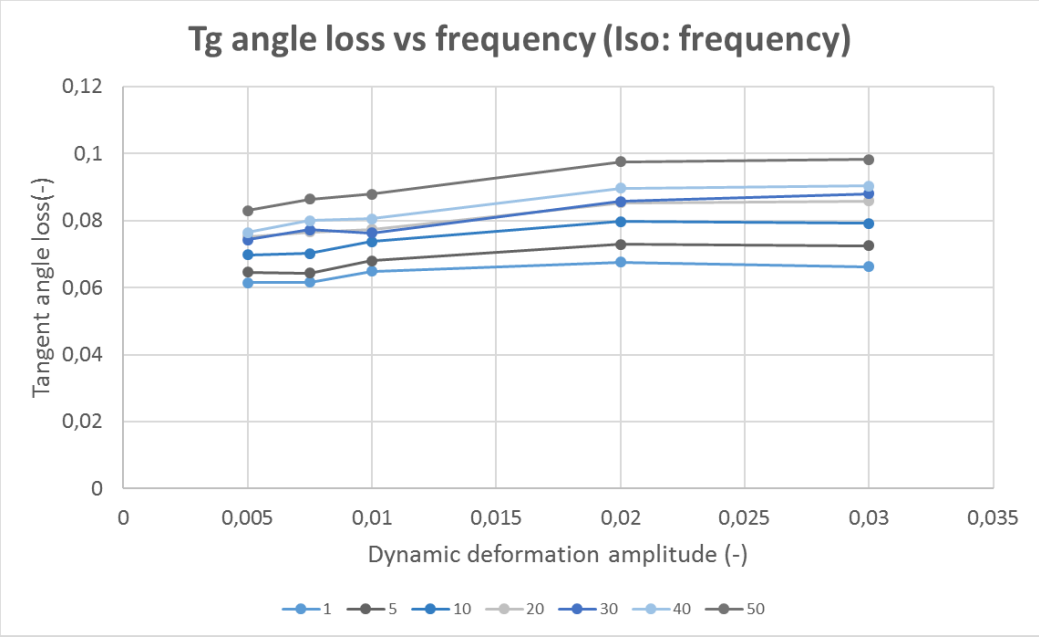

Figure 86: Tangent angle loss with dynamic deformation (ISO frequency)

Concerning the investigations on the dynamic amplitude influence, it can be noticed that the Young modulus increases in function of frequency but decreases when the dynamic amplitude increases. The tangent angle loss, as for it, increases in function of the frequency and increases when the dynamic amplitude increases. Regarding the Young modulus and tangent angle loss, it is difficult to explain their evolution in function of the dynamic excitation amplitude due to the lack of investigations in the bibliography concerning this subject.

3. Results conclusion

At first, even if the quality of the tested rubber samples was unsatisfying due to geometrical issues, the results could be considered satisfactory as the results dispersion of both material characteristics is low. Thus, with the DMA results, it is possible to update the rubber law parameters for the numerical DTS determination or for a potential analytical model. It is worthy noticeable that both parameters are increasing through frequency. Then the parameters should be defined depending on the excitation frequency. This could lead to an issue if the software does not give the possibility to express the parameters in function of the frequency.

It is also possible to obtain the viscous damping of the system at the resonance frequency with its related normal mode using the following formula:

$$c = \tan(\delta) \times m \times \omega_{res} \quad (158)$$

where c is the viscous damping, $\tan(\delta)$ the structural damping at the resonance frequency, m the system mass, and ω_{res} the resonance pulsation of the normal mode.

In fact, as the structural damping is known from the previous results. The mass and resonance pulsation could be gathered from the normal mode analysis in part II.C, where the studied mode is a vertical translation. Thus, the related mass is equal to 93 kg and the resonance frequency to 37 Hz.

In consequence, with the lowest tangent angle loss value (0.08), it gives:

$$c = 0.08 \times 93 \times 2 \times \pi \times 37 \quad (159)$$

$$c \cong 1730\ N.s/m \quad (160)$$

With the mean value (0.925), it gives:

$$c = 0.0925 \times 93 \times 2 \times \pi \times 37 \quad (161)$$

$$c \cong 2000\ N.s/m \quad (162)$$

With the maximum (0.11), it gives:

$$c = 0.11 \times 93 \times 2 \times \pi \times 37 \quad (163)$$

$$c \cong 2370\ N.s/m \quad (164)$$

In addition, this viscous damping could be used to define a viscous damper in the vertical direction in order to model the damping of the system.

IV. EXPERIMENTAL CAMPAIGN

After the design of the test rig according to the ISO 10846 concerning crucial prescriptions related to the structure dimensioning, it was possible to accomplish the experimental campaign. The experimental campaign was realized with the principal objective of an accurate dynamic characterization of the resilient mounting element in the frequency domain. This characterization relies mainly on the vertical complex dynamic transfer stiffness (DTS) determination of the tested resilient mounting. The complex DTS will be expressed using two components: the magnitude and the tangent angle loss as it was displayed in part II.A. To ensure the accuracy of the DTS, the campaign was accomplished respecting the ISO 10846-2 specifications regarding the quality of the measurements. The experimental campaign was performed at the Ship Noise and Vibration Laboratory (NVL) of the University of Trieste using the aforementioned test rig. Figure 87 displays the RME installed on the test rig.

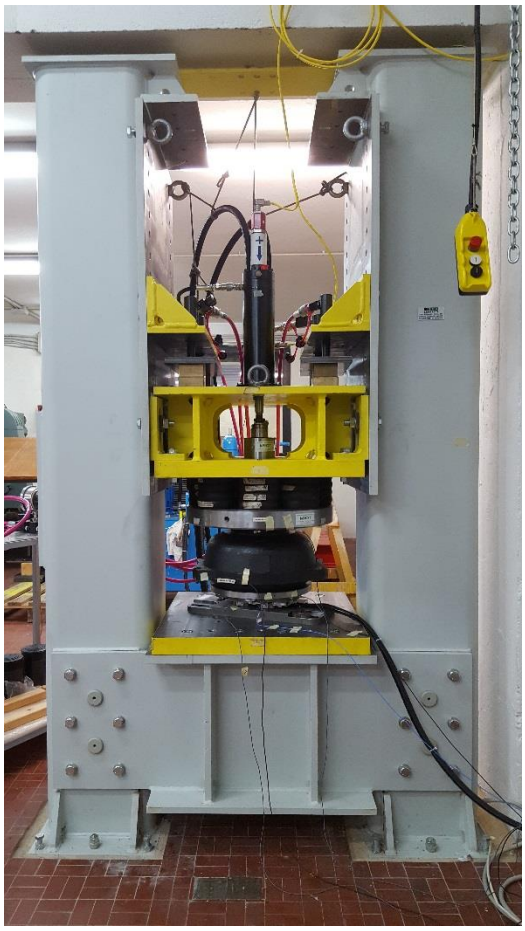

Figure 87: Low frequency test rig at the NVL laboratory

At first, the methodology to follow during the experimental campaign will be exhaustively described, focusing on the procedure and the used measurement instrumentation with a brief description of the test rig components and additional elements.

The coordinate system described in part II.C and III.A were used, where the vertical direction is represented by the *z* axis and the transverse directions by the *x* and *y* axis.

A. METHODOLOGY AND SETTINGS

The apparatus used for this campaign is a test rig specifically designed for low frequency behaviour studies according to the ISO standard presented in part II.D.1. While designing of the test rig, the natural frequencies was determined, with the lowest one around 133 Hz relevant to transverse bending mode. This relatively low value could lead to possible signal disruption during the dynamic experiments while focusing on the RME transverse behaviour. Indeed,

Although the modal behaviour of the test rig could decrease the quality of the results for the transversal characterization, it does not influence the results relative to the vertical DTS determination. Thus, there is no limitation as for the frequency range study when focusing on the vertical RME characterization. So the DTS was determined on the previously fixed frequency range between 1 and 50 Hz. The static pre-compression is fixed at 75kN, which correspond to the working point of the resilient mounting T200. This load leads to a static deflection of 9.75 mm measured top par top part and the bottom part of the RME. As there were no previous investigations about the RME characterization in the low frequency range in the NVL laboratory, several types of input signal were chosen for the displacement dynamic excitation to verify the impact of the input signal on the resulting DTS.

1. Experiment steps.

Using the designed test rig, several stages need to be followed for the behaviour characterization of the RME. At first, the tested element needs to be placed on the test bench respecting the prescription of the standard and, in particular, the RME symmetric planes should coincide with the test rig ones. Then, the static pre-compression at the working load is performed by operating a set of pistons specifically designed for this purpose. At this stage it is possible to verify that the experimental deflection does not diverge from the one provided by the manufacturer. Before initiating the dynamic tests, it is necessary to ensure the decoupling between the static compression system and the dynamic excitation one. Indeed, if the dynamic excitation system performs also the compression, it should be capable to reach the right compression load. However, the dynamic actuator is not able to do create and maintain the compression load, and, in the same time, operate the dynamic excitation, due to the pressure limitation of the hydrodynamic actuator. Therefore, a compression system should operate the compression and maintained it, by on one side, and, on another side, the hydrodynamic actuator should generate the dynamic excitation.

An interval of 24h should be respected between the end of the compression and the beginning of the dynamic test as recommended in the standard to avoid potential elastomeric behaviours that would disturb the measurements, such as rubber relaxation. Then the dynamic characterization can be operated at the chosen static load.

At the end of the dynamic test, a set of measured data, obtained by using different dynamic input signals, is available for the evaluation of the transfer function of the RME. Figure 88 shows the followed procedure to perform the characterization of the RME.

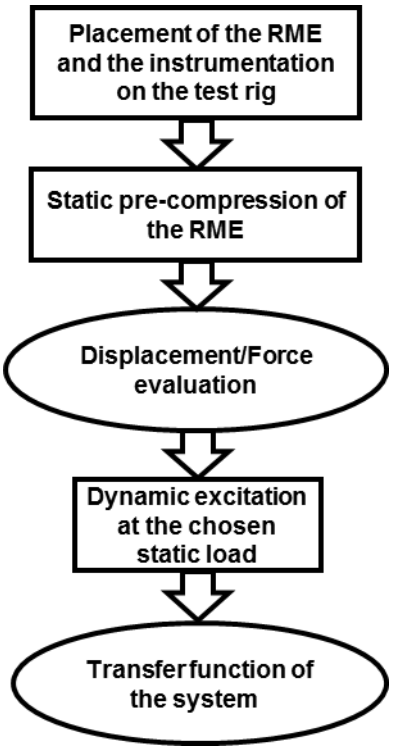

Figure 88: Experimental steps

To ensure the quality of the results, the first phase of the experimental test requires carefulness and high precision in the operating of the. Indeed, the initial conditions significantly impact quality of the measurements. Therefore, this phase will be exhaustively describe.

At first, the mounting element is placed on the distributing plate avoiding non-symmetrical arrangement in order to optimize the quality of the measures, then the exciting mass is accurately placed on the top of the tested T200, and finally, soft isolators are placed between the exciting mass and the mobile traverse. These soft isolators will play two roles: transmitting the static load to the element while isolating it from the possible flanking transmissions. Before to apply the static compression, all the sensors are placed. This instrumentation is described in the next part. The static compression is performed gradually until the working load, and step by step the induced deflection measured and compared to the expected in order to corroborate the data provided by the RME provider. When the working point is reached, the mobile transverse is bolted to the test rig frame to maintain the compression load on the RME. After a check on the overall installation the dynamic test can start.

The tests were performed between May and June 2016. The temperature control specified in the standard was not necessary due to a mild ambient temperature about a constant value of 25°C maintained during the experiment. According to the standard, the test was performed at the ambient temperature and not at the working temperature of the RME, which is expected around 40°C.

As it was mentioned previously, several types of input signal have been use to evaluate their influence on the vertical dynamic transfer stiffness of the mounting element. Among the four possible types of input signals proposed by the ISO 10846 standard, two types were chosen, a sine sweep and a white noise:

- Signal A: a sine sweep signal with a constant velocity profile of 40 mm/s, from 1 to 50 Hz
- Signal B: a white noise signal with a constant spectral density of 1.0E-03 (g^2/Hz), from 2 to 10 Hz
- Signal C: a white noise signal with a constant spectral density of 3.4E-04 (g^2/Hz), from 4 to 40 Hz
- Signal D: a white noise signal with a constant spectral density of 6.9E-04 (g^2/Hz), from 4 to 40 Hz

where signal A corresponds to the maximum working condition of the dynamic actuator. Different levels of white noise signals (B,C,D) have been also used to perform the linearity test as prescribed in the standard. The choice of those specific white noise signals will be explained in section IV.B.1.a.

2. Used instrumentations and used apparatus

For the measurements of the requested physical quantities, the following instrumentation was used:

- One capacitive displacement sensor measuring the vertical displacement of the piston, placed at the top of the stinger
- One uniaxial piezoelectric accelerometer measuring the vertical acceleration of the exciting mass, placed at the centre of its upper surface
- One triaxial piezoelectric accelerometer measuring the vertical acceleration of the exciting mass, placed at the centre of its upper surface measuring the vertical an the two transverse acceleration of the exciting mass, placed on its side surface
- One uniaxial piezoelectric accelerometer measuring the vertical acceleration of the exciting mass, placed at the centre of its upper surface measuring the vertical acceleration, of the distributing plate, placed on its upper surface.
- Four piezoelectric force transducers measuring the vertical an the two transverse forces transmitted to the test rig basement, placed between the distributing plate and the foundation
- One uniaxial piezoelectric accelerometer measuring the vertical acceleration, placed on the top of the test rig foundation

Figure 89 shows the configuration of the set of sensors used in the experiment both in schematic view and in real situation.

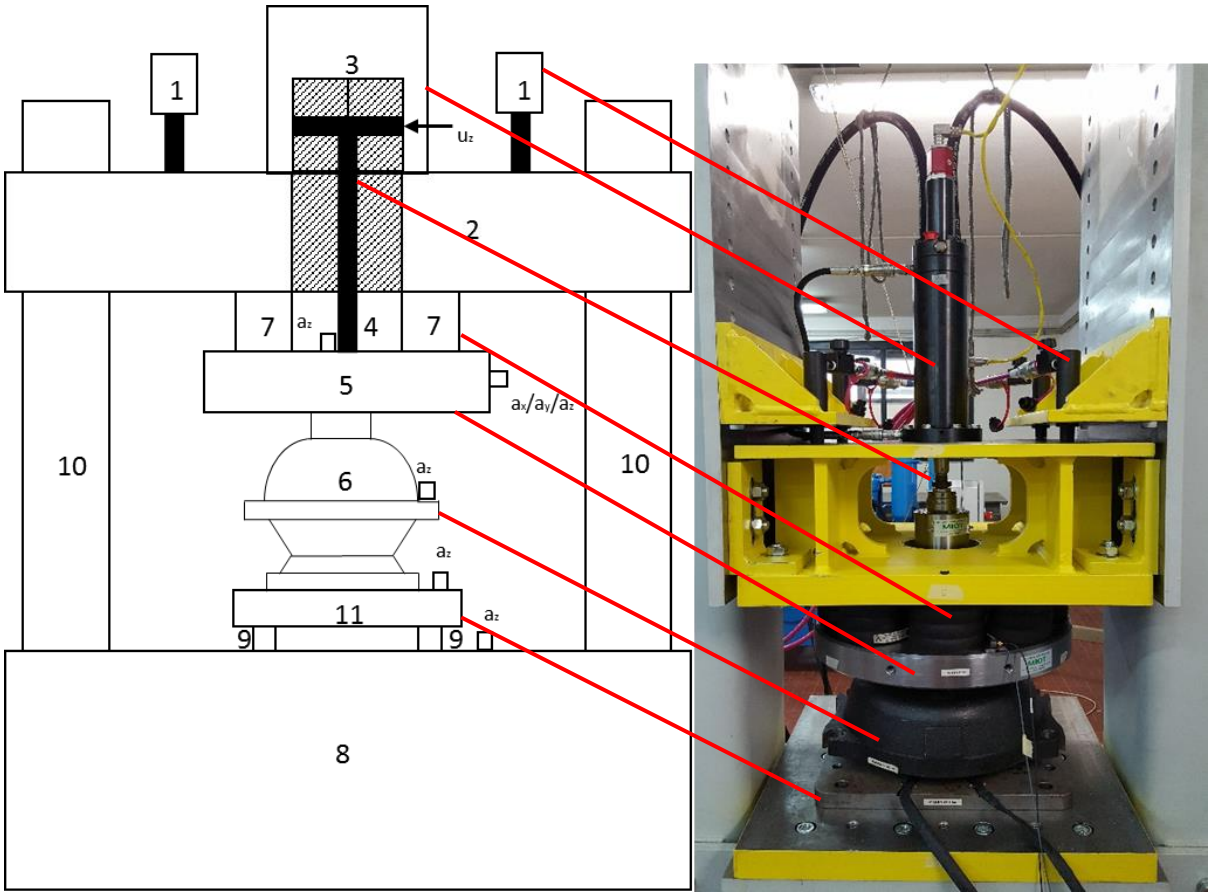

Figure 89: Test rig representative drawing and test rig central parts

Figure 90 exhibits the whole apparatus: on the left the hydrodynamic power unit of the dynamic actuator, in the centre the hydraulic static compression system, and on the right the test rig.

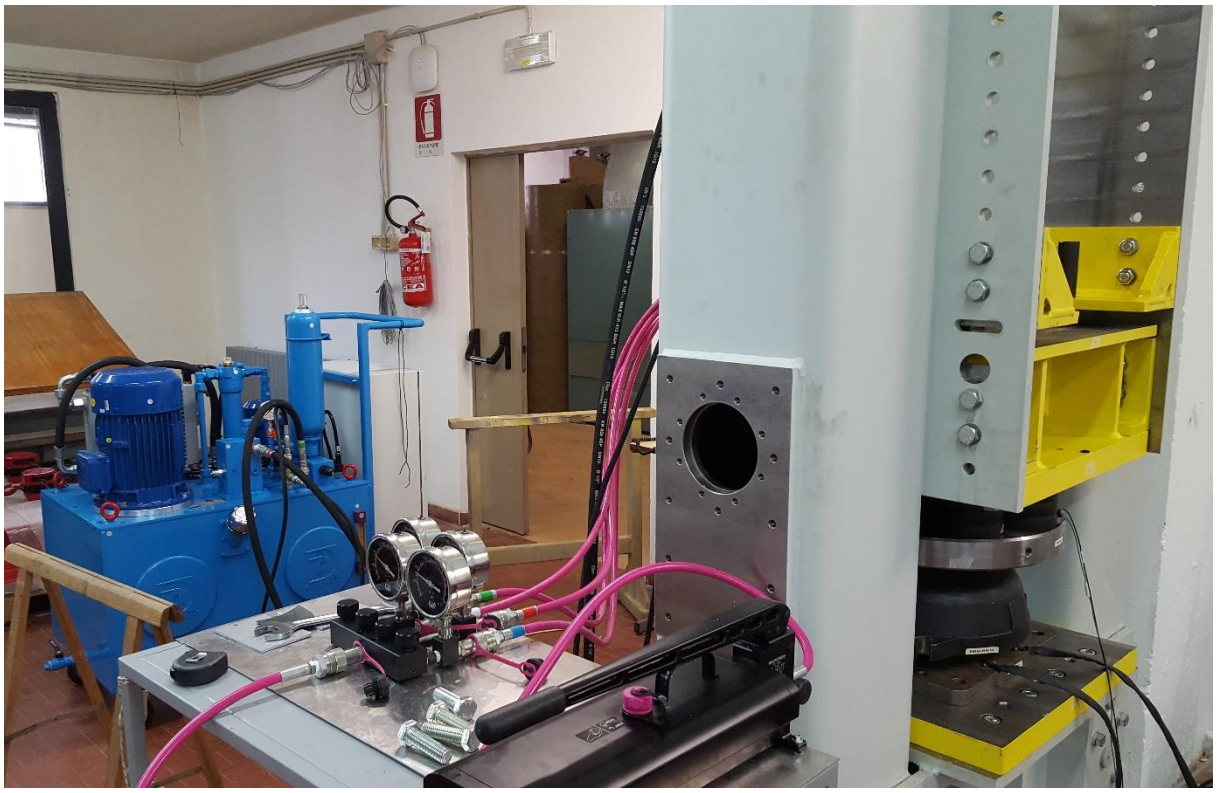

Figure 90: Test rig with the static compression system and hydrodynamic system

The hydraulic static compression system consists of four pistons (Figure 89, label 1) connected to the manual pump (Figure 90) by a manifold used to coordinate the movement of the set of pistons. The working pressure is set to 260 bar for each piston to reach 74 kN of compression force. This piston are capable to reach 100 kN.

The hydrodynamic power unit is connected the actuator which generate the input oscillations of the exciting mass for the dynamic experiments. The working pressure is also set at 260 bar, respecting the actuator use specifications. The used fluid in the pump is a low-viscosity oil, in order to reduce at the maximum the cavitation and keeping a laminar flow in the servo-valve and the whole system. The actuator movement is created using a servo-valve, which direct the oil in the upper or lower chamber of the actuator, creating a difference of pressure. A controller with a PC software user interface commands the electro valve.

All the instrumentation is connected to a data acquisition system (DAQ) to register the time signals (accelerations, displacement and forces). The software generates the signal, which serves as the input to the actuator controller for the servo loop of the system.

It is worth to note that the DTS calculated by making use of the displacement measured with the sensor placed at the top of the stinger is not accurate. In fact, this displacement sensor is measuring the displacement of the stinger top which is different from the one applied to the tested element due to the deformation of the stinger and of the frame of the test rig.

In order to perform the verification of the standard prescription, the mass of the distributing plate was evaluated as it influences the dynamics of the oscillating system. The mass is 12 kg.

3. Data post-treatment

As previously presented, the time domain signals used for the data post-processing are those given by the accelerometers force transducers. Even if the transducer placed at the top of the stinger does not only measure the displacement of the tested specimen, as previously discussed, a DTS was obtained using such time domain signal just for comparison purposes. This comparison is realized using the sine sweep type signals.

As it was discussed in section I.B.3, the DTS can be calculated from the complex apparent mass, by applying the following equations:

$$K^*(f) = -(2\,\pi\,f)^2 \times \frac{F_j^*(f)}{a_i^*(f)} \quad 165$$

which leads to

$$|K^*(f)| = (2\,\pi\,f)^2 \times \left|\frac{F_j^*(f)}{a_i^*(f)}\right| \quad 166$$

And

$$\eta(f) = tan(\phi) = \frac{Im(K^*)}{Re(K^*)} = tan(\,cotan\left(\frac{Im\left(\frac{F_j^*(f)}{a_i^*(f)}\right)}{Re\left(\frac{F_j^*(f)}{a_i^*(f)}\right)}\right) + \pi) \quad 167$$

with $Im(K^*)$, imaginary part of the complex number $K^*$and $Re(K^*)$, real part of K^*.

The DTS so obtained have then compared to each other's in terms of magnitude $|K^*(f)|$ and tangent angle loss $\eta(f)$.

B. RESULTS

The verification of the results is mandatory to acquire an accurate dynamic transfer stiffness, ensuring several requirements about the behaviour (static and dynamic) of the system and test rig. This validation is crucial to be able to infer the reference curves for the comparisons with the numerical DTS. Then, it is possible to interpret the results and potentially validate the procedure developed in the thesis. The DTS of the previously displayed trials are analysed, in terms of magnitude and tangent angle loss.

1. Verification of the results

For the endorsement of the resulting DTS, it is necessary to respect the prescriptions of the ISO 10846 standard, presented in the section **II.D.1.b.** The verification is focusing on the check of the linearity of the tested element behaviour, the respect of a low level of unwanted input vibrations, and the examination of the distributing plate influence on the results. Thus, if the requirements are fulfilled, the potential influence of the critical parts behaviour (dynamic and static), as discussed in section **II.D.1.a**, on the measurements can be considered negligible.

a) Linearity test

Even if it was planned to use signals B and C for the linearity test, due to difficulties that emerge during the experiments, it was decided to use an additional signal (signal D), which characteristics satisfy the exciter capabilities. In fact, the dynamic exciter had difficulties to maintain a constant signal spectral density between 1 and 50 Hz. Indeed, the signal C amplitude was too low to be maintained below 4 Hz and the signal B amplitude was too high in high frequency range (above 10 Hz). In conclusion, due to the difficulties to have two input signals with a difference of 10 dB in terms of level amplitudes between the respective signals, the three signals B, C and D have been used to cover the complete frequency range. The signal A, as for it, can be operated by the actuator in all the frequency range due to its nature (constant velocity).

In consequence, the linearity comparison will consist to a first comparison between the signal B and C between 4 and 10 Hz for the low frequency spectrum. A second comparison will be presented between 4 and 40 Hz using signals C and D. The last comparison, between signals A and D, focuses on the influence of the signal type on the resulting dynamic transfer stiffness. The difference obtained in this comparison should be less than 1.5 dB to ensure the linearity

Figure 91 shows the three differences (comparisons) calculated from the resulting DTS obtained with the fourth previously mentioned signal.

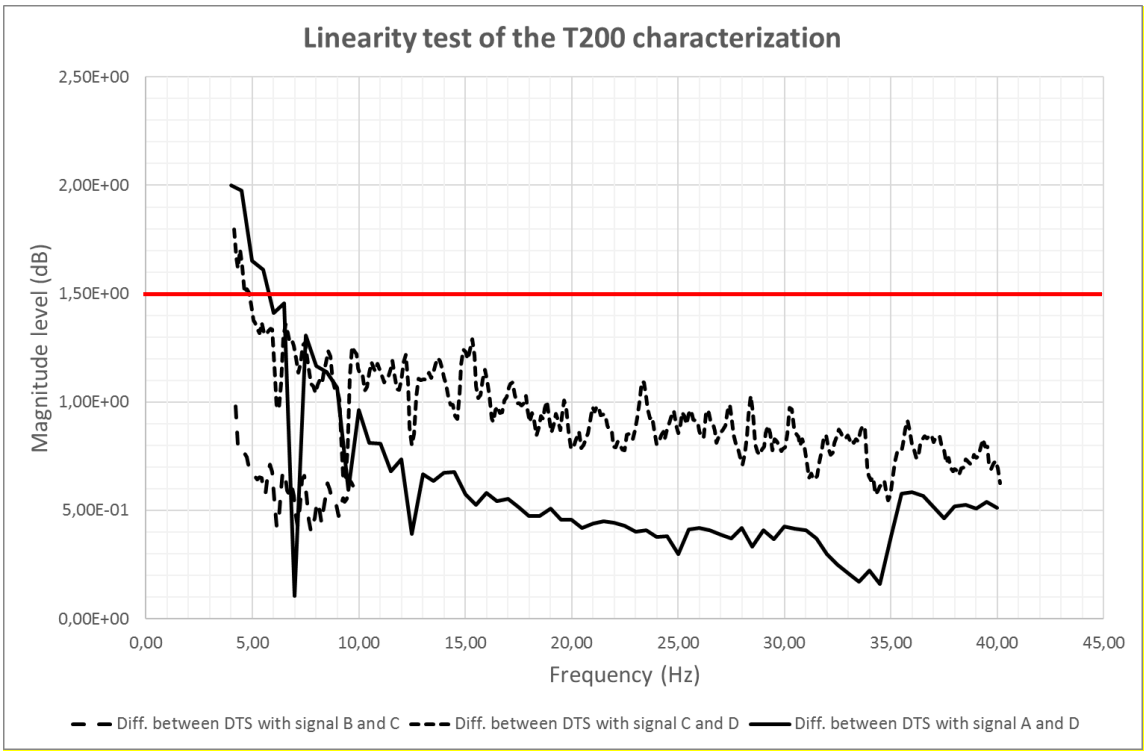

Figure 91: Linearity test for the experimental DTS

The first difference, represented by the curve with **long dot** in the graphic, is calculated from the DTS respectively obtained with the signals B and C from 4 to 10 Hz. Although, this comparison is focusing on a small frequency range, it is pertinent because, in this portion of the studied frequency range, the non-linearity is probable due to higher displacement amplitude, and therefore those high deformation amplitudes can induced nonlinear behaviour of the rubber. In this range, it is worth noting that this difference is not higher than 1 dB, which leads to a partial validation of the system linearity.

After the first comparison, a complementary one was necessary to study the linearity in the rest of the frequency range studied in the thesis. This second difference, represented by the curve with **short dot** in the graphic, is calculated from the DTS obtained with the signal C and the one with the signal D. The comparison is effected from 4 to 40 Hz. The main problem of this comparison lies in the fact that the signal D is only 6 dB higher than signal C and not 10 dB higher as recommended in the standard. In this range, it is worth noting that, if the difference is below 1.5 dB between 5 Hz and 40 Hz, it is higher below 5 Hz (maximum 2 dB). Therefore, it can be possible to ensure the linearity of the system between 5 and 40 Hz with reserves.

The third comparison, represented by the **continuous** curve in the graphic, is calculated from the DTS obtained with the signals A and the one with the signal D. The comparison is performed from 4 to 40 HZ. However, this difference 3 could not be considered a validation of the linearity of the system according to the standard because of the two different type of input signals. In fact, the level of acceleration for the signal with the constant velocity (signal A) is increasing through frequency due to the sine type signal, whereas the level with a constant spectrum density (signal D) is decreasing through frequency. The comparison is instead relevant on the influence of the signal type on the linearity. As for difference 2, the difference 3 is higher than 1.5 dB in the low frequency range, here below 6 Hz. However, this difference is lower than 1.5 dB in the remaining studied frequency range. This brings to consider that the type of input signals does not have a great influence on the results in terms of system linearity and therefore, the input signal type can be indifferently chosen among the proposed in the standard.

Concerning the validation, with the exception of the range below 5 Hz where it is difficult to make any consideration about the linearity of the system, the comparisons lead to the possibility of considering the resilient mounting element as a linear system.

b) Flanking transmissions verification

As it was previously discussed, possible flanking transmissions could occur. Originating from the working actuator, the vibration propagates in all the structure. An investigation on those possible issues are necessary. Their influence on the results could be consider as negligible if the measured acceleration level of the distributing plate is more than 15 dB less than the acceleration level at the centre on the exciting mass. This verification used the result data obtained during the experiment when signal C was used as input signal. In consequence, the standard prescription is verified between 4 and 40 Hz.

Figure 92 shows the configuration where the accelerometers are placed during the experiment. A uniaxial accelerometer placed near the centre of the exciting mass, measures the vertical acceleration at the mass centre (a_{z1}). A triaxial one is located on the side of the mass to measure the vertical acceleration (a_{z2}) and the two transversal acceleration (a_{x2}, a_{y2}) at the side of the exciting mass. It shows also the locations of two other uniaxial accelerometer that measure the vertical acceleration levels at the side of the tested T200 ($a_{z.}$) and at the top of the distribution plate.

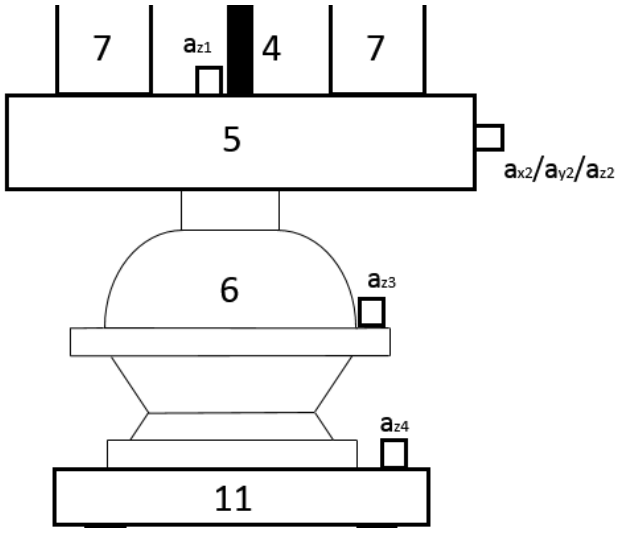

Figure 92: Flanking transmission verification configuration

The two vertical levels are used for the verification of the flanking transmissions are the one at the centre of the exciting mass (a_{z1}) and the one at the top of the distributing plate (a_{z4}).

Figure 93 shows the two levels of vertical accelerations.

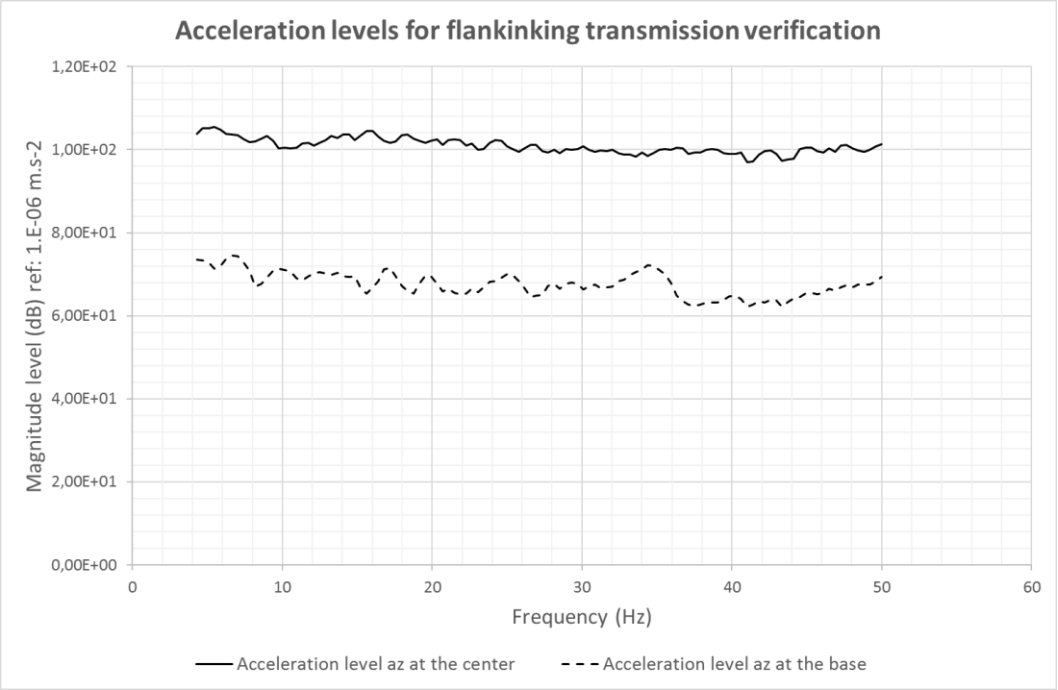

Figure 93: Acceleration level for the flanking transmission verification

The two compared acceleration level are the vertical acceleration (a_{z1}) and(a_{z4}).According to Figure 93, it can be verified that the measured acceleration level of the distributing plate is more than 15 dB less above 4 Hz. Therefore, the prescription is verified the studied frequency range.

c) Unwanted input vibrations

Another important prescription to respect, as prescribed in the ISO 10846-2 standard, is concerning the unwanted input vibration. The acceleration level in the transverse directions on the side of the exciting mass should be 15 dB less than the input acceleration to avoid any disturbance of the measure due to the normal modes of the global structure. This verification used the result data obtained during the experiment when signal C was used as input signal. In consequence, the standard prescription is verified between 4 and 40 Hz.

Figure 94 shows the configuration where the uniaxial accelerometer, to measure the vertical acceleration at the centre (a_{z1}), is placed near the centre of the exciting mass and, where the tri-axial one is located on the side of the mass to measure the vertical acceleration (a_{z2}) and the two transversal acceleration (a_{x2}, a_{y2}) at the side of the exciting mass.

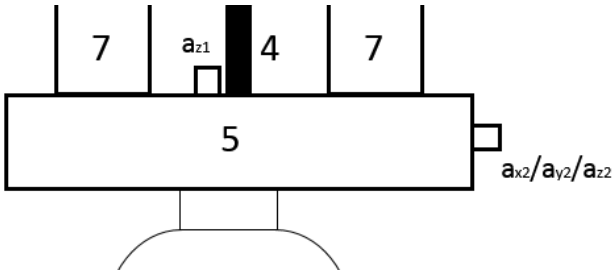

Figure 94: Unwanted input measurement configuration

The level are displayed in Figure 95 for comparison in order to check the minimum difference of 15 dB.

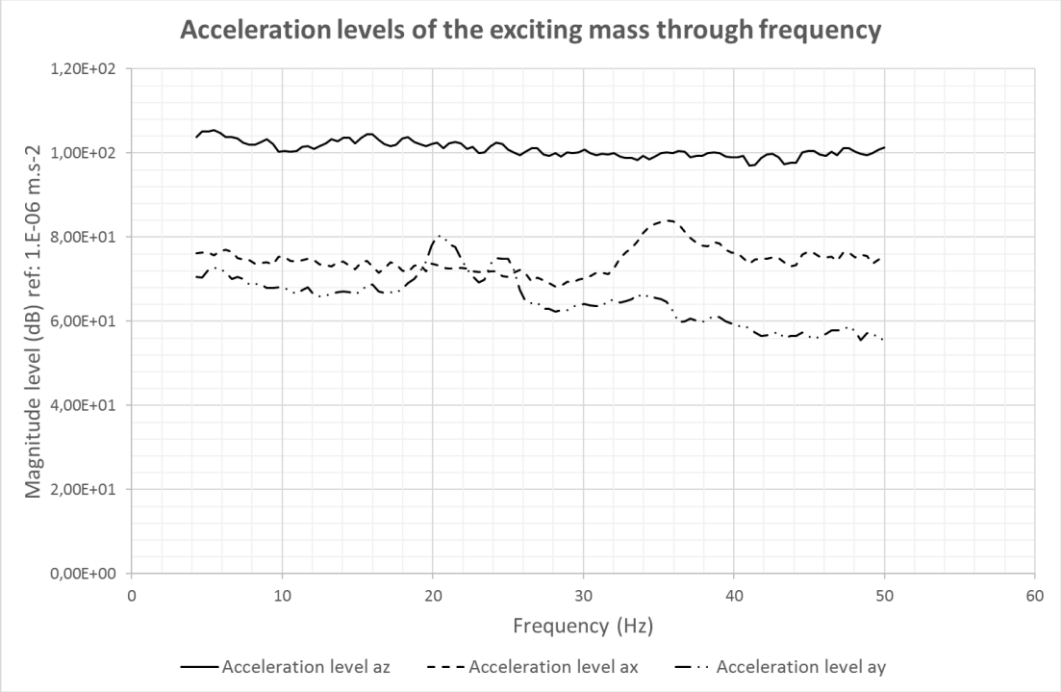

Figure 95: Acceleration levels of the exciting mass

At first, the vertical acceleration level that was used for the comparison is the vertical acceleration level at the centre of the exciting mass and the two transversal acceleration levels at the side of the exciting mass. The difference between the acceleration level in the vertical direction and the two levels in the transversal direction is at least 18 dB above 4 Hz. Therefore, the prescription is verified the studied frequency range.

d) Distributing plate behaviour

Finally, the influence of the distribution plate on the force measurements has been investigate by the values of the vertical acceleration level measured on the plate and the measured force in the vertical direction. This verification used the result data obtained during the experiment when signal C was used as input signal. In consequence, the standard prescription is verified between 4 and 40 Hz.

Figure 96 shows the layout of the mentioned configuration.

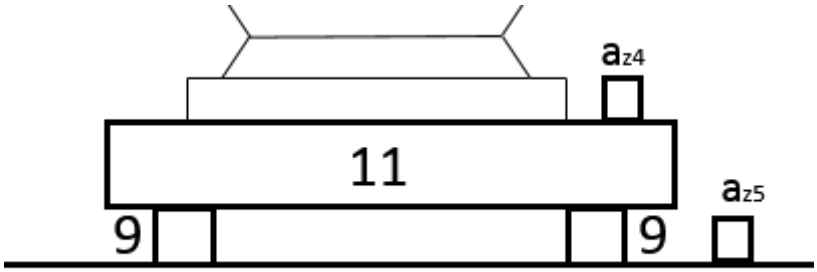

Figure 96: Force level verification configuration

According to the ISO standard the ratio *R,* which is function of the frequency, expressed in kg, in the following equation should be higher than the mass of the distributing plate, which is equal to 12 kg:

$$R = 0.06 \times \frac{10^{\frac{L_{F_2}}{20}}}{10^{\frac{L_{a_2}}{20}}} \qquad 168$$

Figure 97 displays the evolution of the ratio through the studied frequency range.

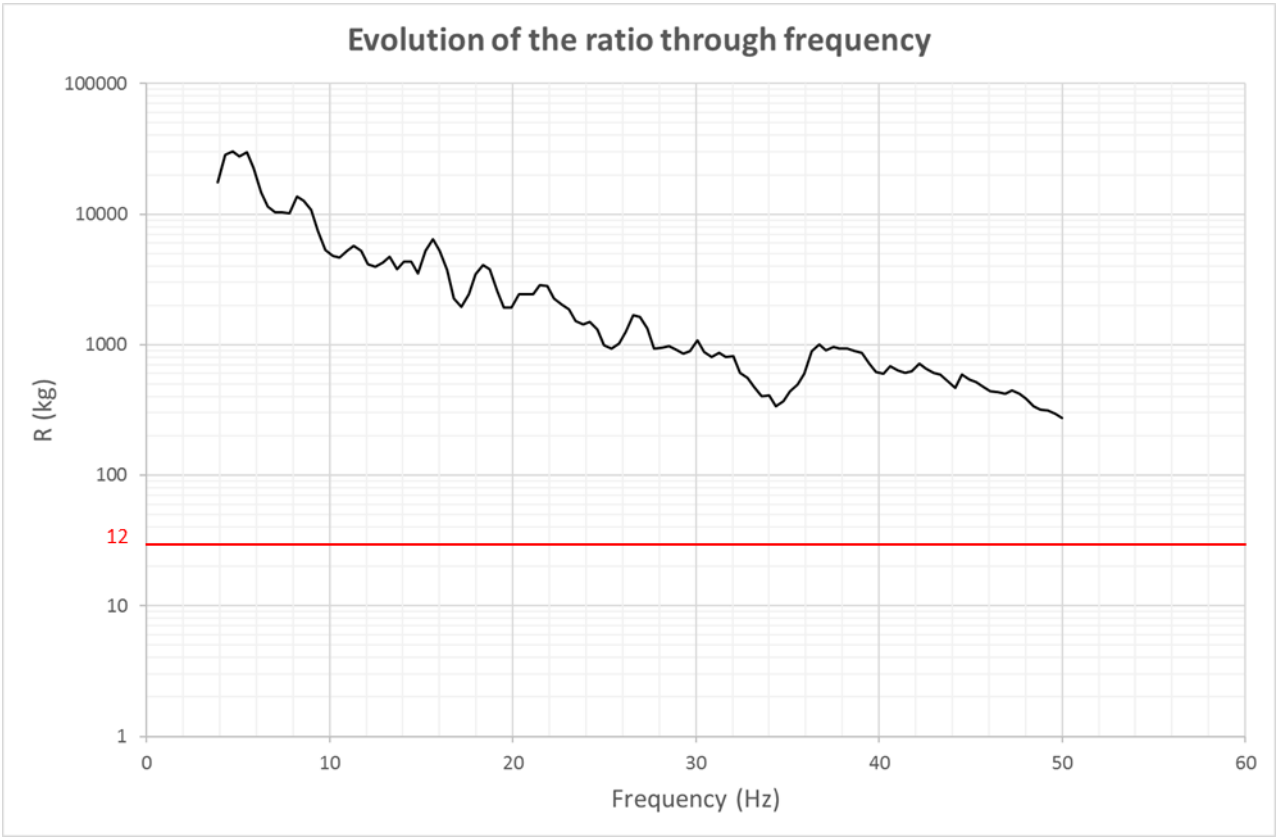

Figure 97: Distributing plate influence verification

The trend of the curve is decreasing while the frequency increase. However, the minimum value is 270, which is higher than the distributing plate mass (12 kg). Therefore, it is clear that the distributing plate has a limited impact on the force measurements. Hence, the prescription is verified the studied frequency range.

In conclusion, the investigations concerning the ISO standard prescription leads to conclude that the setup of the test can be considered acceptable for with some reserves concerning the potential non-linearity of the resilient mount below 4 Hz where it was not possible to investigate the prescriptions.

2. Experimental complex dynamic transfer stiffness

After the validation of the ISO standard requirements, the acquired dynamic transfer stiffness of the resilient mounting element from the several experimental configurations. It is worth to note that those DTS are, at first, acquired from temporal signals and after a post-treatment including the use of fast Fourier transformations. The resulting DTS are therefore, complex number. To represent those DTS, it is possible to display their magnitude in a first graphic and in a second graphic, the tangent of their phase angle, called here, tangent angle loss.

a) Dynamic transfer stiffness magnitude

Figure 98 displays the magnitude of the DTS for the different trials performed in addition of the static stiffness

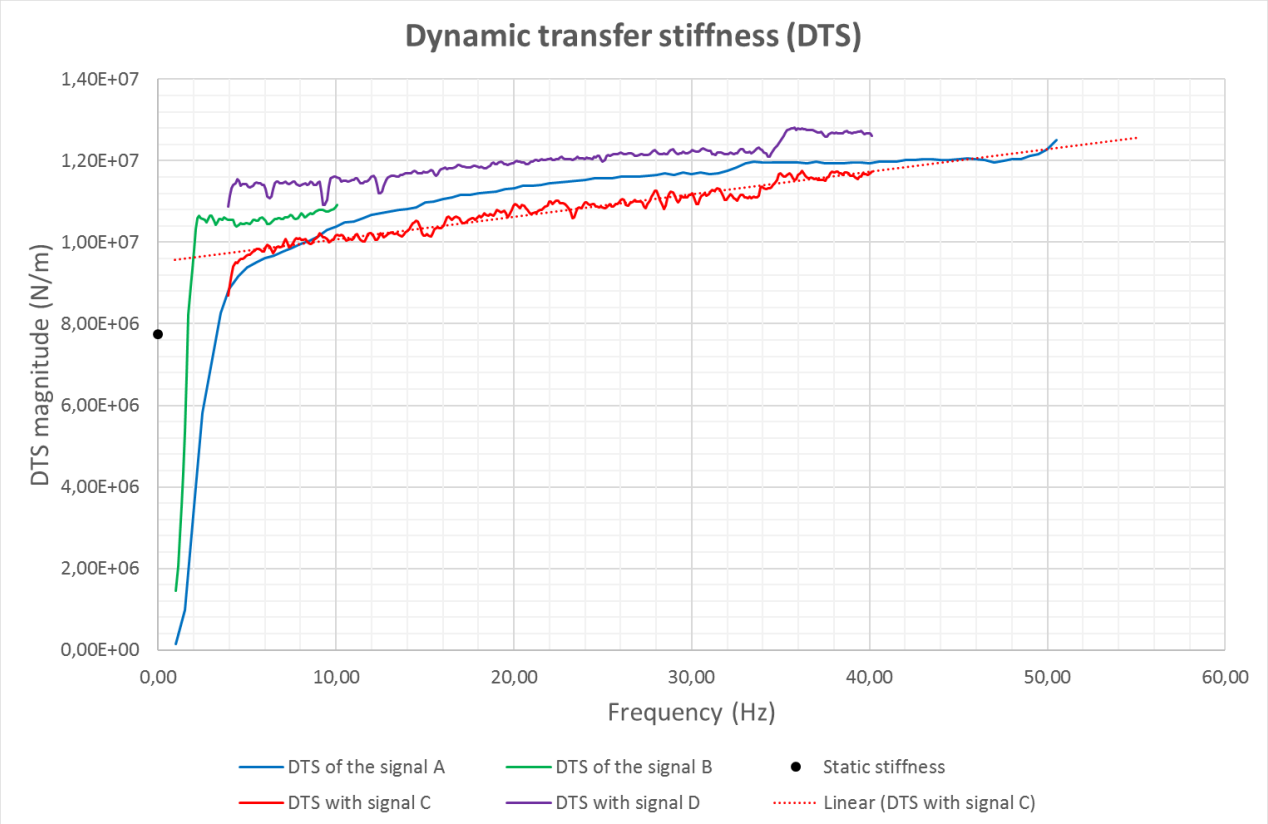

Figure 98: Magnitude of the experimental DTS

The first consideration that can be done is the inconsistency of the resulting DT magnitude. The disparities of the curves is more than 10% at certain frequencies. Hence, several questioning appear considering that the prescriptions the linearity were respected. Due to the fact that those experiments were performed the same day with the same experimental conditions (temperature, compression loads, etc.) the potential features that can affect the measurements are reduced. A phenomenon linked to the Mullins effect could be one of these feature. In fact, as it was advised to wait 24h after the compression to start the dynamic characterization, to avoid relaxation phenomena, this phenomena could had appeared during the test.

Several other unknown phenomena could had appear during those experiments. Due to the lack of time, it was not possible to have more investigations. In this case, deeper experimental investigations are advised to ensure the quality of the measurements.

Another point to notice is the abrupt decreasing below 2 or 4Hz of the DTS magnitude depending on the used signal. It is due to the inability of the used accelerometers to measure accurately the acceleration in low frequency range. In addition, the static stiffness calculated from the static deflection curve is added to verify the coherence of the results. As it was previously discussed in the literature, the dynamic stiffness of systems are commonly higher than the corresponding static one.

However, although, the quality of the results is not satisfying, it is possible to consider that the respective trend of the curves as the same. Therefore, a potential experimental curve that will be considered as the reference for the comparison with the simulation models, can be extrapolated. This curve is extrapolated from the DTS magnitude obtained from the experiment, which use signal C as input signal, using a linear regression. However, the prescriptions were only respected between 4 and 40 Hz. The validity of the extrapolation can not be ensure apart from 4 to 40 Hz.

b) Dynamic transfer stiffness tangent angle loss

The second component of the DTS to examined is the tangent angle loss. As it was previously discussed, the tangent angle loss is linked to the damping properties of the RME.

Figure 99, shows the different tangent angle loss extracted gleaned from the post-treated measurements.

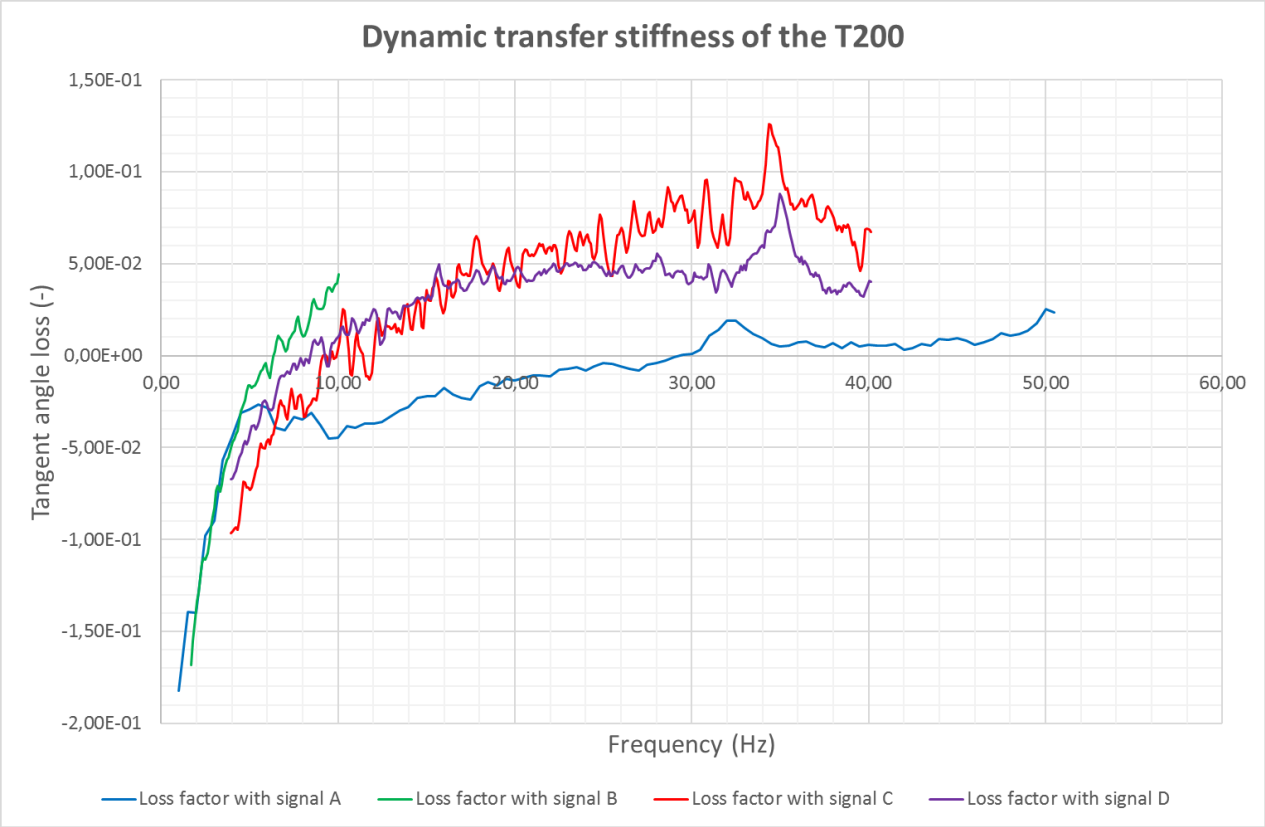

Figure 99: Tangent angle loss of the experimental DTS

Considering the tangent angle loss, it can firstly be noticeable that the dispersion of the results is high. In addition, the curves seem to depend highly on the type of input signal. Furthermore, it appears that the tangent angle loss is negative in the low frequency range below a frequency that depends on the used signal. As explained in section I.D.2., the tangent angle loss is a physical quantity that should always be positive due to the angle loss definition interval [0°;180°]. As for the DTS magnitudes, the tangent angle loss curves discrepancy and odd values are the consequence of the fact that the measured phase angle and the sensibility of the sensor are of the same order of magnitude.

Thus, it is difficult to extrapolate a trend line for the tangent angle loss. A possible explanation about the higher tangent angle loss obtained with the displacement sensor is the influence of the viscosity of the oil in the actuator chamber. As with the DTS magnitude discussion, due to the time restriction, there were no possible additional investigations on this problematic.

In conclusion, the validation of the procedure will be evaluated using the DTS magnitude extrapolated curve of the RME as a reference and will be confronted to the ones obtained by simulations. The validation will not be possible with the tangent angle loss due to the unsatisfying quality of the results.

V. DTS DETERMINATION BY SIMULATION

In this section, the experimental results acquired in part IV. (DTS magnitude and tangent angle loss) are compared to the results obtained by simulations. If this comparison is inconclusive, other type of simulation will be attempted for the comparison. For the creation of the models used in the simulations, the results gathered in the dynamic mechanical analysis (part III.) are necessary, especially for setting of the behaviour material laws. DMA measurements allow for the construction of the model that integrates the pre-compression effect on the rubber, modifying its stiffness. As mentioned in section I.A.3, the ratio between the dynamic amplitude and static one can be considered sufficiently low to assume a linear behaviour of the elastomer around the working point. Therefore, it can be supposed that the Young modulus of the rubber remains constant. However, DMA measurements show that both the Young modulus and the tangent angle loss vary with the excitation frequency. Like experimental measures which provide a DTS depending on the frequency, the numerical model should also allow to calculate a DTS which may vary with the frequency. At the end of this section, the validity of the numerical procedure is discussed.

A. NUMERICAL SIMULATIONS

Firstly, numerical simulations were performed using the finite element software LS-Dyna. The main objective of such simulations was to determine the vertical DTS of the RME. In this situation, the RME can be considered as a 1D vertical system with the related vertical stiffness and damping. In order to calculate the DTS, the excitation is a purely 1D directional displacement vector and the post-processed result is the resultant force vertical component.

Two types of numerical simulations are possible to express the vertical DTS as a function of the frequency. A first one, called frequency response analysis, is performed in frequency domain, by characterizing the DTS for each required frequency. For a given excitation load, Equations 16 or 17 are mathematically solved for each discrete frequencies in the studied frequency range. The second type of simulation is performed in time domain and is based on an excitation similar to the ones used in the experiments (random noise or sine-sweep signals). In this case, equation 11 is mathematically solved at each simulation time step. Then, the DTS, expressed as a function of the excitation frequency, is obtained from time domain using a fast Fourier transform. This simulation procedure is thus very similar to the experimental one.

In order to take into account the pre-compression effect on the rubber part, only the second type of simulations is possible. First, the simulation of the quasi-static response of the RME to the pre-compression load is carried out. The resulting files are then used as input (initial state) for the time step-by-step dynamic simulation. To simulate accurately the experimental loading, a stepped sweep sinusoidal signal is applied on RME top. The choice of the stepped sine-sweep will be discussed later.

As the dynamic simulation is performed in time domain, two time integration schemes, namely explicit and implicit, can be used as discussed in section I.D.3. In this case, it is necessary to have a step-sine sweep that is correctly discretized and 20 points are at least required to represent precisely a sine wave. The maximum frequency in the simulation being, at maximum, 50 Hz, the time step (Δt) should be equal to 2µs. Regarding the Fourier transform, the time step is inversely proportionate to the maximum frequency of the transformed signal. Then, the maximum possible frequency is 5000Hz. Furthermore, the frequency step (Δf) of the signal obtained by the Fourier transformation is proportionate to the time signal length which will be specified in section c.

1. Finite element model

The finite element model used for dynamic simulations is similar to the one used in quasi-static one. In fact, the dynamic calculation is initialized from the 3D stress and strain fields obtained from static simulation. The only difference between static and dynamic models is the presence of a 1D viscous damper element in the latter to simulate the viscosity component of the rubber. In fact, several attempts to model correctly the viscosity were achieved. At first, as the DMA experiments give a structural damping (tangent angle loss), a structural damping was implemented on all part of the model. As it was previously presented in section I.B.3., the structural damping is related to the system stiffness. In this case, the structural damping coefficient is applied, individually on a part or globally in the model, on the stiffness matrix of the related elements. In fact, the use of the structural damping in LS-Dyna did not give acceptable results for unknown reasons. To overcome this problem, instead of structural damping, viscous damping was considered. As it was discussed in the end of part III and in section I.B.3, the viscous damping is directly related to the structural damping at a given frequency. As shown in Figure 100, two viscous discrete dampers were considered in our finite element model.

Figure 100 displays the resilient quarter model at the initial state of the dynamic simulation.

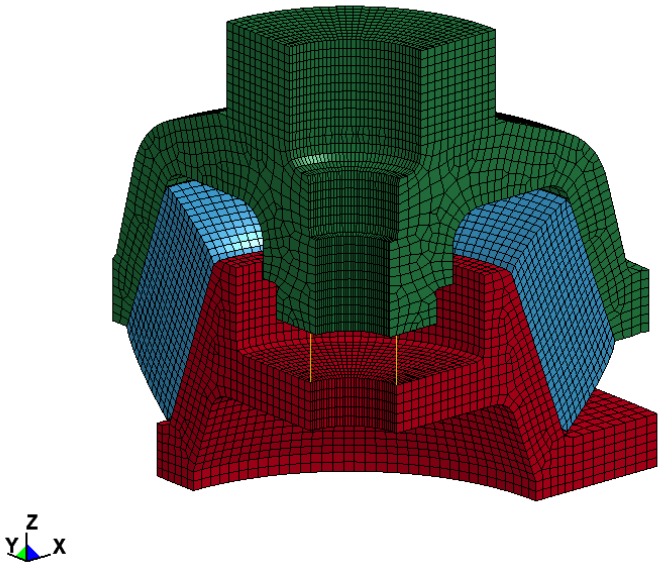

Figure 100: LS-DYNA dynamic quarter model

The viscous dampers are modelled using 1D discrete elements displayed in yellow colour in figure above. As in the quasi-static simulation, the rubber part is rigidly connected to the top casting and the base; no contacts laws were defined. In order to be as near as possible to the experiments, 0D mass elements were integrated to the model and placed at the top surface of the top casting. ~~However, this mass should not have a significant influence on the simulation due to the control in displacement.~~ ~~The RME cannot enter in resonance.~~

a) Boundary conditions

As the dynamic model uses the final step of the static simulation as initial state, the boundary conditions of the dynamic model are the same as in the static simulation regarding the symmetry as well as the steel base bottom conditions.

b) Material law and damping

At first, it was decided at the end of the quasi-static simulations that rubber material law in this model should be the Hook law. Using the DMA experimental campaign results, it is possible to express the complex Young modulus at the working point as a function of the frequency. According to the DMA results, the Young modulus and the structural damping increases with the frequency, but it is unfortunately not possible to define variable parameters in the material law when using LS-Dyna software. Indeed, it is not possible to update the Young modulus value when the simulation is performed in time domain. As for the Young modulus, the viscous damping coefficient cannot vary with the frequency in LS-Dyna. Hence, simulations with different couples of Young modulus/viscous damping were performed.

The following table shows the different couples featured in the final comparison:

	Young modulus (MPa)		
Damping (N.s.m^{-1})	6.8	7.2	8
4000		x	
2000	x	x	x

Table 1: Simulation Young modulus/damping couples

The chosen values of the Young modulus are the lowest one (6.8 MPa) extracted from DMA results in the studied frequency range, the mean value (7.2 MPa) and the highest value (8 MPa). In the same way, according to the DMA results, tangent angle loss varies from 0.8 to 0.11 with an average value of 0.925. At first, due to the potential amount of simulations for each planned couple, 9, it was decided to only use the average value of the structural damping, which corresponds to a viscous damping equal to 2000 N.s.m^{-1}. The relevance of using 4000 N.s.m^{-1} value for viscous damping will be further discussed with the simulation results. The use of these couples could frame the expected DTS that would be obtained if it was possible to consider Young modulus and damping varying with the frequency.

c) Input

The setting of the dynamic excitation requires to be done with caution. In ISO standard, four input types of signal are advised, that is a random noise signal and a sine sweep with three variations. Among these possibilities, the discreetly stepped sine sweep was chosen due to its ease of creation and use in LS-Dyna, with an arbitrary displacement amplitude of 1 mm. For every frequencies, the signal is applied during eight oscillations, which permits to keep the same excitation energy for each frequency. The step sine sweep varies from 1 to 50 Hz with a frequency step of 0.2 Hz. Consequently, the excitation signal is applied at the top of the RME during around 162 seconds.

Figure 101 shows the evolution of the input signal frequency as a function of the time.

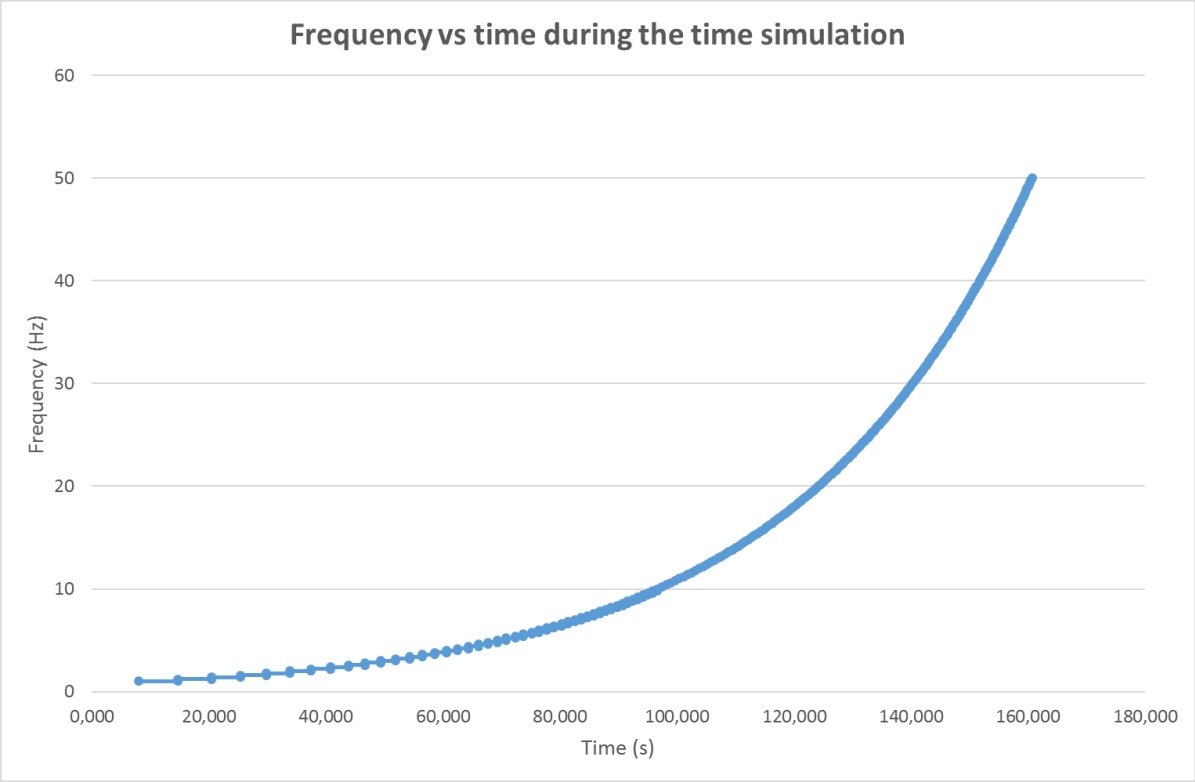

Figure 101: Frequency evolution trough the simulation time for the step sine sweep

Furthermore, regarding the Fourier transform, it is worth noting that a simulation length of 162 seconds in time domain allows for a frequency step of around 6.2 mHz in frequency domain.

1. Comparison with the experimental results

Once the RME reaction force time history has been post-processed from dynamic simulation, fast Fourier transformation of imposed displacement and reaction force were carried out in order to build the numerical DTS in frequency domain which will be compared to the experimental one. Indeed, both the DTS magnitude and the tangent angle loss curves are compared. To increase the clarity of the comparison graphics, the DTS obtained from the Young modulus of 7.2 MPa and the viscous damping of 2000 N.s.m^{-1} is not displayed. Three numerical curves are thus confronted to the experimental ones, in terms of DTS magnitude (Figure 102) and tangent angle loss (Figure 103).

As it was concluded at the end of the experimental section, the DTS obtained with the signal D (white noise from 4 to 40 Hz) was chosen as reference. Corresponding DTS data can then be represented by the following linear regression:

$$K^*(f) = 5.55\,10^4 f + 9{,}4.10^6 \qquad 169$$

The associated coefficient (R^2) of the linear regression is 0.94.

Figure 102 shows the four different dynamic transfer stiffness evolutions within the studied frequency range.

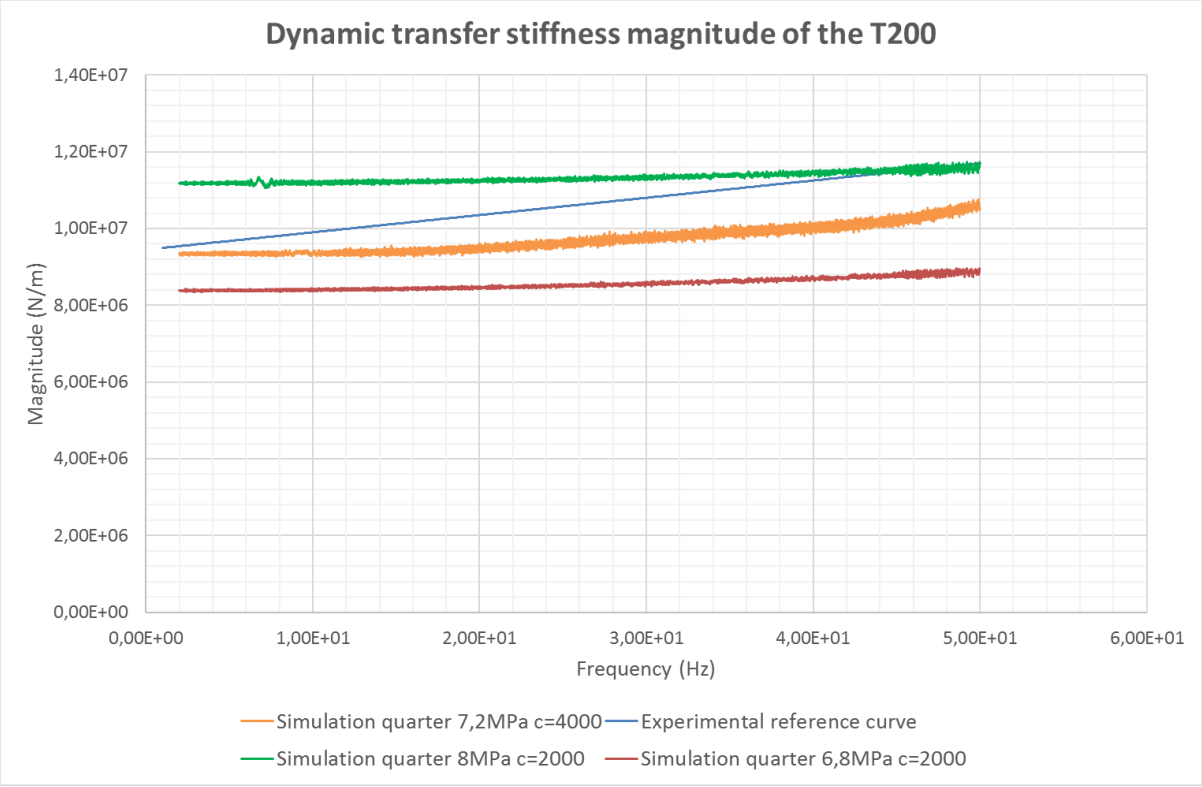

Figure 102: Dynamic transfer stiffness magnitude comparison

Firstly, it can be observed that the numerical curves do not correlate with the experimental curve. In fact, even though the DTS curves related to the Young modulus of 7.2 MPa seem to be in good accordance in low frequency, numerical and experimental slopes are completely different. Furthermore, using the maximum Young modulus (8 MPa), the obtained DTS magnitude is superior to the experimental DTS in all the frequency range, which could be considered coherent. Using the minimum Young modulus (6.8 MPa), the resulting DTS magnitude is inferior to the experimental DTS in all the frequency range, which is also coherent.

As it should be expected from the DMA results, the Young modulus increases with the frequency but it was not possible to integrate this variation in the model. This could partially explain the discrepancy regarding the curve slope. On the other hand, the numerical curve related to the maximum Young modulus seems to correlate better with the experimental one in the high frequencies of the studied range. Nevertheless, the numerical curve slope is again clearly much lower than the experimental curve one.

It was noticed that damping actually influences the DTS slope. As shown in Figure 102, the slope of the two DTS curves calculated with a damping of 2000 $N.s.m^{-1}$ is too small when compared to experimental result. Therefore, another simulation based on a damping doubled value was tried and Figure 102 shows that the resulting DTS curve slope is increased. Indeed, it can be observed that this curve (7.2 MPa & 4000 $N.s.m^{-1}$) and the experimental one have almost the same asymptotic slope.

Even if the comparison of the different acquired tangent angle loss is not as important as the comparison concerning the DTS magnitude, it is still necessary to investigate this topic.

Figure 103 shows the four different tangent angle loss evolutions within the studied frequency range.

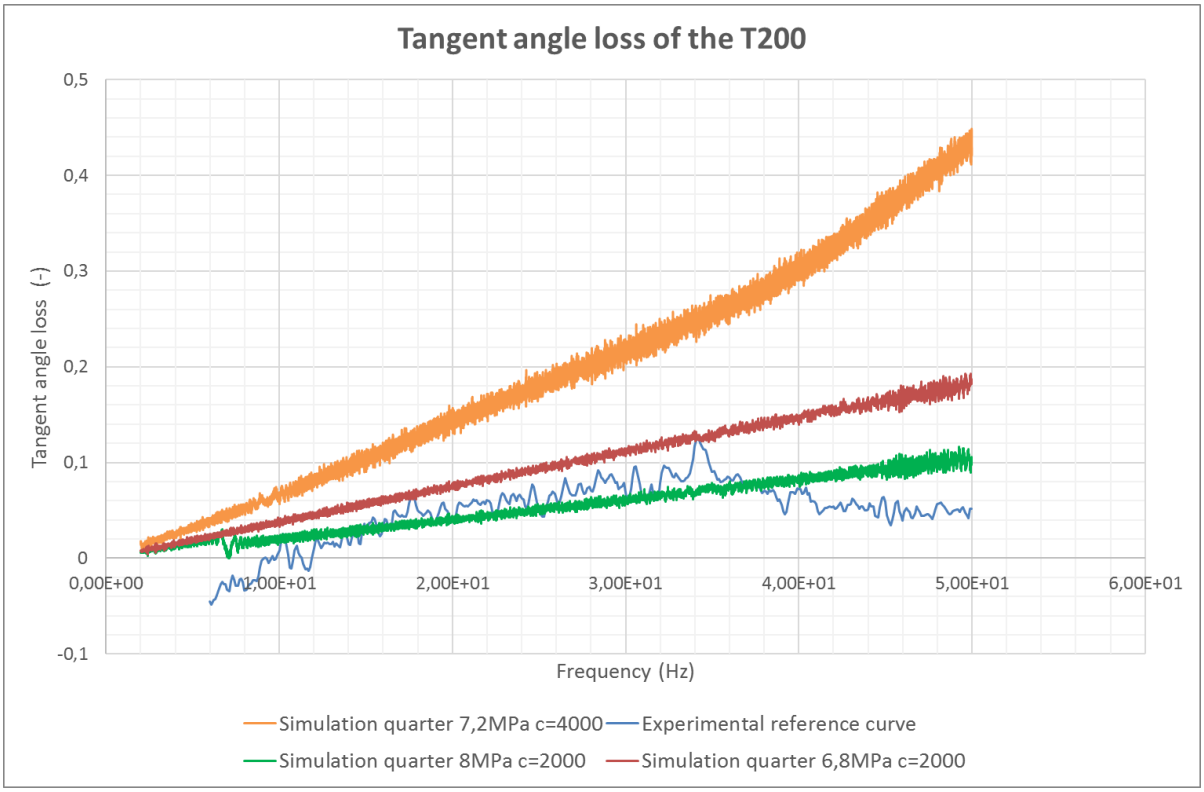

Figure 103: Tangent angle loss comparison

At first, it could be notice that the dispersion of the results is important even with two curves based on the same viscous damping. The trend of the experimental curve is difficult to extrapolate due to the low value of damping. As a consequence, it can be inappropriate to use the experimental tangent angle loss curve as the reference. In fact, as it was mentioned in the experimental section of the thesis, the phase angle measured by the accelerometer may be considered with caution.

In conclusion, it is difficult to establish a good correlation between numerical and experimental results in terms of DTS magnitude even though the experimental results can be framed. Furthermore, as the quality of the results regarding the tangent angle loss is somehow quite poor, the validation of the followed procedure could not be ensure. Regarding the last comparisons, It is therefore uneasy to validate completely the procedure developed in the framework of the thesis.

B. ANALYTICAL SIMULATIONS

As it was observed in the previous part, the numerical simulations do not give results with sufficient qualities in terms of DTS magnitude and, in terms of tangent angle loss. Moreover, regarding the tangent angle loss, the comparison becomes questionable due to the uncertainty on the experimental results. Therefore, the validity of the procedure developed in the thesis is difficult to establish.

In this perspective, as it was previously mentioned, in part I.B.4 and I.C.2, it is possible to use a 1D analytical model to model a viscoelastic material that is submitted to a one dimensional excitation. The first interest of this analytical model is that it is much more easy and rapid to vary some parameters as compared to the numerical one. For a better understanding of the issues met when modelling the damping, both types of damping could be use (viscous and structural).

At first, it is necessary to acquire the evolution of the Young modulus and the tangent angle loss in a form that can be implemented in the analytical model. In this situation, a regression analysis of the relative DMA result curves is judicious. For the analytical model, the Young modulus and tangent angle loss need to be expressed as a function of the frequency only, keeping the other parameters constant. If the DMA curves are considered, a linear regression is not sufficient to express either the Young modulus or the tangent angle loss. Among the potential regression functions, a polynomial one seems to be the most appropriate. This regression should be performed on the averaged curves acquired with the DMA.

Figure 104 displays the averaged Young modulus versus frequency curve with the related regression curve.

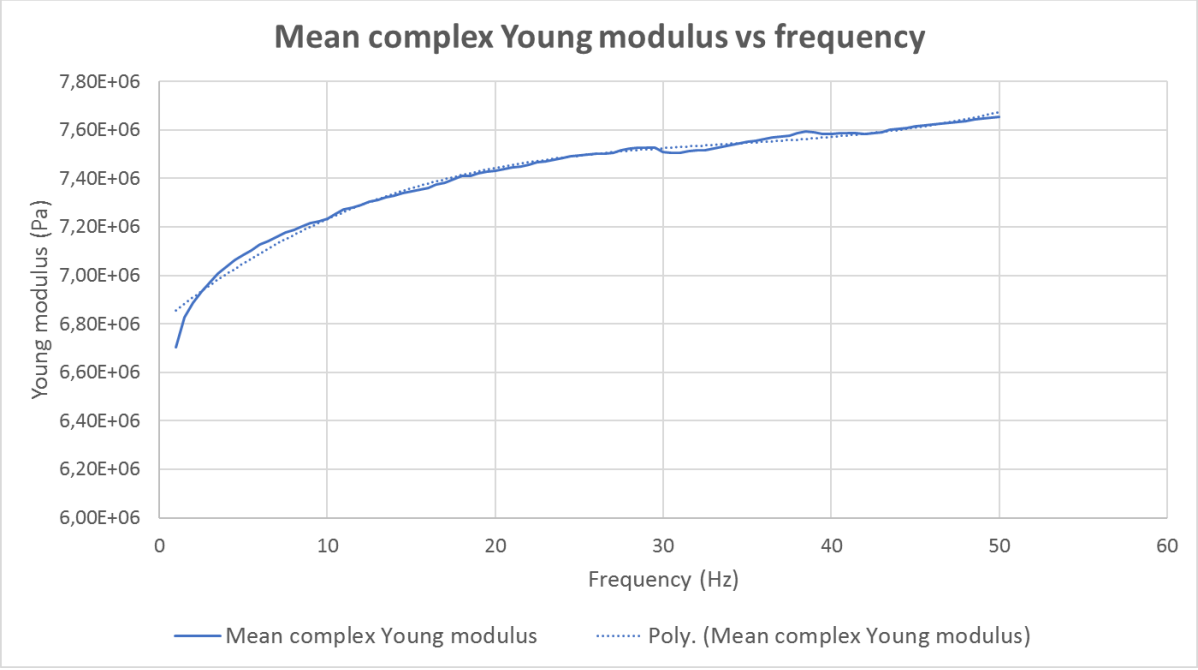

Figure 104: Mean Young modulus value with its polynomial regression

To enhance the accuracy of the regression, the order of the chosen polynomial function may be increased. However, increasing the polynomial order increases also the difficulty to use it for further application. In this studied case, a balanced approach provides a third order polynomial regression. The coefficient of regression (R^2) associated with this regression is about 0.99.

Therefore, the Young Modulus obtained from polynomial regression can be formulated, in Pascal, as follows:

$$E^*(f) = 1.56 \times 10^1 f^3 - 1.59 \times 10^3 f^2 + 5.78 \times 10^4 f + 6.80\,10^6 \qquad 170$$

As for the Young modulus, the same analysis concerning the tangent angle loss regression was done. A third order polynomial regression was also chosen with an associated coefficient (R^2) of 0.97.

Figure 105 displays the mean tangent angle loss through frequency with the related regression curve.

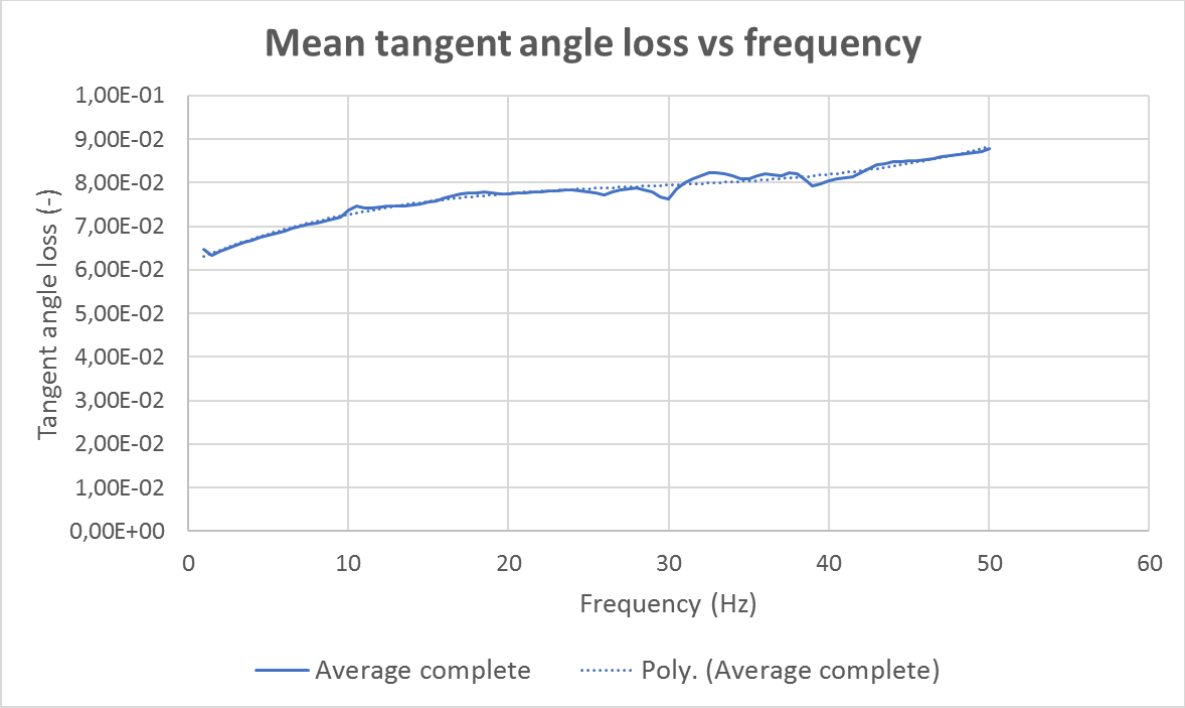

Figure 105: Mean tangent angle loss value with its polynomial regression

The tangent angle loss obtained from polynomial regression can thus be formulated as follows:

$$\eta(f) = 6.0 \times 10^{-7} f^3 - 5.0 \times 10^{-5} f^2 + 1.5 \times 10^{-3} f + 6.17 \times 10^{-2} \quad (171)$$

After, the two equation creations to model the DMA results parameters variation in function of the frequency, the creation of a pertinent analytical model is necessary. To be able to have a reliable comparison this analytical model should provide an expression of the DTS in function of the frequency according to the DMA results parameters.

1. Analytical models

At first, to develop an analytical model able to simulate the viscoelastic behaviour of the elastomer, several potential approach are available in the literature, as previously discussed in section I.C.2. In this section, the approach will be limited to the model previously discussed, the viscoelastic rheological models. At this point, the two most straightforward possible models are the Maxwell or Kelvin-Voigt models. While the Maxwell model is more suited to simulate soft solid, the Kelvin-Voigt model is more adapted to rubberlike material as previously discussed. Although, the Kelvin-Voigt does not model the viscoelastic material relaxation comparatively to the Zener model, for a dynamic response analysis, the relaxation cannot be consider due to the nature of the excitation (dynamic). In consequence, it is sufficient to use the Kelvin-Voigt model for this case.

Another feature that led to the choice of the Kelvin-Voigt model for the rubber part behaviour simulation is that this model is consistent with a model based on structural damping. Indeed, a model based on structural damping considers that the complex stiffness of the rubber can be decomposed in summation of a real part and imaginary part as granted in section I.D.2.a (equation 107 and 110). Hence, if "viscous damping" and "structural damping" models are supposed to be equivalent, then the elementary model components (spring, dashpot and imaginary stiffness) are supposed to work in parallel.

Figure 106 displays both models.

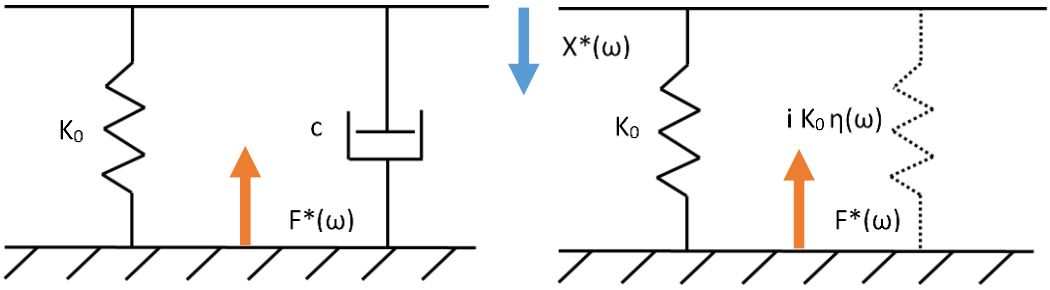

Figure 106: Analytical model using viscous damping (left) and structural damping (right)

By calculating the ratio between the complex reaction force ($F^*(\omega)$) and the complex displacement ($X^*(\omega)$), it is possible to obtain the DTS of the model as previously discussed in section I.B.3.b. In the analytical model, the complex stiffness is decomposed in a real part (k_0) and an imaginary part ($k_0\eta(\omega)$)

a) Model stiffness calculation

Before focusing on the damping feature of the models, it is necessary to set a relation between the Young modulus of the rubber obtained from DMA tests and the stiffness of each model. A suitable approach to determine the relation between the stiffness and Young modulus of a material is the dimensional analysis. In fact, when studying a one degree of freedom (1DOF) system, the dimension of a stiffness is a ratio between a force and a length ($N.m^{-1}$) and the Young modulus, expressed in Pa, is similar to ratio between a force and a surface ($N.m^{-2}$). Therefore, if the stiffness is directly proportional to the Young modulus, it can be expressed as follows:

$$k_0 = C_1 E \qquad 172$$

where C_1 is a constant expressed in m^{-1}.

This constant can designate several physical quantities. In this thesis, one of this physical quantity could refer to the so-called form factor (F_c) as it was previously designated in section I.D.2.b. In fact, if a hypothetical

solid is considered, this constant is a ratio between a surface, generally the excited one, and the length of the solid in the stress direction.

Hence, it is possible to relate the stiffness and the Young modulus as follows:

$$k_0 = \frac{S}{L} \times E \qquad 173$$

where S designates the excited surface and L, the mentioned length.

Among several possibilities to acquire this ratio, the most reliable approach is to use the curve extrapolated from the experimental results and the Young modulus polynomial regression to set it. The "static" values (values at 0 Hz) of those two models give acceptable reliance to set the model, the stiffness is thus equal to 9.4 10^6 N.m^{-1} and the Young modulus equal to 6.8 10^6 Pa. The "static" stiffness is then obtained from the ratio of these two values, that is:

$$\frac{S}{L} = \frac{9.41 \times 10^6}{6.83 \times 10^6} \qquad 174$$

Which leads to:

$$\frac{S}{L} = 1.38 \qquad 175$$

Once the "static" stiffness is set, it is possible to focus on the impact of the dampings on the DTS. However, if the Young modulus varies with the frequency, which is actually the case according to the DMA results, the stiffness k_0 varies also. Therefore, the models should integrate this variable stiffness for the DTS determination.

b) DTS analytical model based on structural damping

At first, the analytical model based on structural damping is examined. Considering a structural damping ($\eta(f)$) and consequently a complex stiffness, it is possible to express the reaction force $F^*(f)$ with respect to the complex displacement as follows:

$$F^*(f) = \left(k_0(f) + i \times k_0(f) \times \eta(f)\right) \times X^*(f) \qquad 176$$

Thereby, the expression of the DTS writes:

$$DTS\,(f) = \frac{F^*(f)}{X^*(f)} = \left(k_0(f) + i \times k_0(f) \times \eta(f)\right) \qquad 177$$

And the magnitude may be expressed as:

$$|DTS|\,(f) = k_0\sqrt{(1 + (\eta(f))^2)} \qquad 178$$

c) DTS analytical model based on viscous damping

Furthermore, considering a viscous damping, the expression of the reaction force is presented as following where the force and the displacement are still complex numbers:

$$F^*(f) = (k_0(f) + i \times c(f) \times 2\pi f) \times X^*(f) \quad 179$$

Thereby, the expression of the DTS is:

$$DTS\,(f) = \frac{F^*(f)}{X^*(f)} = (k_0(f) + i \times c(f) \times 2\pi f) \quad 180$$

And the magnitude may be expressed as:

$$|DTS|\,(f) = \sqrt{(k_0(f))^2 + (c(f))^2(2\pi f)^2} \quad 181$$

As it was presented in section I.B.3.a, the viscous damping and the structural damping are related by the following formula:

$$c(f) = \eta(f) \times m \times \frac{{\omega_0}^2}{\omega} \quad 182$$

However, the resonance circular frequency ω_0 is unknown for those systems as for the mass that is not present here. Therefore, it is impossible to regard those models as representations of oscillating system. A first consideration is possible concerning the mass. A fictive mass can be included in those models in order to calculate the viscous damping. In fact, this mass is present in the experiment and the numerical model.

Then it is possible to express the resonance circular frequency ω_0 as a function of the stiffness and the system related mass:

$$\omega_0 = \sqrt{\frac{k_0(f)}{m}} \quad 183$$

Finally, the viscous damping can be calculated with the following expression, using the stiffness $k_0(f)$ and the mass m:

$$c\,(f) = \eta(f) \times \sqrt{k_0(f) \times m} \quad 184$$

At this stage, it is finally possible to obtain an analytical expression of the DTS based on viscous damping or structural damping that involve parameters which vary with the frequency. Moreover, considering the equivalence between “structural” and “viscous” damping, the two resulting DTS should be the same.

2. Resulting DTS and comparison with DTS obtained from other methods

In this last section, the DTS obtained from the analytical model are confronted to the experimental one and to the DTS obtained numerically. At first, the unadjusted analytical model will be used for this confrontation. The analytical model are considered unadjusted when the coefficient of the parameter expression (Young modulus and tangent angle loss) are not changed. If the curve resulting from the analytical models do not correlate with the experimental curve, an attempt to fit the experimental model will be presented and its pertinence and coherence will be discussed.

a) Unadjusted analytical modes

The confrontation of the resulting curves is realized within the frequency range 1 - 50 Hz and is only discussed in terms of DTS magnitude. Figure 107 compares the DTS obtained from the two analytical models, the DTS obtained from the numerical simulation based on an averaged Young modulus and a viscous damping of 4000 N.s.m^{-1} and the experimental reference curve.

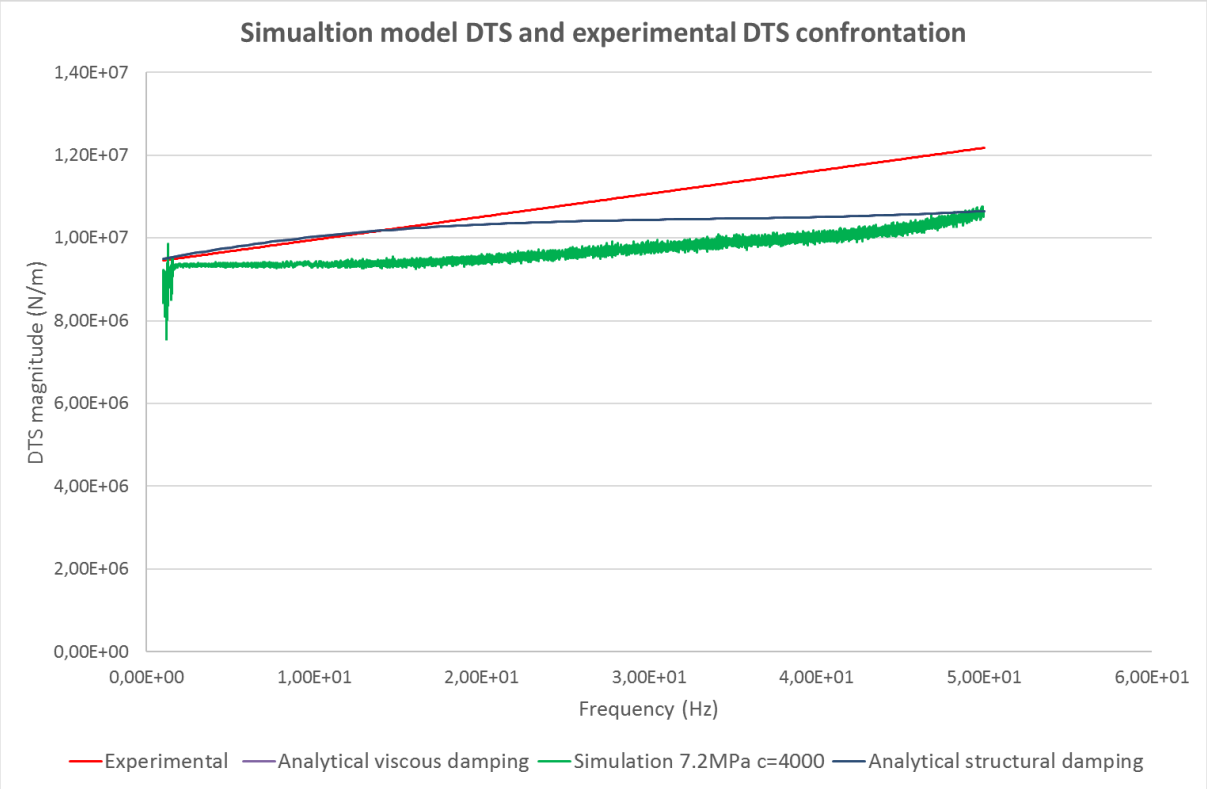

Figure 107: Simulation DTS and experimental DTS confrontation

At first, it appears that the superimposed analytical curves fit the experimental curve until 16 Hz. At this point, the curves starts to diverge with no more correlation. Moreover, it can be noted that the asymptotic slope of the analytical curves are completely different from the experimental and numerical one. Finally, the two analytical curves are also quite different from the numerical curve: they fit better the experimental curve than the numerical one. This is comprehensible due to the implementation of the variable parameters resulting from the DMA.

This results are not satisfying and in consequence, several attempts were realized to fit the analytical curves to the experimental one.

b) Adjusted analytical models.

This adjustment consists in changing one coefficient involved in the expression which gives the evolution of damping with the frequency (Equation 132). This can be justified by the uncertainty on the measurement of the damping of the RME. In fact, as it was previously discussed in the experimental part and DMA part, the tangent angle loss is quite small, and, for the one acquired during the experimental campaign, is also within the measurement uncertainty of the accelerometers that emerge when the system operates in low frequency. Several modifications on the coefficient were studied and the most pertinent will be exposed.

At first, if the modifications focus on the damping, the analytical expression should be examined deeper. The third order polynomial regression of the tangent angle loss was most balanced in terms of accuracy and complexity, but a linear regression, even though a regression of lesser quality, was still pertinent. Thus, the modification were concentrated on the coefficient related to the frequency at power 1, in the analytical expression of the tangent angle loss.

Figure 108 compares the new DTS obtained from the two modified analytical models, the DTS obtained from numerical simulation and the experimental curve.

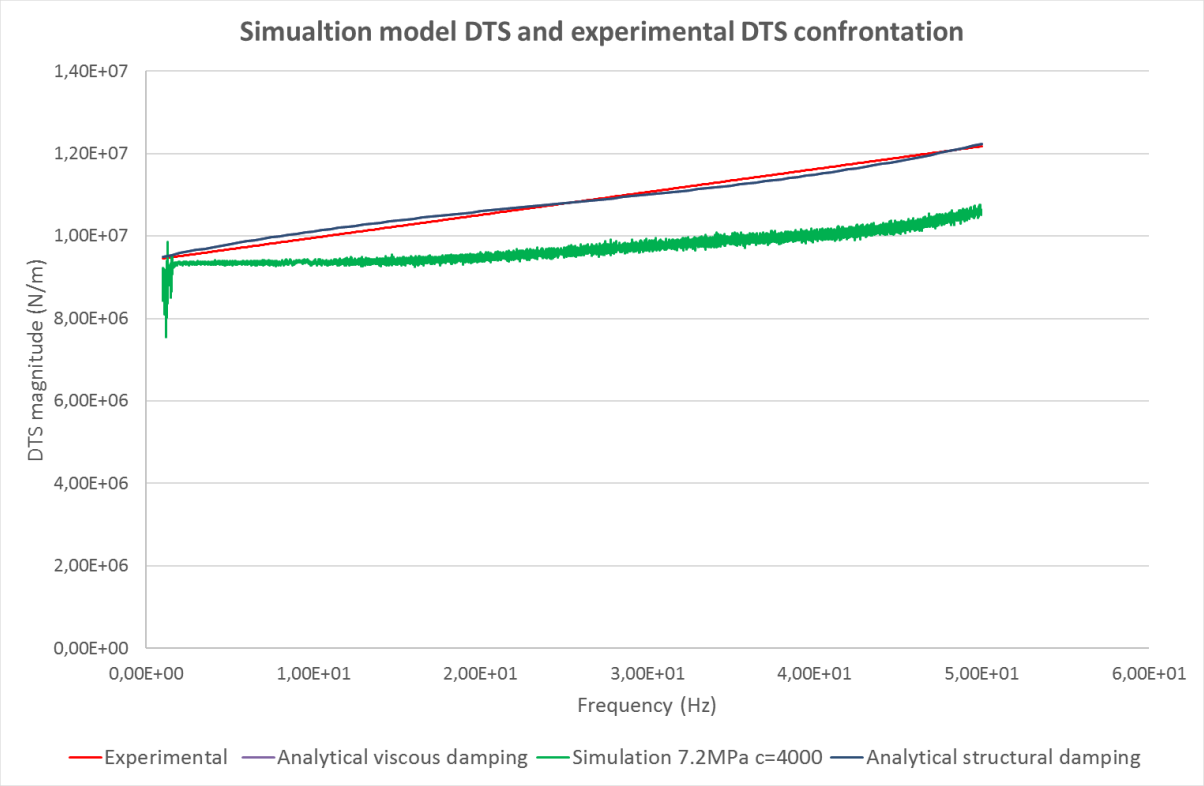

Figure 108: Simulation DTS and experimental DTS confrontation with adjusted parameters

A good fitting can be obtained by multiplying by 6 the coefficient related to the frequency at the power 1, the other coefficients remaining unchanged. It appears that, after this adjustment, the analytical curves fit the experimental curve appropriately. However, it can be noted that the asymptotic slope of the curve diverges slightly. Thus, it reduces the relevance of the modification. Furthermore, this modification has not a substantial physical meaning and is not supported by any consistent reason at the exception of the uncertainty about the viscous behaviour of the rubber.

In conclusion, it is difficult to judge the quality of the analytical model due to the partial correlation with the experimental curve and, therefore, it is difficult to validate the procedure. Several potential phenomena that are not considered in the analytical model, such as the gliding of the rubber on the steel parts or the influence of the Mullins effect, could create this difference.

Conclusion

The main objective of the presented thesis was to define and validate a procedure that enabled the characterization in frequency of a specific resilient mounting element (RME), the T200, via the determination of its dynamic transfer stiffness (DTS). The ambition of the thesis was to be able to avoid totally or partially the most spread method, the experimental characterization, which requires important experimental means and instrumentations, and could last several days or weeks. With the increase of the computational power through the last years, the interest arose for a possible determination using numerical simulations. Due to the known non-linear behaviour of the rubber, damping part of the T200, it was required to use non-linear simulation to be able to model the rubber behaviour.

According to the single point approach, presented in the thesis, the DTS determination of the resilient mount is sufficient to predict the structure born noise induced by the engines on board ship, simplifying the problem. Therefore, with the determination of the DTS, it is possible to estimate the discomfort of passengers on board and, hence, it is possible to conduct specific actions to reduce this discomfort. In fact, it was established in the thesis that most of the natural frequencies of the human body are between 2 and 60 Hz. Therefore, it was crucial to conduct the investigations and studies in the low frequency range. The planned frequency range of study was arbitrary set from 1 to 50 Hz.

Although the numerical characterization have many advantageous aspects as flexibility and short characterization time, there was not a lot of experience with this new method, at the exception of few ones. The use of non-linear simulations is an important feature to consider for the frequency characterization of a structure including a rubberlike material. A third method using analytical models, offered a third way for the determination of the DTS. The analytical simulations could be used when the numerical simulations are not capable to represent accurately the reality.

Concerning the resilient mounting element DTS, an important feature was noticed. Due to the weight of the engine, a compression load on the top of the RME was considered. It led to a resulting vertical deflection. Then, the RME reaches a static equilibrium related to an equilibrium point also called working point. Indeed, if the RME is subjected to vibrations induced by the engines, it oscillates around this working point. Even if the behaviour of the RME is globally non-linear (no proportionality between the load and the resulting deflection), it is possible to have a local linear behaviour around the working point leading to a local linearization of the system.

To enable the determination of this DTS, at the working point, a procedure was developed inspired by previous studies. This procedure was designed and tested according to two main axis:

- Experimental determination of the RME dynamic transfer stiffness
- Determination the DTS via simulations

As it previously mentioned, the main objective was the **creation** and the **validation** of the procedure. In order to validate the procedure it was necessary to acquire the accurate DTS at the working point. Therefore, a classical experimental characterization was planned to obtain the accurate DTS. Indeed the experimental approach represented the most reliable method. This experimental DTS served as reference in order to validate the numerical DTS and, by extension, to validate the procedure.

The numerical DTS determination required several data to be preformed. Indeed, several input parameters were needed, especially the parameters of the rubber constitutive law, to create the models. To be able to create an accurate model of the T200, the effect of the pre-compression on the rubber needed to be considered. Indeed, due to the rubber non-linear behaviour, the compression induced a modification of its intrinsic characteristics, especially its rigidity, which changes in function of the strain inside the rubber. Therefore, it was required to obtain the rubber intrinsic characteristic at the right strain state.

At the beginning of the thesis, the first objective was the creation of the T200 numerical models. The numerical models were created with data provided by Moro L. [41]. These data were obtained using reverse engineering. Indeed, the simulations that were previously performed modelled the T200 compression load, leading to the acquisition of the parameter values for the rubber constitutive law, knowing the corresponding deflection of the compression load. Therefore, the starting point of the procedure was the acquisition of the data provided by the T200 manufacturer (working load and corresponding vertical deflection). These numerical simulations were non-linear quasi-static simulations to be able to integrate the non-linearity of the rubber behaviour. The principal result obtained with the quasi-static simulations was the 3D rubber strain field in the rubber part. In fact, to determine the rubber intrinsic parameters in function of the frequency at the right strain state, a dynamic mechanical analysis (DMA) was necessary. It was required to evaluate the rubber intrinsic material parameter in function of the frequency at the right strain state, before initiating the numerical DTS determination.

In addition, two material laws were used to model the rubber behaviour in the quasi-static simulations. This feature was investigated to determine the possible adoption of the Hook linear law to model the rubber behaviour at the working point. The results obtained from the two models with different material laws were compared, and no concerning the results were significant. Then the linear law was chosen to reduce the complexity of the numerical model, used for the DTS determination simulation.

Furthermore, normal mode analyses of the RME numerical models were performed providing a natural frequency of 37 Hz, with its related vertical mode. It could had had an impact on the quality of the experimental measurements. However, due to the control in displacement during the experimental campaign, the potential vertical resonance mode was subdued.

Simultaneously of the first numerical simulations, it was necessary to conceived and build a test rig that could be used for low frequency experimental characterization. The conception of the test rig followed the specifications of the ISO standard 10846-2. One issue emerged from the test rig dimensioning. One of the resonance frequency (133 Hz) whose related resonance mode, was less than three time 50 Hz, highest value of the planned frequency range. Although it could had potentially disturb the measurements, no disturbances that could had been explained by this issue, appeared during the experiments.

After the test rig conception, a classical experimental resilient mount DTS determination was performed. Concerning the results, the quality was not really satisfying especially concerning the phase angle, even if the characterization was respecting the specifications of the standards above 4 Hz. Another characterization focusing on the DTS determination between 1 and 4 Hz is advised to complete the previous RME characterization in frequency.

During the dynamic mechanical analysis, issues appeared concerning the samples shapes. The design and cutting was not as simple as it previously appeared. Surprisingly, these issues did not disturb the quality of the results, as the dispersion analysis exposed. After the DMA testing, the rubber characteristics (Young modulus, tangent angle loss) depending on the amplitude and exciting frequency were expressed.

The modelling of the damping was difficult to achieve. The use of structural damping in LS-Dyna was not effective. Therefore, two viscous dampers were implemented in the model, whose values were calculated from the resulting tangent angle loss, acquired during the DMA, and the calculated first natural frequency (37Hz) of the RME, whose vertical normal mode.

For the determination of the RME dynamic stiffness, non-linear simulations were perform using a direct integration method in the time domain to reproduce exactly the same configuration as in the experimental campaign. Although the LS-DYNA software gives opportunities to perform temporal non-linear dynamic simulation, its utilization is quite limited due to the impossibility to have varying parameters in the material constitutive law. Thus, only one value of the Young modulus and one value of viscous damping were used for each numerical simulations.

Concerning the results obtained via numerical simulations, it can be noticed that the results are not satisfying. Focusing on the magnitude, the trends of the numerical DTS curves are quite different from the experimental DTS magnitude. Furthermore, regarding the influence of the Young modulus on the DTS magnitude, it just affects the constant part of the DTS. It does not affect the trend of the curve. Moreover, regarding the damping influence on the DTS magnitude, it just affects the slope of the DTS. It is also not possible to compare the resulting tangent angle loss, due to the quality of experimental results. In conclusion, it is difficult to estimate the relevancy of the numerical model due to the invariable parameters in the material laws. Therefore, the LS-Dyna numerical model is not sufficiently relevant to be considered as a reliable tool to estimate the resilient mounting element DTS and then, cannot be considered as a good predictive tool.

After the comparison between the numerical results and the experimental results, it was decided to create an analytical predictive model. Unlike the numerical model, the possibility to have variable material parameter in the analytical model exists.

Concerning the results obtained via analytical simulations with the unadjusted model, it can be notice that the integration of variable parameters in the model leads to better results. Indeed, the correlation between the curves is good until 15 Hz. However, after 15 Hz, the trends of the analytical curves are different from the experimental. Considering that the analytical model is one of the simplest rheological model, the results are surprisingly good due to the amount of potential issues.

The adjusted analytical model, as for it, presents interesting results. Indeed the change of one parameter coefficient in the model led to a good correlation between the analytical curves and the experimental one. However, this damping arbitrary change, with no pertinent justification engender speculative questioning. Therefore, the main questioning concerns the modelling of the damping. It could be an interesting subject of another work.

In conclusion, the analytical model provides interesting perspectives in terms of validation or further development. Due to the reduced possibilities concerning the numerical model. It is difficult to imagine deeper investigations in this direction.

However, several potential investigation tracks are possible. The first one concerns the development of the procedure for the six other directions; in order to determinate the DTS matrix. Concerning the numerical model, only one hypothetical possibility appears. The creation of a sub-routine in the LS-Dyna software in order to update the material law parameters during the simulation is possible but it could require the authorization of the software editor.

Another feature that could be developed, is the possibility to study the influence of the temperature on the DTS and integrate this influence on the material parameters. As, it was discussed in the thesis, the temperature is an important feature to consider when viscoelastic material are involved, which is the case here.

The last feature that could be investigated concerns the Mullins effect. Indeed, even if the Mullins effect was not considered in this thesis, for valid reasons, it could be interesting to investigate on this aspect.

References

[1] Turan, O. 2006. *A rational approach for reduction of motion sickness and improvement of passenger comfort and safety in sea transportation*, EU Project No. G3RD-CT-2002-00809, COMPASS Final Publishable Report.

[2] Blanchet A., 2000. *Comfort class and passenger ships*, Inter.noise 2000, The 29th International Congress and Exhibition on Noise Control Engineering.

[3] American bureau of shipping (ABS), 2015. *Guide for passenger comfort on ships.*

[4] Det Norske Veritas (DNV), 2011. *Rules for classification of ship: Comfort class*, part 5 chap. 12.

[5] Biot, M. and De Lorenzo, F. 2007. *Open Issues Regarding Noise and Vibrations on Board Cruise Ships: a Suggested Approach for Measuring Comfort*. Proceeding of the Autumn Conference 2007 − Advanced in Noise and Vibration Engineering, Institute of Acoustics, Oxford, UK.

[6] Griffin, M. J., 1990, *Handbook of Human Vibration*, Academic Press, ISBN 0-12-303040-4, pages 53-70.

[7] Mansfield, N. J., 2005, *Human response to vibration*, CRC Press, SBN 0-203-48722-2, pages 14-59.

[8] ISO 2631-5:2004. *Mechanical vibration and shock — Evaluation of human exposure to whole-body vibration*. International Organization for Standardization

[9] Borellia D., Gaggero T., Rizzuto E. and Schenone C., 2015. *Analysis of noise on board a ship during navigation and manoeuvres*, Ocean Engineering Volume 105, pages 256-269.

[10] Badino A., Borelli D., Gaggero T., Rizzuto E. and Schenone C., 2016. *Airborne noise emissions from ships: Experimental characterization of the source and propagation over land*, Applied Acoustics volume 104, pages 158-171.

[11] De Lorenzo F., Biot M. and Blanchet, A. 2005. *Ship noise and vibrations: some notes on the evolution of the standards*. Proceeding of the International Conference ICMRT '05, Neaples, Italy.

[12] Moro, L., Biot, M., Brocco, E., De Lorenzo F. and Mendoza Vassallo, P.N. 2013. *Hull Vibration Analysis of River Boats*. First International Conference IDS2013 – Amazonia, Iquitos, Peru.

[13] Clausen N.B. 2009. *Marine Diesel Engines: How Efficient can a Two-Stroke Engine be?* – Review at ship-efficiency.org.

[14] Brocco E., Biot M. and Micheli D., 2017. *Study of new solution to reduce vibration transmission on board ships.* Doctoral thesis, University of Trieste, Architecture and Engineering department, Trieste, Italie.

[15] Mendoza Vassallo P. N., Biot M. And Micheli D., 2017. *Experimental study and numerical simulation of the behavior of viscoelastic material to reduce the vibration on board ship.* Doctoral thesis, University of Trieste, Architecture and Engineering department, Trieste, Italie.

[16] Ran Lin T., Pan J., O'Shea P.J. and Mechefske C.K. 2009. *A Study of Vibration and Vibration Control of Ship Structures*. Marine Structures, 22, 730-743.

[17] Biot M. and Moro L., 2012. *Experimental study of a resilient mounting for marine diesel engines*. Proceedings of the IMDC 2012 Conference, Glasgow, UK.

[18] Biot M., Mendoza Vassallo P., N. and Moro L. 2014. *Prediction of the structure-borne noise due to marine diesel engines on board cruise ships.* Proceedings of the 21st Internation Congress on Sound and Vibration (ICSV 21), 2014, Beijing, China.

[19] Mondot J.M. & Petersson B., 1987. *Characterization of structure-borne sound sources: The source descriptor and the coupling function*. Journal of Sound and Vibration, 114(1).

[20] Fulford R.A.; Gibbs B.M. 1997. *Structure-Borne Sound Power and Source Characterization in Multi-Point-Connected Systems, Part 1: Case Studies for Assumed force Distributions*. Journal of Sound and Vibration, 204(4).

[21] J. W. Verheij. 1982. *Multi-path sound transfer from resiliently mounted shipboard machinery*. Delft: Technisch Physische Dienst TNO-TH, PhD Thesis.

[22] Petersson B. & Plunt J. 1982. *On Effective mobilities in the prediction of structure-borne sound transmission between a source structure and a receiving structure, part 1: Theoretical background and basic studies*. Journal of Sound and Vibration, 82.

[23] Hynnä P. 2002. *Vibrational Power Method in Control of Sound and Vibration. Research Report No. BVAL37-021229*, Technical Research Centre of Finland, 2002, Espoo, Finland.

[24] Nilsson A., Kari L., Feng L. and Carlsson U. 1998. *Resilient mounting of engines*. Proceedings of the 16th international Congress on Acoustics, vol. 4: 2373-2374. Seattle, U.S.A.

[25] Cremer L., Heckl M., and Petersson B.A.T. 2005. *Structure-borne sound, structural vibrations and sound radiation*, Berlin: Springer.

[26] Moorhouse A. T. & Gibbs B. M. 1993. *Prediction of structure-borne noise emission of machines: development of a methodology*. Journal of Sound and Vibration, vol. 167 (no. 2): pp 223-237.

[27] Besio G., Loredan V. and Contento O. 1997. *Improved Noise Control on Board Ships. Optimization of Resilient Mountings and Bed Structures*. Proceedings of the International Conference on Ship and Marine Research NAV'97, 1997, Sorrento, Italy.

[28] Thompson D.J., Van Vliet W.J. and Verheij W., 1998. *Developments of the Indirect Method for Measuring the High Frequency Dynamic Stiffness of Resilient Elements.* Journal of Sound and Vibration, 213(1), 169-188.

[29] Moro L. & Biot M. 2013c. *Laboratory tests pave the way for the knowledge of dynamic response of resilient mount-ings on board ships*. Proceedings of the PRADS2013 Conference, 2013, Changwon City, Korea.

[30] Moro L.; Brocco, E.; Mendoza Vassallo, P.N.; Biot, M.and Le Sourne, H. 2015. *Numerical simulation of the dynamic behaviour of resilient mounts for marine diesel engines*. Analysis and Design of Marine Structures - Proceedings of the 5th International Conference on Marine Structures, Marstruct 2015, Pages 149-158.

[31] Precision mechanics use non-linear isolators for low frequency application. Carrella A., Brennan M., Waters T.P., 2007. *Optimization of a Quasi-Zero-Stiffness Isolator,* Journal of Mechanical Science and Technology 21 pages 946-949.

[32] Ahn H.-J. 2008. *Performance limit of a passive vertical isolator using a negative stiffness mechanism*, Journal of Mechanical Science and Technology 22(12) pages 2357-2364.

[33] Houston, J., Gattis C. 2003. *Passive isolators for use on the international space station*, AIAA Paper 2004-0787.

[34] Shibata T., Sakai S. 2016. *Passive Micro Vibration Isolator Utilizing Flux Pinning Effect for Satellites,* J. Phys.: Conf. Ser. 744 012009

[35] Maritnez J. M., 2005., *Modélisation et charactérisation du comportement hyper-visco-elastique d'un polymères sous sollicitations multi-harmoniques et à différentes températures*, Doctoral thesis, University of Aix-Marseille II, Solid mechanic department, Marseille, France.

[36] *Delattre A., 2014., Caractérisation et modélisation du comportement hyper-viscoélastique d'un élastomère chargé pour la simulation de pièces lamifiées élastomère-métal et étude en fatigue,* , Doctoral thesis University François Rabelais, Tours.

[37] Petiteau J. C. 2012*. Caractérisation expérimentale et modélisation du comportement des élastomères en dynamique rapide : application aux plots de suspension.* Doctoral thesis, Ecole central de Nantes, Architecture and Engineering department, Nantes, France.

[38] Stahl K., Meingaßner G. J., Pflaum H., Mair C., *2013, Isolation of Torsional Vibrations in Automotive Applications - Passive Switching Isolator PSI,* 2th International CTI Symposium dq Automotive Transmissions, HEV and EV Drives dq,

[39] Liu, X., Wagner J*.,* 2002, *Design of a vibration isolation actuator for automotive seating systems - Part I: Modelling and passive isolator performance,* International Journal of Vehicle Design , Volume 29 (4)

[40] ISO 10816-6 (1995). *Mechanical vibration -- Evaluation of machine vibration by measurements on non-rotating parts -- Part 6: Reciprocating machines with power ratings above 100 kW*. International Organization for Standardization

[41] Moro L., Biot M., Micheli D., 2015. *Structure borne noise due to marine diesel engines: experimental study and numerical simulation for the prediction of the dynamic behavior of resilient mounts*. Doctoral thesis, University of Trieste, Architecture and Engineering department, Trieste, Italie.

[42] ISO 10846-1 (2008a). *Acoustics and vibration − Laborato-ry measurement of vibro-acoustic transfer properties of resilient elements − Part 1: Principles and guidelines*" International Organization for Standardization.

[43] Dickens J.D. & Norwood C.J. 1997. *Design of a test facility for vibration isolator characterization*, Acoustics Australia, vol. 25 (no. 1): pp 23-28.

[44] Dickens J.D. & Norwood C.J. 2001. *Universal method to measure dynamic performance of vibration isolators under static load*, Journal of Sound and Vibration, vol. 244 (no.4): pp 685-696.

[45] Poole, R J. 2012*. The Deborah and Weissenberg numbers*. The British Society of Rheology, Rheology Bulletin. Volume 53 number 2. pp 32-39.

[46] 2018*. Viscosity*. Merriam-Webster dictionary

[47] Ferry, J.D. 1991. *Some reflections on the early development of polymer dynamics: Viscoelasticity, dielectric dispersion and self-diffusion.* Macromolecules. Volume 24 number 19. pp 5237–5245.

[48] ISO 6721-1 2011. *Determination of dynamic mechanical properties -- Part 1: General principles elements* International Organization for Standardization.

[49] Williams, M.L., Landel, R.F., Ferry, J.D. (1955). *The Temperature Dependence of Relaxation Mechanisms in Amorphous Polymers and Other Glass-forming Liquids*. Journal of American Chemical Society Volume 77 number 14. pp 3701–3707.

[50] Ogden R.W., 1984. *Non-Linear Elastic Deformations*. ISBN: 0-486-69648-0. Dover.

[51] Yeoh, O. H., 1993. *Some forms of the strain energy function for rubber*, Rubber Chemistry and technology, Volume 66, Issue 5, Pages 754-771.

[52] Mullins L. 1969. *Rubber Chemistry and Technology*. Volume 42 pp 339

[53] Dubigeon S. 1998. *Mecanique des milieux continus*. ISBN: 2-912985-00-5. Ecole centrale de Nantes

[54] ISO 7626-1-2-3-4-5 2011 *Mechanical vibration and shock -- Experimental determination of mechanical mobility.* International Organization for Standardization.

[55] Salgado J. & Meireles J., 2011*. Dynamic stiffness and loss factor measurement of engine rubber mount by impact test.* Fifth International Operational Modal Analysis Conference Guimarães - Portugal

[56] Oudet C. 1993. *Mecanique des milieux continus*. ISBN: 2-225-84271-X. Elsevier Masson. Pages 1-70

[57] Kari L., 1998*. Structure-borne sound properties of vibration isolators.* PhD Dissertation, KTH- Royal Institute of Technology, Stockholm

[58] C. A. J. Beijiers & De Boer A., 2003*. Numerical modelling of rubber vibration isolator.* Tenth International congress of sound and vibration, Pages 149-158.

[59] https://pixabay.com/en/driving-cruise-ship-night-port-ship-759796/

[60] https://www.publicdomainpictures.net/en/view-image.php?image=176921&picture=large-luxury-yacht

[61] https://www.pon-cat.com/power/sc/caterpillar-products/marine-power-systems/marine-power-systems/marine-generator-sets/vm-43-c